

Contrails

FOREWORD

This investigation was initiated by the Multienvironment Division, Biophysics Laboratory, 6570th Aerospace Medical Research Laboratories, Aerospace Medical Division, Wright-Patterson Air Force Base, Ohio. The research was conducted by Northrop Space Laboratories, Hawthorne, California, under Air Force Contract AF33(657)-8762, Project No. 6301, "Aerospace Systems Personnel Protection," Task No. 630101, "Physical Protection of Man Against Ionizing Radiation." Northrop Space Laboratories have assigned number NSL 63-168 to this document. The work was monitored technically by Mr. Loren Pittman of the Radiation Shielding Branch.

This report is submitted as the final report for the Contract AF33(657)-8762. Mr. R. E. Fortney of Northrop Space Laboratories was the program manager responsible for this study. The assistance of the following personnel is gratefully acknowledged: G. D. Duckworth, M. R. Morrison, J. L. Spadafora, and A. E. Tate.

Contrails

ABSTRACT

The purpose of this mathematical study, "Computer Analysis of Radiation Shielding" (CARS), was to develop mathematical methods to assess the biological hazards of space radiation and to program these methods for the IBM 7090 using FORTRAN language. In the accomplishment of the above tasks, a semianalytical approach was utilized to write machine programs for geocentric trajectories and a model astronaut inside a space vehicle. The trajectory program is used to solve the two body problem with perturbations to correct for the oblateness of the earth. The earth's magnetosphere is the space of principle interest for lunar missions, therefore lunar impact and return trajectories are considered to be two body geocentric orbits. An astronaut's head and torso are represented by two right elliptical cylinders. This model is placed inside a mathematically described space vehicle with known thicknesses in designated areas. An existent machine program was utilized to define the radiative environment in McIlwain (B,L) coordinates and supplemental computer programs were used to determine radiation doses resulting from electron and proton environments. Results from the CARS program are obtained with a small amount of machine time. For example, one tenth (.1) of an hour was required to determine the radiation dose due to two spectra (electrons and protons) at ten points in the model astronaut within the APOLLO Command Module (CM) for a given orbital mission.

PUBLICATION REVIEW

This technical documentary report is approved.

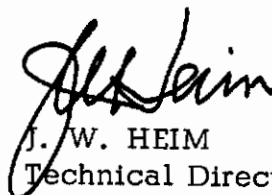

J. W. HEIM
Technical Director
Biophysics Laboratory

TABLE OF CONTENTS

<u>Section</u>		<u>Page No.</u>
1	INTRODUCTION	1
2	RADIATIVE ENVIRONMENT	2
	2.1 McIlwain Coordinates	2
	2.2 Van Allen Zones	10
	2.3 Solar Flares	17
	2.4 Galactic Cosmic Rays	25
	2.5 Solar Wind	28
3	MISSION TRAJECTORIES	31
	3.1 Geocentric Orbits	31
	3.2 Lunar Transfer Trajectories	36
	3.3 Lunar Return Trajectories	37
4	RADIATION-MATERIAL INTERACTIONS	38
	4.1 Electron Interactions	38
	4.2 Electron Shielding Calculations	45
	4.3 Proton Interactions	50
	4.4 Proton Shielding Calculations	54
5	SHIELDING CALCULATIONS	60
	5.1 Isotropic Flux and Beam Flux Relationships	60
	5.2 Dose Rate Determinations	62
6	VEHICLE GEOMETRY	70
	6.1 Mathematical Description of Surfaces	70
	6.2 Calculation of Slant Thickness	72
7	MODEL ASTRONAUT	78
	7.1 Description of Mathematical Model	78
	7.2 Biomedical Tolerances	80
	7.3 Calculation of Tissue Slant Thickness	80
8	RESULTS	83
9	RECOMMENDATIONS	84
	REFERENCES	85

LIST OF ILLUSTRATIONS

<u>Figure No.</u>	<u>Title</u>	<u>Page No.</u>
1	Invariant Shells	4
2	Mapping of Polar Coordinates R and λ on to B,L Plane	6
3	Contours of Constant Count Rate Transformed to R and λ Coordinates	7
4	Trapped Proton Spectrum (Freden and White)	11
5	Variation of Proton Spectrum with L (Naugle and Kniffen)	12
6	Composite Trapped Proton Spectrum	14
7	Artificial Belt Electron Spectra	15
8	Van Allen Zones-Idealized Cross Section	16
9	Outer Van Allen Zone Electron Spectrum	18
10	Integral Proton Energy Spectra (Bailey)	21
11	Integral Proton Energy Spectra (Winckler)	22
12	Time Variation of Solar Cosmic Ray Proton Spectra	23
13	Model Solar Flare - Differential Flux	24
14	Envelope Flare	26
15	Spectrum of Galactic Cosmic Rays	29
16	Interaction of Solar Wind with the Earth's Magnetic Field	30
17	Trajectory Options	32
18	Equatorial Coordinate System	33
19	Orbit Plane Coordinate System	35
20	Electron Stopping Power for Aluminum	40

LIST OF ILLUSTRATIONS (Con't)

<u>Figure No.</u>	<u>Title</u>	<u>Page No.</u>
21	Range of Electrons in Aluminum	41
22	Transmission Factors at Various Energies for Electrons Normally Incident on Aluminum	42
23	Thick-Target Bremsstrahlung Photon Spectra in Aluminum	43
24	Bremsstrahlung Cross Sections, Differential in Photon Energy but Integrated with Respect to Angular Distribution	46
25	Electron Energy as Related to Depth of Penetration in Aluminum	47
26	X-Ray Flux-to-Dose Conversion Factor	51
27	Range of Protons in Aluminum	52
28	Nucleon-Nucleon Cross Sections	55
29	Proton Nonelastic Cross Section for Aluminum	56
30	Flux - Geometry Relationships	61
31	Dose Rate versus Depth in Tissue Due to Van Allen Protons After Passing Through Various Thicknesses of Aluminum	66
32	Dose Rate versus Depth in Tissue Due to Artificial Belt Electrons Passing Through Various Thicknesses of Aluminum	67
33	Dose Rate versus Depth in Tissue Due to Solar Flare Protons After Passing Through Various Thicknesses of Aluminum	68
34	Surfaces Available for Describing Spacecraft Geometry	71
35	Wall Slant Thickness Relationship	73
36	Cross Section of APOLLO Command Module Showing Position and Orientation of Model Astronaut in Sample Problem	75

LIST OF ILLUSTRATIONS (Con't)

<u>Figure No.</u>	<u>Title</u>	<u>Page No.</u>
37	Typical Wall of the APOLLO Command Module	76
38	Model Astronaut Based on Dimensions of U.S. Air Force Flying Personnel	79

LIST OF TABLES

<u>Table No.</u>		<u>Page No.</u>
1	Gaussian Coefficients Finch and Leaton 1955.0 Epoch Data	8
2	Gaussian Coefficients Jensen and Cain 1960.0 Epoch Data	9
3	Electron Fluxes and Energies in the Outer Van Allen Zone	17
4	Solar Flare Data	20
5	Relative Abundances of Nuclei in Cosmic Rays	27
6	Solar Wind	30
7	Source Distribution of X-Ray Dose Due to Artificial Belt Electrons	48
8	Orthogonal Polynomial Coefficients for Van Allen Protons for Various Thicknesses of Aluminum	63
9	Orthogonal Polynomial Coefficients for Artificial Belt Electrons Penetrating Various Thicknesses of Aluminum	64
10	Orthogonal Polynomial Coefficients for Envelope Flare Protons Penetrating Various Thicknesses of Aluminum	65
11	NASA Biomedical Tolerances	80
12	Dose Results	83

SECTION 1

INTRODUCTION

The principal goal for this study has been the development of an analytical tool utilizing digital computing programs for the overall assessment of shielding against space radiation. The mathematical analysis has resulted in the generation of a number of computer routines which can be utilized with CHAINED main programs to perform parametric studies of space missions for various spacecraft, or the programs can be used separately for specific detailed studies. This report presents the general mathematical development of Computer Analysis of Radiation Shielding (CARS) with a technical discussion of the simplifying assumptions.

The approach taken in a computer analysis of this type must compromise between rigor in the mathematical treatment of the physical processes and geometries involved and the computer (machine) running time required. To achieve this compromise certain assumptions have been made, and the approach is semianalytical and at times even empirical. The intensities and spectra of the protons and electrons trapped in the earth's magnetic field are not known with accuracy and solar flare proton spectra and intensities are specified with even less accuracy. Thus, mathematical rigor with the extensive computing time required to obtain the possible accuracy for radiation penetration is considered irreconcilable with the present knowledge of the radiative environment. Therefore, a thoughtful balance has been sought between calculational complexity and the accuracy of the geophysical data.

To assess the radiation hazard a specific mission presents to crew members, the following steps are necessary:

- (1) the radiation fluxes (protons and electrons) must be integrated along the mission trajectory,
- (2) the interaction of the specific space vehicle with these time integrated fluxes must be evaluated, and
- (3) the interaction of the penetrating radiation with the astronaut must be evaluated as radiation dose.

The mathematical development of a method for accomplishing this is discussed in the following sections along with pertinent background information.

SECTION 2

RADIATIVE ENVIRONMENT

The particulate radiative environment in space consists of the geomagnetically trapped particles, solar flare particles, galactic cosmic rays, and particles from the solar wind. The type and duration of a mission will determine which part of the radiative environment must be considered when planning protection for man and equipment. The geomagnetically trapped particles are necessarily a near-earth phenomenon, while the other types of radiation are important outside of the earth's magnetosphere. These environmental components will be discussed in some detail in Sections 2.2, 2.3, 2.4 and 2.5.

A convenient coordinate system for describing the geomagnetically trapped radiation has been developed by C. E. McIlwain. This system and its application to the CARS program is discussed in Section 2.1.

2.1 McILWAIN COORDINATES

In order to determine the flux intensities encountered by a vehicle in a geocentric orbit, it must be possible to map the intensities of trapped radiation. Early attempts, using a dipole model for the earth's magnetic field gave unreliable results, due to the high spatial gradients in intensity that exist and the deviation of the earth's field from that of a dipole. C. E. McIlwain (ref 1) developed a coordinate system which takes into account the nondipole character of the earth's field and allows intensity measurements to be organized along lines of force.

The problem of describing the motion of particles in a magnetic field is greatly simplified if the time variation of the magnetic field is slow enough to allow adiabatic approximations. In reference 2, Northrop and Teller discuss the resulting adiabatic invariants of motion. Only two adiabatic invariants are important if the following type of magnetic field is considered:

- (a) at a given longitude and latitude, the magnetic field decreases with increasing radial distance,
- (b) a line of force contains only one relative minimum in magnetic field intensity, and
- (c) the magnetic field is essentially static and without electric field, so that particle momentum is constant.

The first adiabatic invariant can be written

$$\mu = P_L^2 / 2MB = \text{constant}, \quad (1)$$

Contrails

where μ is the magnetic dipole moment associated with the spiral motion of the particle of mass M , B is the magnetic field intensity at the position of the particle, and P_{\perp} is the component of the particle momentum perpendicular to the line of force. Also

$$\mu = P^2 \sin^2 \alpha / 2MB = \text{constant}, \quad (2)$$

where α is the pitch angle of the particle. (It can be seen that as α approaches 90° the momentum of the particle becomes more perpendicular to the line of force. Thus when $\alpha = 90^\circ$ the particle does not continue to move down the line of force, but mirrors and travels along the line of force in the opposite direction.) Since the particle momentum P is constant,

$$\frac{\sin^2 \alpha}{B} = \frac{2\mu M}{P^2} = \frac{1}{B_m} \quad (3)$$

where B_m is the magnetic field intensity at which a particle mirrors. The second adiabatic invariant, called the longitudinal or integral invariant is

$$J = \int_{B_m}^{B'_m} P_{\parallel} ds, \quad (4)$$

where the integration is performed along the line of force connecting the two mirror points of the particle. Since

$$P_{\parallel} = P \cos \alpha = P(1 - \sin^2 \alpha)^{\frac{1}{2}} \quad (5)$$

an alternative form of the integral invariant is

$$I \equiv \frac{J}{P} = \int_{B_m}^{B'_m} \left[1 - \frac{B}{B_m} \right]^{\frac{1}{2}} ds. \quad (6)$$

Defined in this way, I can be considered a scalar field that has a definite value at each point in space and does not require reference to the motion of trapped particles. However, the value of I obtained by integrating equation 6 between B_m and B'_m cannot be applied to all particles observed at these two points, but only to those mirroring at these points (ref 3).

Contrails

The points in space that have the same value of B and I form a ring in each hemisphere, and particles mirroring at this B and I will remain on the surface described by the lines of force that connect these rings, figure 1.

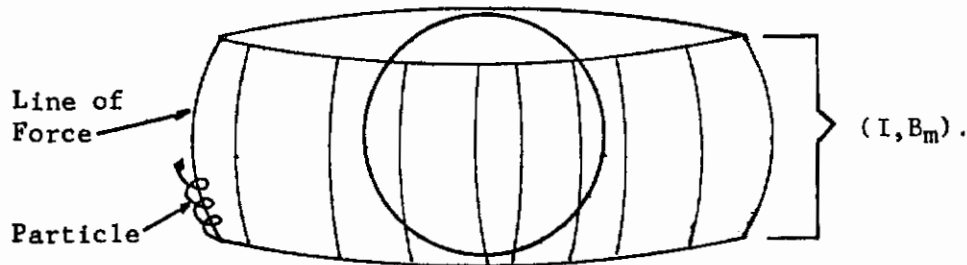


Figure 1 Invariant Shell

Because of azimuthal asymmetry in the geomagnetic field, two particles that initially mirror at different values of B along a particular line of force will not drift in longitude to the same line of force. However, the invariant shells for the two particles are separated by less than ± 1 percent in equatorial radius in the earth's field. Since all particles that drift through a particular line of force will remain on approximately the same invariant shell throughout their motion, it is desired to label each invariant shell uniquely. A characteristic radius, R_{0D} , which is the equatorial radius of the shell in a dipole field is utilized because of two facts: (1) The actual shell radius, R_0 , which is longitude dependent in the geomagnetic field is nearly equal to R_{0D} , and (2) the radial separation of invariant shells in the earth's magnetic field with the same characteristic radius, R_{0D} , is only ± 1 percent of the shell radius. A function $R_{0D} = F(I, B)$ is determined, where I and B are invariants of particle motion. The development of this function is shown in reference 1. The final result is

$$\frac{R_{0D}^3 B}{M} = F\left(\frac{I^3 B}{M}\right) . \quad (7)$$

The above equation is valid for dipole fields only. A magnetic shell parameter L, in units of earth radii, is now defined for a point in the geomagnetic field by

$$\frac{L^3 B}{M} = F\left(\frac{I^3 B}{M}\right) , \quad (8)$$

Contours

where I and B are calculated for the point with a representation of the earth's field, M is the dipole moment of the earth, and F is the function found in the dipole field. L is associated with a particle of longitudinal invariant I mirroring at B ; if a particle has the same mirror point B and invariant I in both the geomagnetic field and a dipole field, then the L value for the particle is identical with the R_{0D} of the same particle in a dipole field. A set of values for the function F are given in reference 1. The following method is used to accurately compute L :

$$\ln \left(\frac{L^3 B}{M} - 1 \right) = \sum_{n=0}^{n=6} a_n X^n, \quad (9)$$

where

$$X = \ln \frac{I^3 B}{M}$$

Sets of the coefficients, a_n , for different ranges of X are given in reference 1.

In order to obtain a coordinate system that resembles the actual physical geometry, B and L can be transformed to polar coordinates using the dipole relations,

$$B = \frac{M}{R^3} \left(4 - \frac{3R}{L} \right)^{\frac{1}{2}}, \quad R = L \cos^2 \lambda \quad (10)$$

where R is the radial distance of a point and λ is the geomagnetic latitude. Figure 2 shows R and λ plotted on the B, L plane using the above relations. Because of the asymmetries in the geomagnetic field, a transformation to polar coordinates will cause geographic coordinates to have an irregular dependence on longitude. Figure 3 shows contours of constant counting rate transformed to polar coordinates.

The representation of the geomagnetic field utilized employs a set of 48 spherical harmonic coefficients. These coefficients are derived from a spherical harmonic analysis of the geomagnetic field using observations of the horizontal and vertical components of the field at various points on the surface. The analysis yields the Gauss coefficients, g_m^n and h_m^n , which are utilized in the determination of the intensity of particles at a point. A complete development of the spherical harmonic analysis of the earth's magnetic field is presented in reference 4. Table 1 presents Finch and Leaton 1955.0 epoch data (ref 5) and table 2 presents Jensen and Cain 1960.0 epoch data (ref 6). Either of these or any other set of 48 coefficients may be used as magnetic field data. The fullest

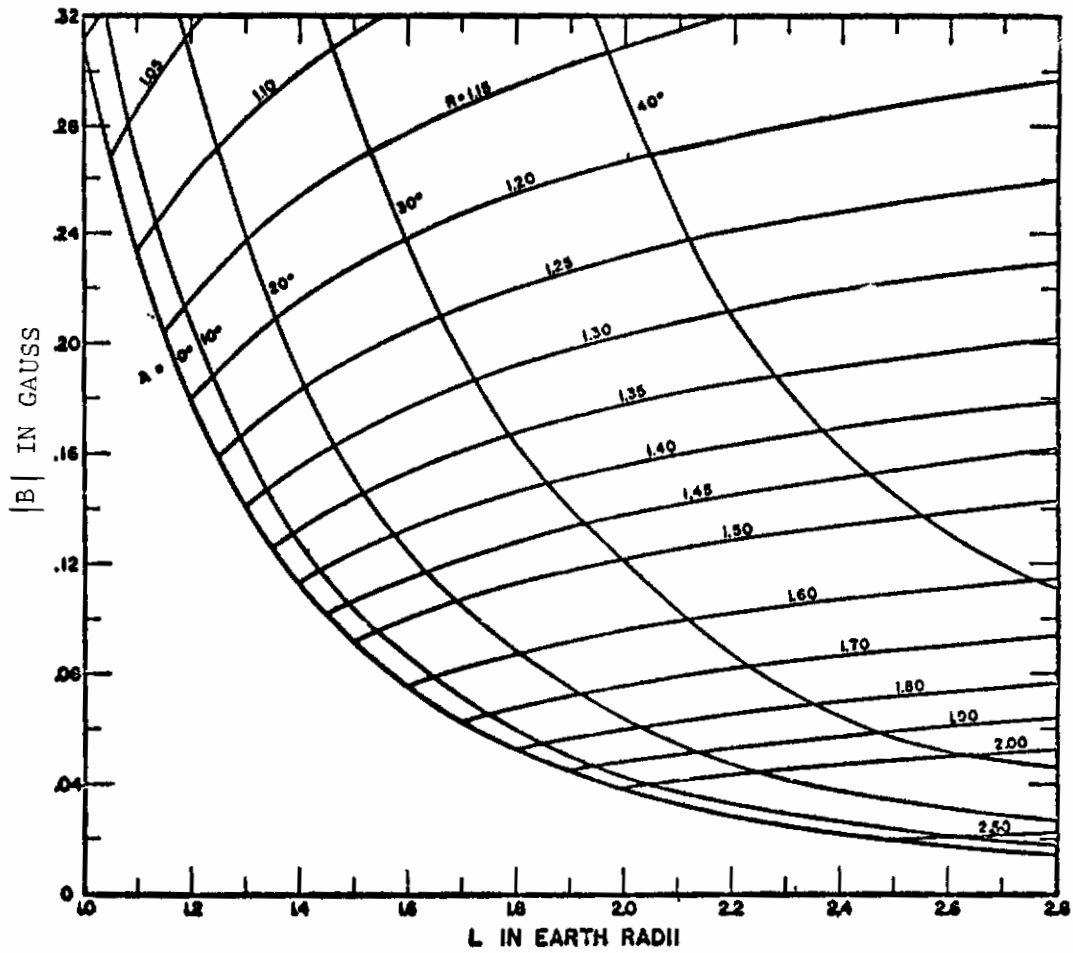


Figure 2. Mapping of Polar Coordinates R and λ on to B, L Plane

Contrails

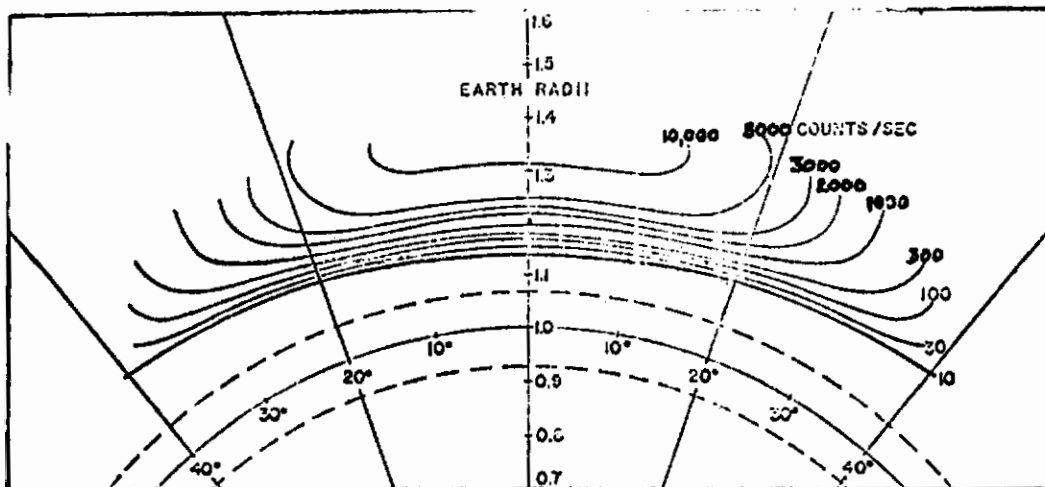


Figure 3. Contours of Constant Count Rate Transformed to R and λ Coordinates

TABLE 1

GAUSSIAN COEFFICIENTS

FINCH AND LEATON 1955.0 EPOCH DATA

m,n	g	h
1,0	-0.3055	
1,1	-0.0227	0.0590
2,0	-0.0152	
2,1	0.0303	-0.0190
2,2	0.0158	0.0024
3,0	0.0118	
3,1	-0.0191	-0.0045
3,2	0.0126	0.0029
3,3	0.0091	-0.0009
4,0	0.0095	
4,1	0.0080	0.0015
4,2	0.0058	-0.0031
4,3	-0.0038	-0.0004
4,4	0.0031	-0.0017
5,0	-0.0027	
5,1	0.0032	0.0002
5,2	0.0020	0.0010
5,3	-0.0004	-0.0005
5,4	-0.0015	-0.0014
5,5	-0.0007	0.0009
6,0	0.0010	
6,1	0.0005	-0.0002
6,2	0.0002	0.0011
6,3	-0.0024	0.0000
6,4	-0.0003	-0.0001
6,5	0.0000	-0.0003
6,6	-0.0011	-0.0001

TABLE 2

GAUSSIAN COEFFICIENTSJENSEN AND CAIN 1960.0 EPOCH DATA

m,n	g	h
1,0	0.304112	
1,1	0.021474	-0.05798.9
2,0	0.024035	
2,1	-0.051253	0.033124
2,2	-0.013381	-0.001579
3,0	-0.031518	
3,1	0.062130	-0.014870
3,2	-0.024898	-0.004075
3,3	-0.006496	0.000210
4,0	-0.041794	
4,1	-0.045289	-0.011825
4,2	-0.021795	0.010006
4,3	0.007008	0.000430
4,4	-0.002044	0.001385
5,0	0.016256	
5,1	-0.034407	-0.000796
5,2	-0.019447	-0.002000
5,3	-0.000608	0.004597
5,4	0.002775	0.002421
5,5	0.000697	-0.001218
6,0	-0.019523	
6,1	-0.004853	-0.005758
6,2	0.003212	-0.008735
6,3	0.021413	-0.003406
6,4	0.001051	-0.000118
6,5	0.000227	-0.001116
6,6	0.001115	-0.000325

advantage of a B,L coordinate system will be obtained if the Gauss coefficients are updated every 10 years or less. It would be possible to utilize larger sets of Gauss coefficients such as Jensen and Whitaker's set of 512 coefficients (ref 7); however, sufficient accuracy in the final flux of particles, is obtained with the 48 coefficient set.

2.2 VAN ALLEN ZONES

The Van Allen zones consist of electrons and protons trapped in the geomagnetic field. The inner and outer zones are usually depicted as two distinct torroidal belts. In addition, recent high altitude nuclear detonations (ref 8) have created an artificial belt of geomagnetically trapped electrons at relatively low altitudes. The naturally occurring zones are characterized by: (1) high energy protons which are found in the inner zone, and (2) high energy electrons, found in the outer zone. The zones are generally symmetric with the plane of the geomagnetic equator, although a magnetic anomaly in the South Atlantic region causes the belts to dip to lower altitudes in this area. Since the planes of the geomagnetic equator and the geographic equator vary by 11.4° , the radiation belts would appear to wobble if they were viewed from an orbiting equatorial satellite.

2.2.1 Inner Zone

The inner zone particles are trapped in a region of $L \approx 1.6$. Although both protons and electrons are present in the zone, the protons, with energies up to several hundred Mev, are more important from a shielding viewpoint. The inner zone is considered to be generally stable in time, with particle lifetimes in the order of years. Because of this, a low efficiency steady source mechanism is theorized. The theory proposed by Singer (ref 9) is that neutrons from cosmic ray collisions with atmospheric particles decay, giving protons and electrons that are trapped in the earth's field. This injection source, albedo neutrons, can explain the fluxes of higher energy protons; however, a variation in the intensity of lower energy protons has been noted (ref 10) and it has been suggested (ref 11) that solar protons that strike the polar atmosphere could give rise to albedo neutrons, which would result in lower energy trapped protons, whose intensity is a function of solar activity. However, McIlwain (ref 12) who observed a time variation in intensity could not correlate it with solar events.

Information on the spectrum of protons has been obtained from rocket flights into the bottom of the inner zone (refs 13, 14, 15, and 16). Freden and White obtained a spectrum, figure 4, and in the determination of particle intensities at points in B,L space, this spectrum was assumed valid throughout the entire volume of the inner zone. Naugle and Kniffen found a variation of spectrum with L. (See figure 5.) At low L values

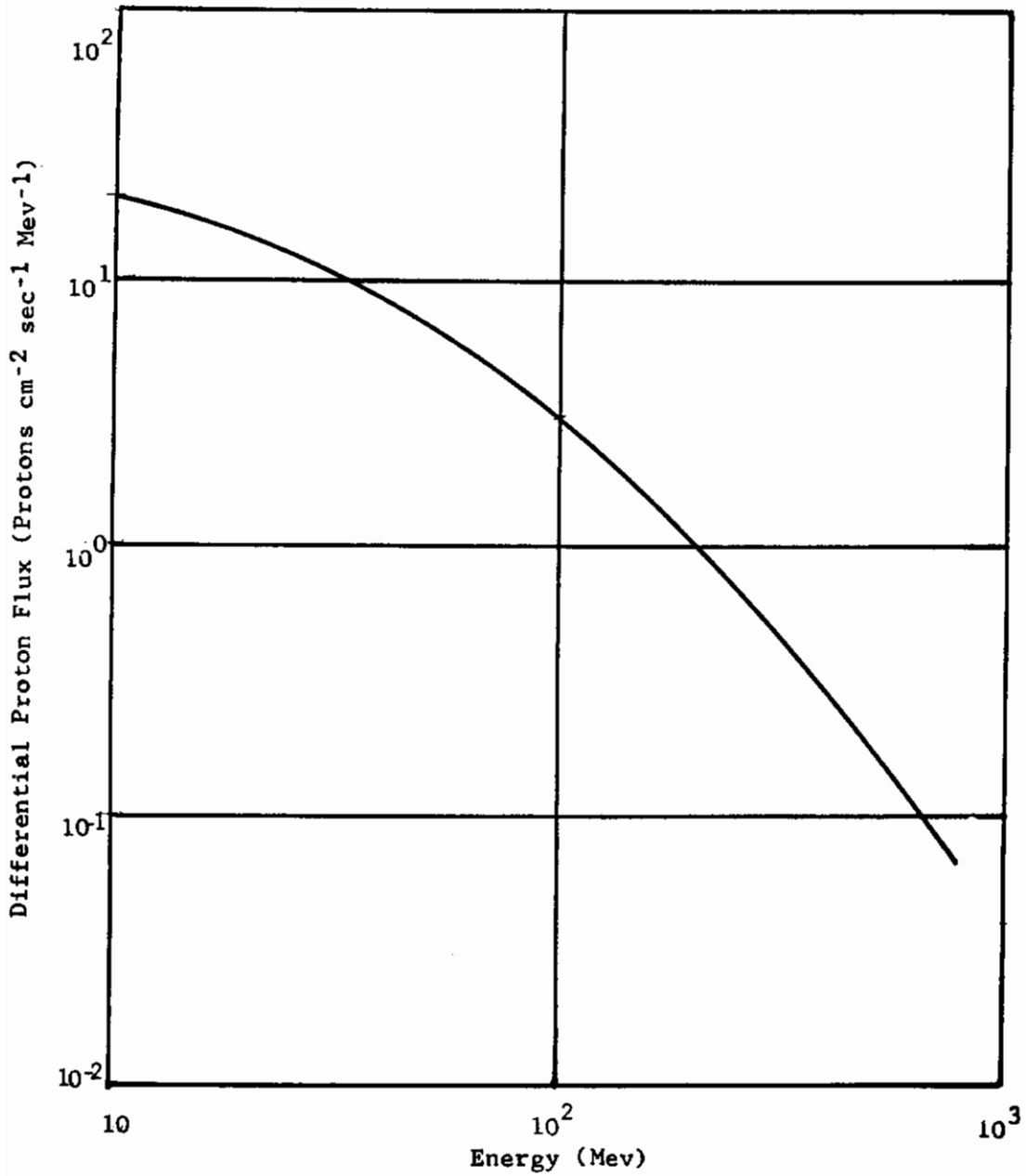


Figure 4. Trapped Proton Spectrum (Freden and White)

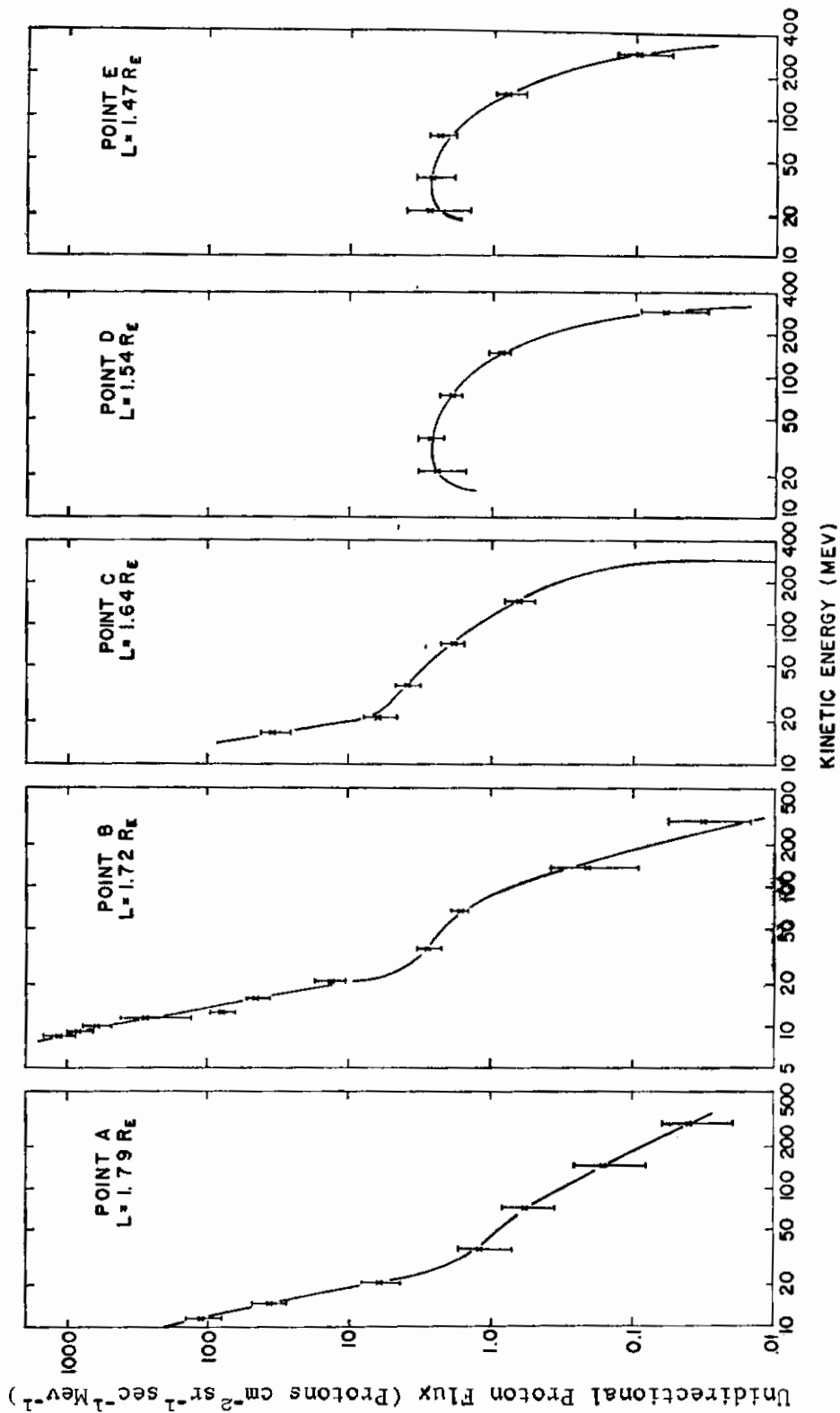


Figure 5. Variation of Proton Spectrum with L (Naugle and Kniffen)

the spectrum agrees with that of Freden and White; however at higher L values ($L > 1.55$) a large number of protons below 30 Mev were observed. Therefore, a composite spectrum was developed to be used in calculation of the proton penetration of materials. This spectrum, figure 6, is shown as a normalized unidirectional differential flux curve. This spectrum was obtained by describing the integral flux analytically by a fourth order logarithmic polynomial,

$$\ln \phi(E) = a_0 + a_1 \ln E + a_2 (\ln E)^2 + a_3 (\ln E)^3 + a_4 (\ln E)^4 \quad (11)$$

which is normalized by letting $\phi(40) = 1$. These values of $\phi(E)$ were then converted to unidirectional differential flux.

2.2.2 Artificial Electron Zone

Information on the electrons in the inner zone, which was scarce before mid-1962, has been complicated by the addition of the electrons from the fission fragments of Starfish. Since the natural component is not different from the artificially injected component of inner zone electrons, separation of the components is practically impossible.

The artificial belt was formed on July 9, 1962 by a high altitude nuclear detonation over the Central Pacific Ocean. The fission fragments from the detonation decayed, giving a large number of electrons that were trapped in earth's field. These electrons initially would have a fission spectrum of the form (ref 17)

$$Y_0(E) = 3.88 \exp. (-0.575E - 0.055E^2). \quad (12)$$

The electrons have decayed with time and McIlwain (ref 18) reports fluxes of 3×10^8 electrons $\text{cm}^{-2}\text{sec}^{-1}$ for $E > .5$ Mev and 10^7 electrons $\text{cm}^{-2}\text{sec}^{-1}$ for $E > 5$ Mev. The curves for the differential fission electron spectrum and McIlwain's data are shown in figure 7. The difference in spectra below 5 Mev is interpreted as the decay of electrons from July 9, 1962 to January 1, 1963 (the date of McIlwain's observations).

2.2.3 Outer Zone

The outer zone extends to higher latitudes than the inner zone and reaches its lowest altitudes at these high latitudes. In the latitude range $50^\circ - 65^\circ$, the outer zone exhibits what is known as its "horn" structure as it dips to relatively low altitudes. A qualitative picture of the outer zone surrounding the inner zone is shown in figure 8. The outer limit of this zone is extremely variable, ranging between $L \approx 7$ to $L \approx 20$ earth radii.

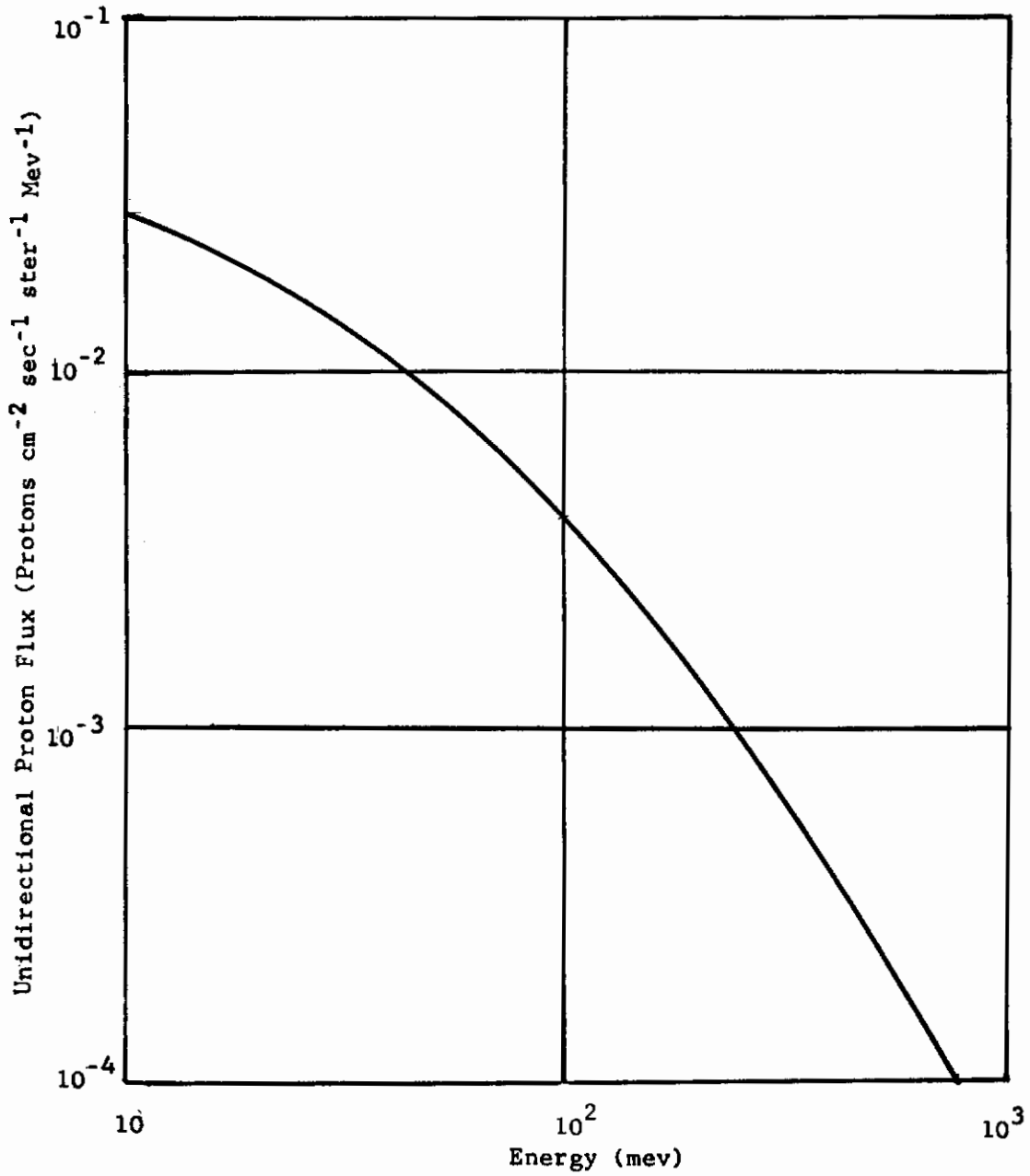


Figure 6. Composite Trapped Proton Spectrum

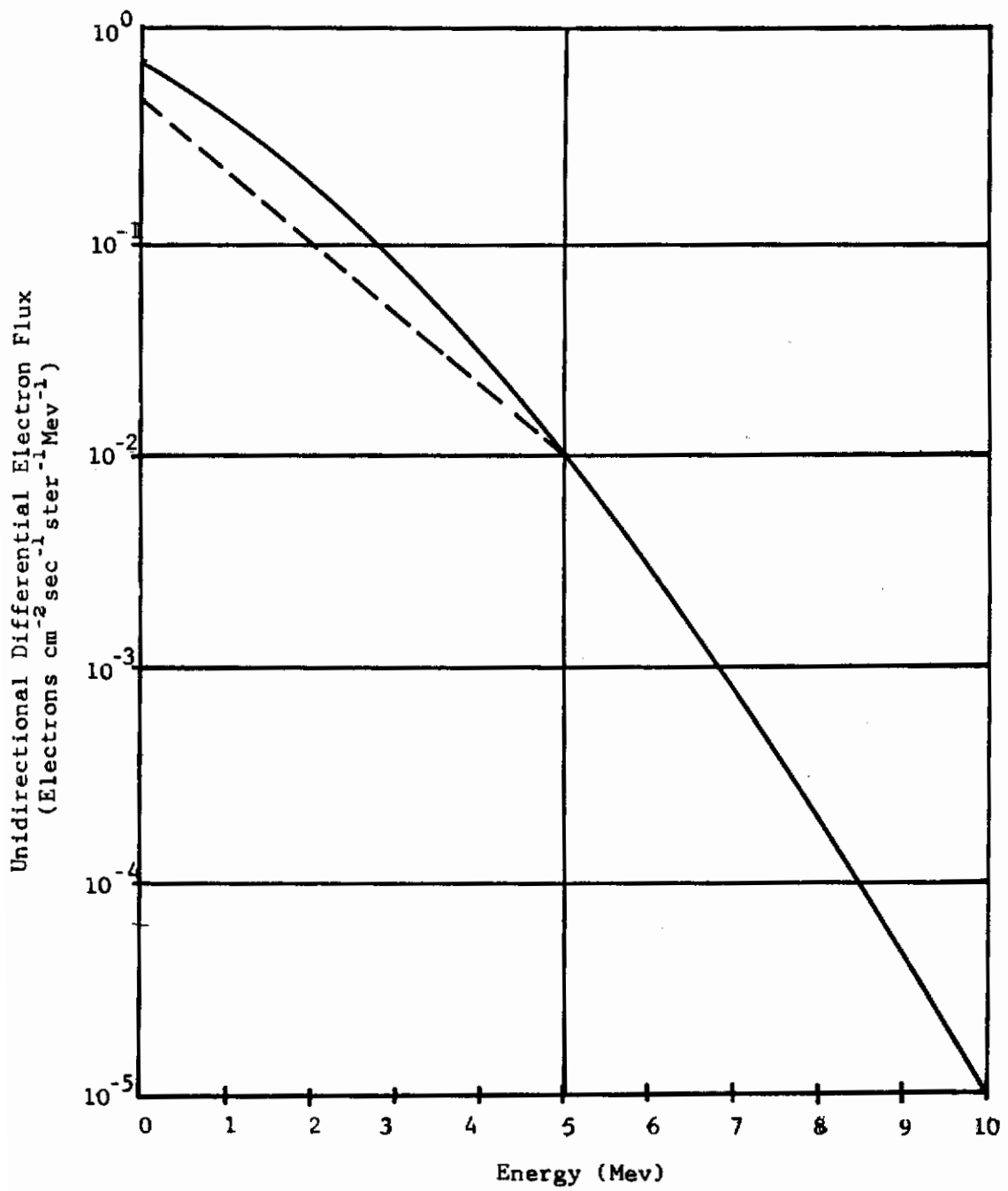


Figure 7. Artificial Belt Electron Spectrums

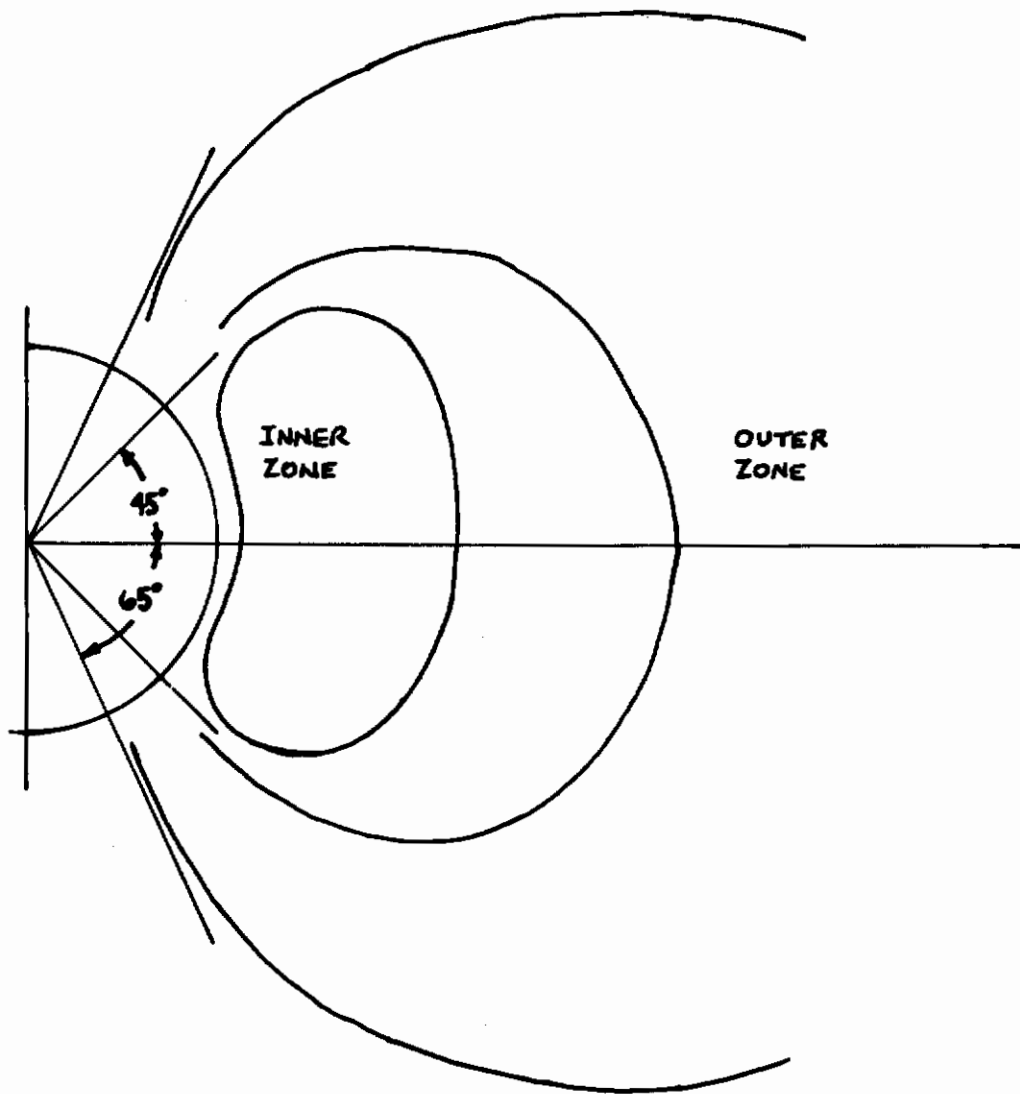


Figure 8. Van Allen Zones - Idealized Cross Section

The proton flux in this zone has been measured, and reached $10^9 \text{ cm}^{-2} \text{ sec}^{-1}$ between 120 kev and 4.5 Mev during August 1961 (ref 19). These comparatively low energies are not hazardous to manned space vehicles.

Electrons with energies up to approximately 5 Mev have been observed in the outer zone. Table 3 gives measured fluxes and energies for September 1961 (ref 19).

TABLE 3

ELECTRON FLUXES AND ENERGIES IN THE
OUTER VAN ALLEN ZONE

Energy	Flux (electrons $\text{cm}^{-2} \text{sec}^{-1}$)
45 kev < E < 60 kev	9×10^7
80 kev < E < 110 kev	8×10^7
110 kev < E < 1.6 Mev	$> 10^8$
1.6 Mev < E < 5 Mev	2×10^5
E > 5 Mev	$> 10^3$

Figure 9 shows the differential energy spectrum for outer zone electrons. The spectrum is normalized to 1 electron $\text{cm}^{-2} \text{sec}^{-1} \text{ster}^{-1}$ for E > .1 Mev.

For the calculation of the dose received by an astronaut orbiting in the Van Allen zones, it is assumed that it is necessary to consider only the protons from the inner zone and the electrons from the artificial zone. The inner zone electrons cannot be distinguished from the artificial belt electrons and in the available data it is assumed the flux of electrons at low altitudes consist entirely of those from the artificial belt. The outer zone electrons have a relatively low flux compared to that of the artificial belt and the outer zone protons have low energies; therefore, these particles are neglected in the dose calculations.

2.3 SOLAR FLARES

A solar flare is defined as the optical brightening of active regions on the sun; however, certain solar flares have associated with them the ejection of charged particles from the active regions. These particles

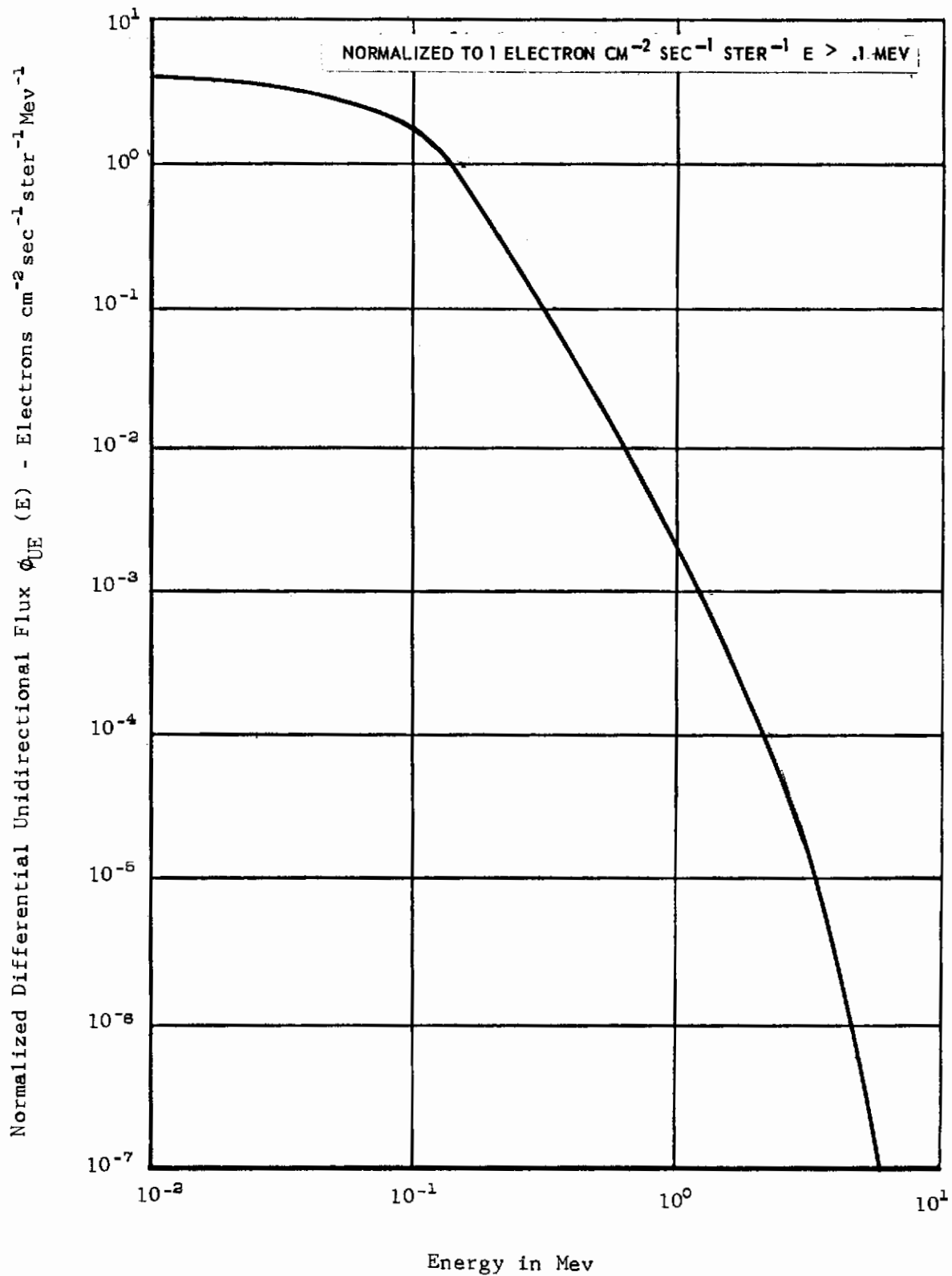


Figure 9. Outer Van Allen Zone Electron Spectrum

Contrails

may impinge upon the earth's magnetosphere and on occasion penetrate to the surface of the earth. Even though other phenomena such as radio and X-ray emission are associated with solar flares, only the particles ejected from the active region are considered hazardous to manned space flight. Only approximately 4 percent of the total number of flares observed on the sun produce particles that are detected in the vicinity of the earth; thus, the probability of encountering these particles is low, but because of the high intensities involved, this hazard is considered.

Solar flare particles consist mainly of protons, with a small percentage of heavier particles included in the total composition. The energies associated with these particles range from a few Mev to several Bev. Those solar flares that produce particles, observable at earth, are termed solar cosmic ray events (SCR), and are the events of importance to studies of radiation protection. These studies are hampered by the variability of occurrence and spectra of SCR events. The form of the flux-energy spectra for several important SCR events is shown in table 4. The starred events refer to data reported by Bailey (ref 20) and are shown in figure 10. Figure 11 shows the integral proton spectra for several other SCR events which were recorded by Winckler (ref 21). Figure 12 relates the time variation of the proton intensities for various events. The points indicated on the curves are the times at which the spectra of figure 11 were measured.

The above data are representative of solar particle characteristics in the magnetosphere. No rigorous single spectrum can be specifically defined; however, Bailey (ref 20) has developed an idealized evolution of the integral spectrum for a SCR event. This spectrum is shown in differential form in figure 13. The dashed curves indicate an extrapolation to longer times than Bailey originally presented. While this variation of spectrum with time is an idealized model, the time history corresponds to data presented by Bryant (ref 22) on the September 28, 1961 flare, which was observed outside the magnetosphere.

Solutions to the problem of protecting personnel from the radiation of solar flares are divided into two approaches:

- (a) prediction of the occurrence of an SCR event in time to abort any planned mission, and
- (b) shielding the spacecraft against the radiation.

Approach (a) has been investigated from the standpoint of correlating certain solar indices, such as plage size and radio noise, to the occurrence of an SCR event (refs 23 and 24). The approach is limited by incomplete knowledge of the flare process itself, and of the solar indices

Contrails

Event No.	Flare Date, (UT)	Spectra Measured, Date (UT)	ΔT (Hrs)	Differential $N(E)=CE^*$ (MEV)		Integral $N(>E)=CE^*$		Rigidity Spectra (MV)	Lit. Source	Remarks
				C	γ	C	γ			
1*	23 FEB 56	24 FEB 2100	17 1/2					$\propto R^{-4}$	46	2-100 MEV
2*	SAME	SAME	SAME					SAME	46	SAME
3*	SAME	SAME	SAME					R^{-2}		$R \leq 5 \times 10^8$ VOLTS
4*	TYPICAL EVENT								46	40-300 MEV
5	23 MAR 58 0950	24 MAR 58 1300-1400	78			7.2×10^3	2.7		47	
6	22 AUG 58 1417	23 AUG 0500	13			8.8×10^7	4		47	
6*	22 AUG 58	23 AUG 0430	14				4		46	100-500 MEV
7	22 AUG	---	---		3	5×10^8	4		48	
8	10 MAY 59 2055	12 MAY 0500	32			2.5×10^9	5		47	
8*	10 MAY 59	12 MAY 0530	32-1/2					$\propto R^{-6.8}$	46	110-240 MEV
9	10 MAY 59	---	---				4.8	$N(>7R) = 7.5 \times 10^3 R^{2.8}$ $= 2 \times 10^{-1} R^{-1}$ $= \text{see star}$	49	110-220 EV
10	19 MAY 59	12 MAY 0539 0539-0600 0600-0940 0940-1300		2.47×10^9 1.43×10^9 1.23×10^6 7.46×10^3		4.8 4.8 3.5 2.8			50	E>100 MEV
11	10 JULY 59 0210	11 JULY 1800-1400	34						47	
11*	10 JULY 59	11 JULY 1430	34-1/2				4		46	210-300 MEV
12*	10 JULY 59	12 JULY 1430	40-1/2				4		46	110-300 MEV
13	14 JULY 59 0323	15 JULY 1030	31			1.1×10^8	2.9		47	
13*	14 JULY 59	15 JULY 1044	31-1/2				2.9		46	88-300 MEV
14	14 JULY 59	15 JULY							51	<400 MEV
15	16 JULY 59 2200	---	---			1.5×10^{11}	4		52	85-300 MEV R^{-2} ($t > 1.2$ DAYS)
16	1 APR 60 0643	1 APR 0945	1				2.4		47	
17	1 APR 60	---	---			3.1×10^4	2.4		53	18-400 MEV
18	4 MAY 60 1020	4 MAY 1700-2300	11							
19	4 MAY 60 1020	1700-4 MAY TO 0200 5 MAY				3.8	1	$\frac{dN}{dR} = 8.5 \times 10^{-4} R^{-1.1}$	54	$n=2$ $(0.7 - 1.6 \text{ kv})$ $n^{-1} \text{ ev}^{-1}$
20	3 SEPT 60 0040	3 SEPT 1400	12						47	10 - 300 MEV
21*	3 SEPT 60 0640	3 SEPT 1408	13-1/2						46	20 - 180 MEV
22*	3 SEPT 60 0040	3 SEPT 1730	17						46	20-220 MEV
23	3 SEPT 60 0040	3 SEPT	<48	8×10^8 $(M^{-2} \text{ sec}^{-1} \text{ ster}^{-1} \text{ mev}^{-1})$					55	165 - 1050 MEV
24	3 SEPT 60 0040	4 SEPT	<48	3.4×10^8 (M^{-2})		3			55	135-110 MEV
25	3 SEPT 60 0040	4 SEPT	<48	1.8×10^8		3			55	75-800 MEV
26	12 NOV 60 1322	13 NOV 2000	31						47	
27*	12 NOV 60 1322	12 NOV 1840	5-1/2						46	2-350 MEV
28*	12 NOV 60 1322	13 NOV 1603	26-1/2						46	4-775 MEV

Table 4. Solar Flare Data

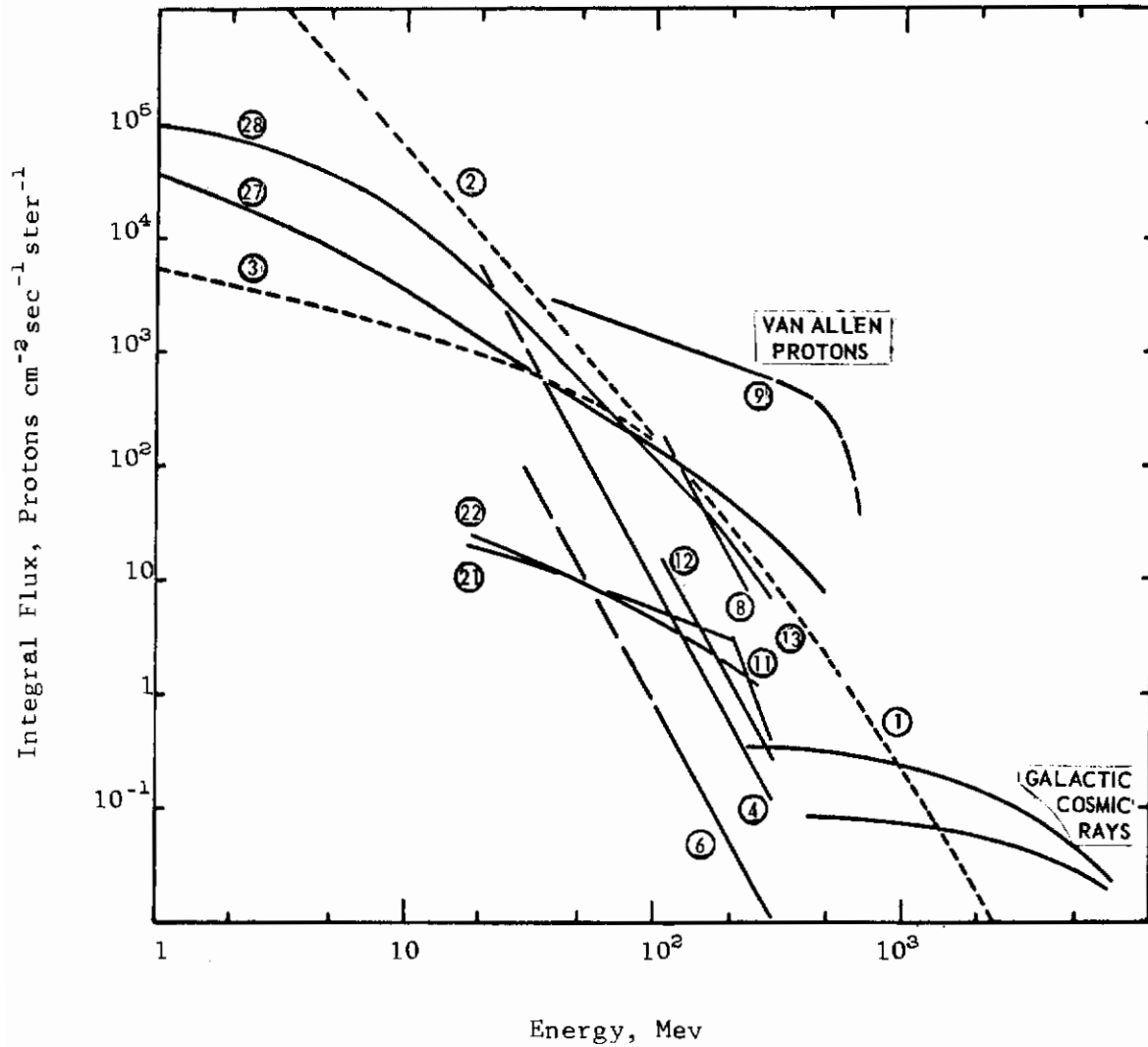


Figure 10. Integral Proton Energy Spectra (Bailey)

Contrails

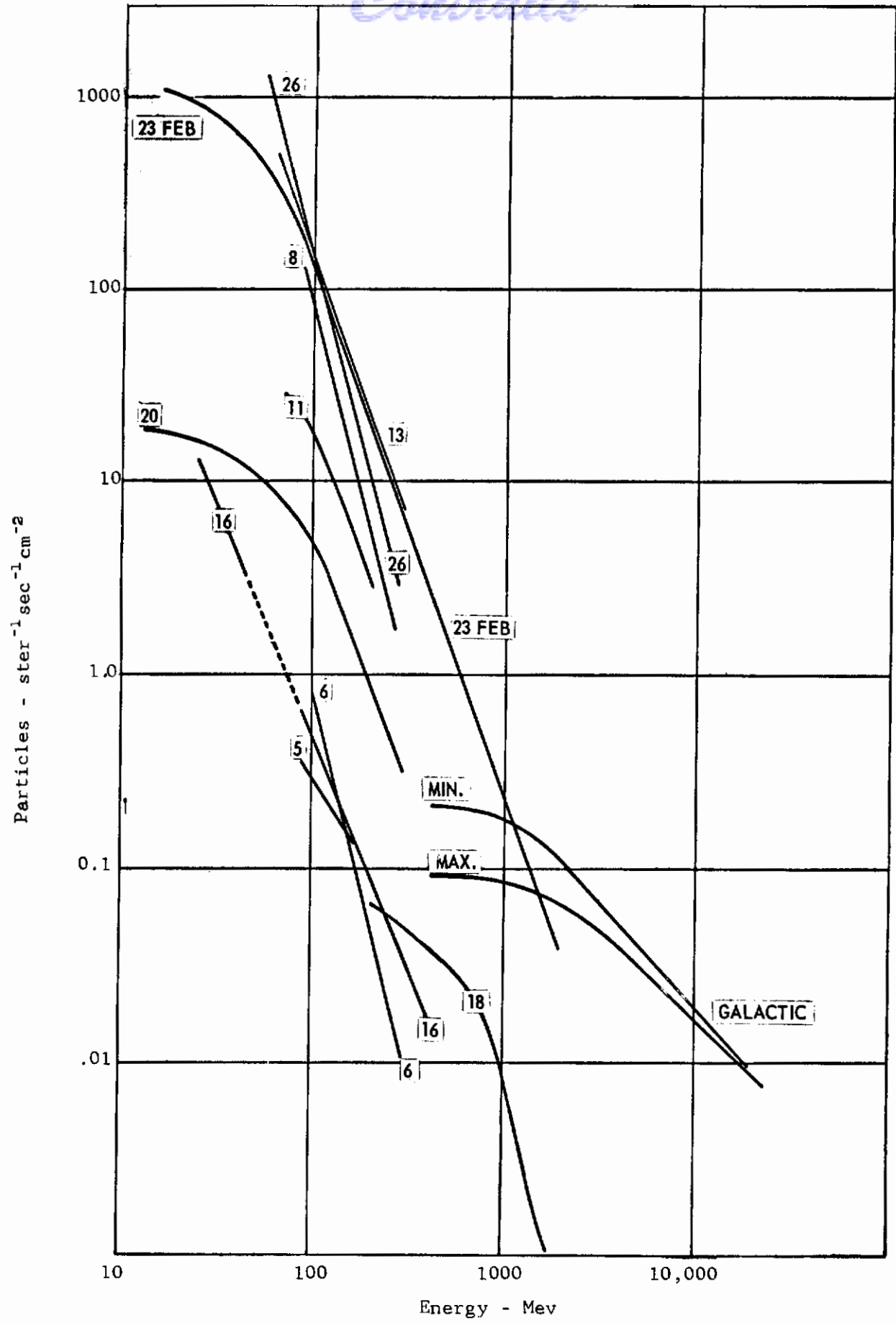


Figure 11. Integral Proton Energy Spectra (Winckler)

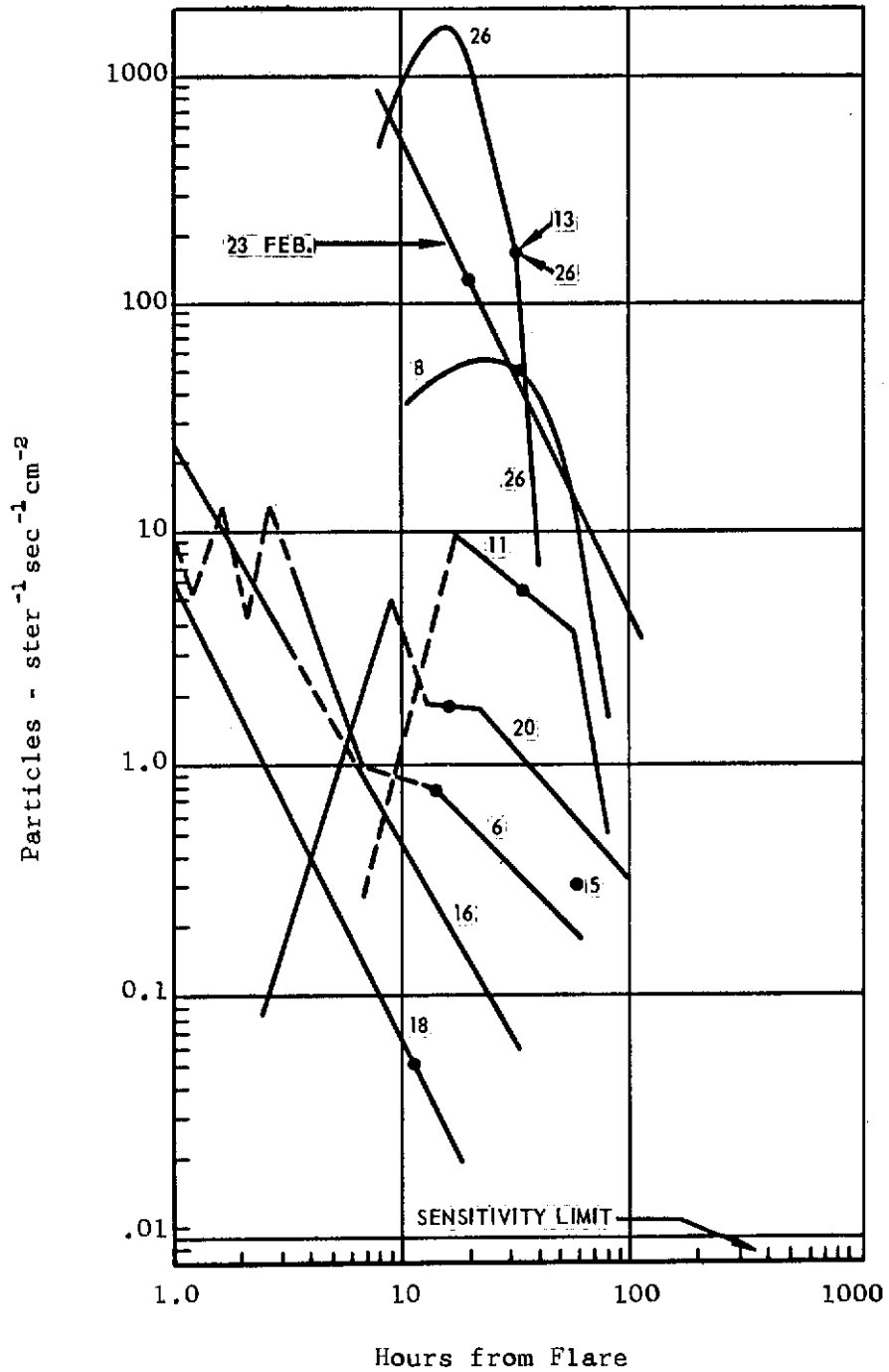


Figure 12. Time Variation of Solar Cosmic Ray Proton Spectra

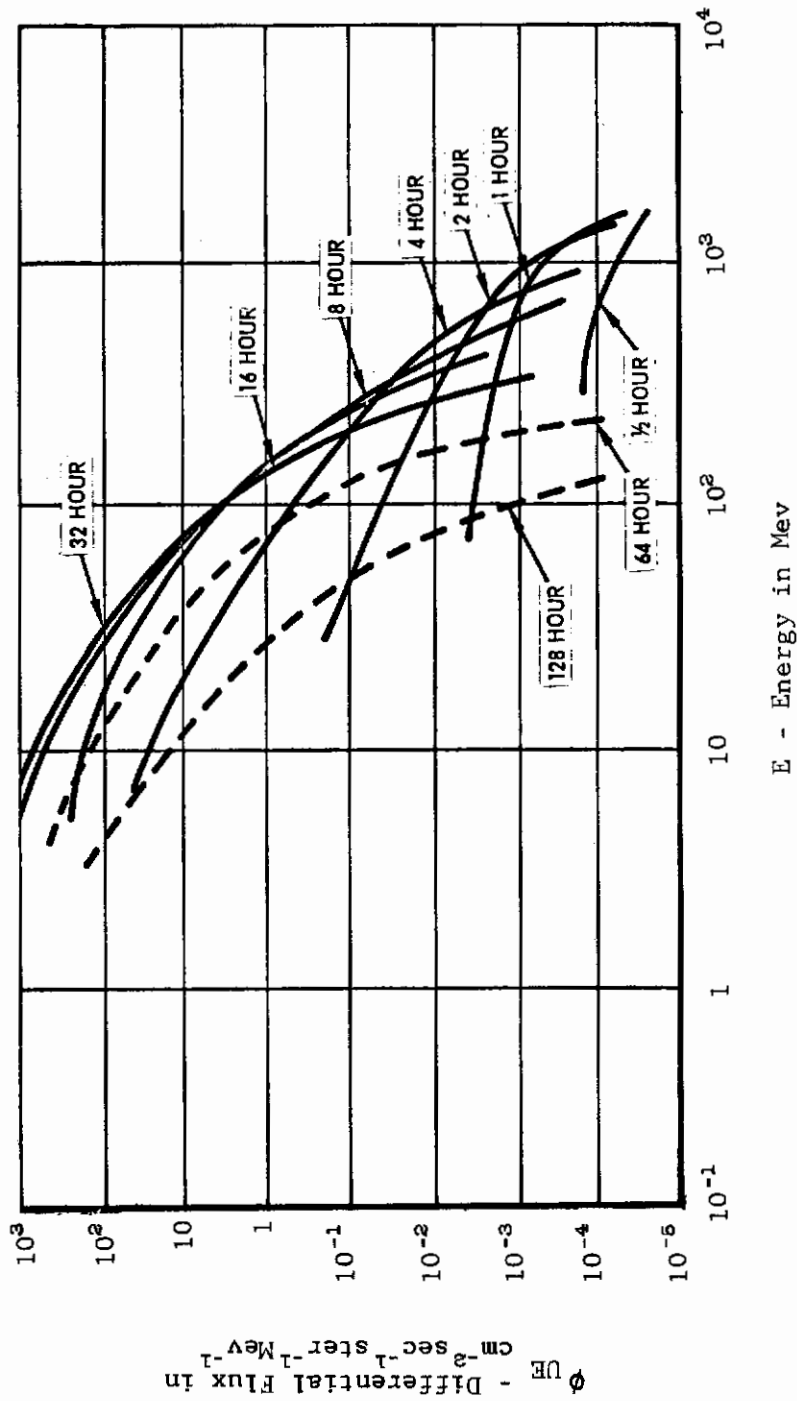


Figure 13. Model Solar Flare - Differential Flux

which could be used for long range prediction. Visual observations of active regions on the sun can give a 4 or 5 day prediction, but for longer duration missions, this approach is not reliable.

The second approach seems more feasible for manned military missions of long duration; however, an analytical analysis is complicated by the variability of individual SCR events. The choice of a "typical" flare to utilize in shielding calculations is risky, at best. A statistical method which utilizes an integral size versus frequency of occurrence distribution for SCR events over 4 years has been developed by Chupp, et al (ref 25) and in the Apollo statement of work (ref 26). These distributions rely heavily on the interpretation of SCR data to give the integral intensity of each event, and result in uncertainty in the distribution function which is obtained.

An alternative method to shielding against one flare has been developed by McDonald (ref 27). A graph of intensity versus time for all recorded events is constructed. At the present time the graph would include flares over most of one solar activity cycle (cycle 19). A curve slightly greater in value than the peak intensity of each individual even would constitute an envelope flare, larger than any single recorded event. An envelope flare, figure 14, obtained by NASA Goddard, is utilized in the dose calculations. It has been normalized to one particle $\text{cm}^{-2}\text{ster}^{-1}\text{E} > 100$ Mev for utilization in the dose analysis.

Sections 2.4, Galactic Cosmic Rays, and 2.5, Solar Wind, are included only for completeness of the description of the radiative environment. These components become important only for extremely long duration missions, and the solar wind is important only outside the magnetosphere. Usually it is better not to shield against the radiation from galactic cosmic rays, since the nuclei deposit only a small fraction of their energy in the material as they pass through it, and a collision with particles in the shield could trigger a large cascade of secondary particles. The solar wind, directly, can cause sputtering on exposed vehicle surfaces; however, this would be critical only to certain optical or thermal equipment. Indirectly, the solar wind affects the penetration of solar flare particles into the earth's field by its compression of the field.

2.4 GALACTIC COSMIC RAYS

Galactic cosmic rays consist almost entirely of stripped nuclei, mostly hydrogen, with kinetic energies on the order of, or very much greater than their rest mass. Table 5 lists the relative abundances of nuclei in cosmic radiations.

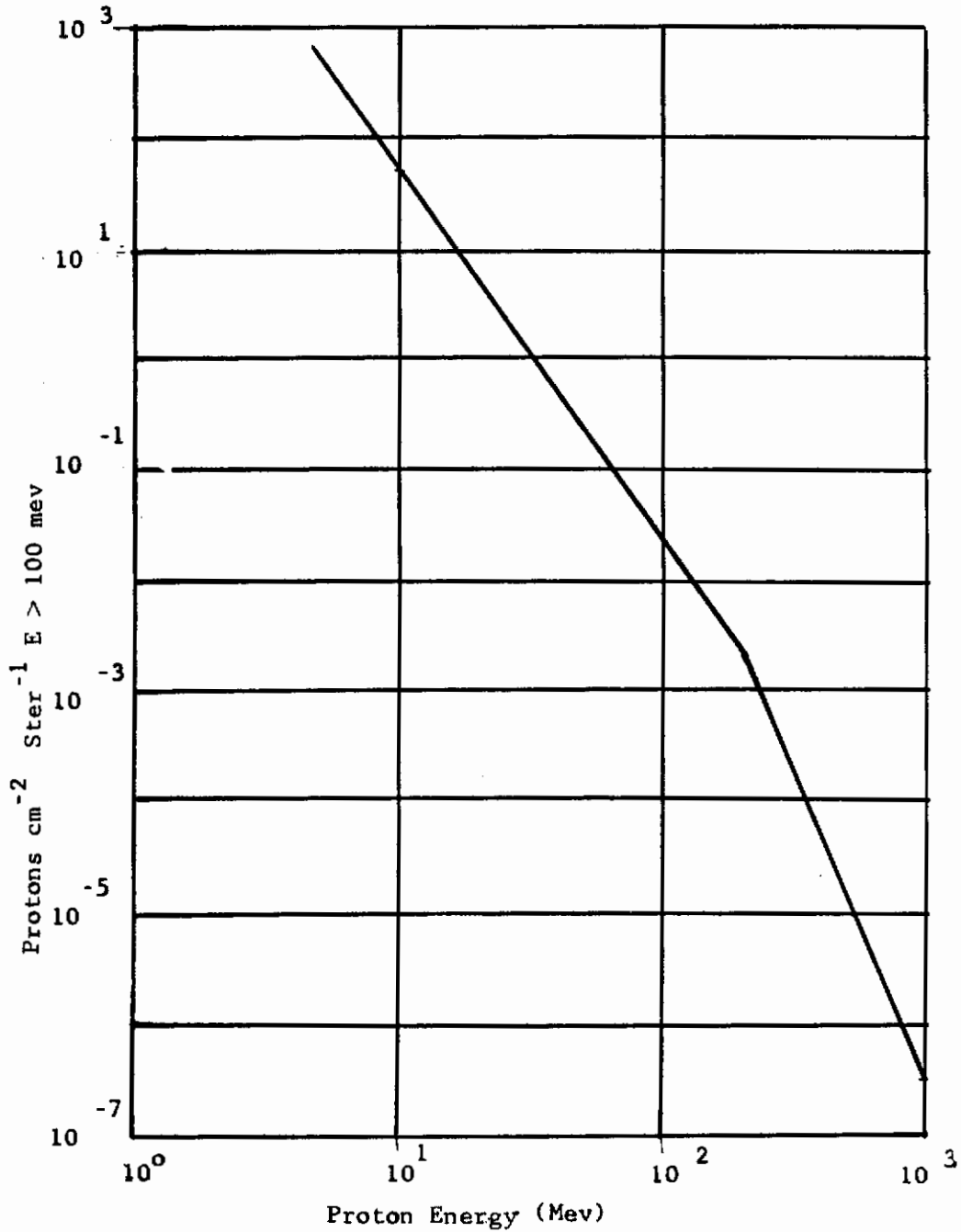


Figure 14. Envelope Flare

TABLE 5

RELATIVE ABUNDANCES OF NUCLEI
IN COSMIC RAYS

Element	Abundance (%) at Comparable Magnetic Rigidities
Hydrogen	~ 86
Helium	~ 13
Elements with $z \geq 3$	~ 1.4

At present there is no definite evidence of cosmic ray primary particles other than the nuclei $1 < Z < 26$ and electrons; however, studies are being made to determine if high-energy gamma-rays and neutrons can be detected in the cosmic ray flux. The percentage of electrons in cosmic radiation is small but measurable. Meyer and Vogt (ref 28) have placed an upper limit of 3 percent within the range 0.1 to 1.3 Bv.

Cosmic ray intensity at energies above 10 Mev per nucleon is nearly constant in time and isotropic in its direction of incidence upon the earth. Variations that do occur are mainly at lower energies and are the result of solar activity. Solar modulation of galactic cosmic radiation by the emission of plasma clouds, shield the earth from the lower energy primaries. This phenomenon is known as a Forbush decrease. Solar modulation, in addition to producing changes of a few days duration, also follows the 11-year solar cycle. At high latitudes, the magnetic shielding of the ionized gas from the sun reduces the overall cosmic ray intensity at the solar activity maximum by a factor of 2 to 4 below its mean value during the quiet part of the solar cycle. This reduction of intensity occurs with a time lag of approximately one year after solar maximum, and involves mainly cosmic rays in the 0.5 to 30 Bev range.

Galactic cosmic rays occur in space with a low intensity of approximately $2 \text{ particles cm}^{-2} \text{ sec}^{-1}$, but the energy range associated with these particles ranges from $\sim 10^8$ Mev to perhaps as high as 10^{13} Mev. The energy spectrum can be represented by

$$N(E) dE = dE / (1+E)^n \tag{13}$$

where

$$n = 2.1 \text{ for } 2 < E < 15 \text{ Bev}$$

$$n = 2.5 \text{ for } E > 15 \text{ Bev}$$

The flux-energy spectrum for galactic cosmic rays is shown in figure 15.

2.5 SOLAR WIND

The solar wind consists of an ionized plasma emitted continuously by the sun. Its existence was inferred by Biermann (ref 29) when he concluded that an outward streaming of gas from the corona could account for the observed motions of comet tails. In 1958, E. N. Parker (ref 30) proposed that this gas resulted from the hydrodynamical expansion of the corona, and the gas, which he called the solar wind, should have a velocity at the orbit of the earth of 150-500 km sec⁻¹. The solar wind exhibits an increase in flux and energy during periods of increased solar activity. Table 6 gives values of the flux of particles for both quiet and enhanced periods of solar activity.

When the solar wind encounters the earth's magnetosphere the force it exerts on the magnetic field tends to flatten the magnetosphere on the sun side of earth. Because the low energy particles cannot penetrate into the field, the magnetosphere acts like a solid object "carving out a hollow" in the solar stream. The solar wind particles passing around the magnetosphere extend the field lines away from the night side, and the magnetosphere becomes tear-shaped. (See figure 16.) The compression of the earth's field will continue until the energy density of the field becomes comparable to the kinetic energy density of the solar wind. An increase in solar activity and the subsequent increase in the solar wind velocity causes more compression on the sun side of the field; thus, the boundary of the magnetosphere may vary between 7 to 10 earth radii on the sun side. The night side of the field may extend to 20 earth radii or more.

For manned space missions - either earth orbital or lunar - the components of the radiative environment that are considered, in this study, as important in dose calculations are the protons from the inner Van Allen zone, the electrons from the artificial radiation belt, and solar flare protons. It is with these three components that the radiation penetration of the vehicle and dose calculations are made.

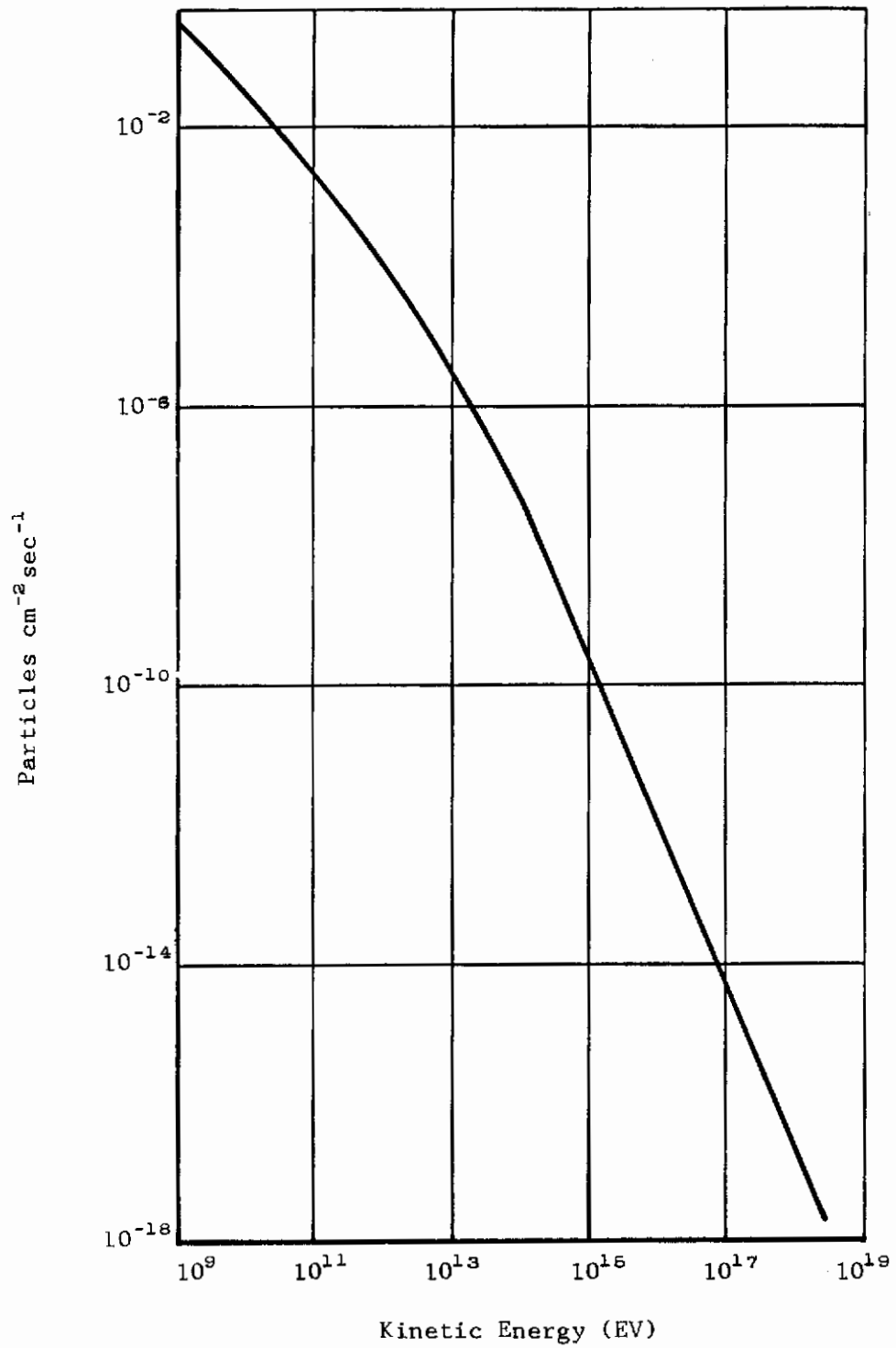


Figure 15. Spectrum of Galactic Cosmic Rays

TABLE 6

SOLAR WIND

Particles	Flux (Particles $\text{cm}^{-2}\text{sec}^{-1}$)	Energy (ev)
Protons	5×10^9 (normal) 2×10^{13} (enhanced)	2×10^3 2×10^4
Electrons	5×10^9 (normal) 5×10^{13} (enhanced)	2 11

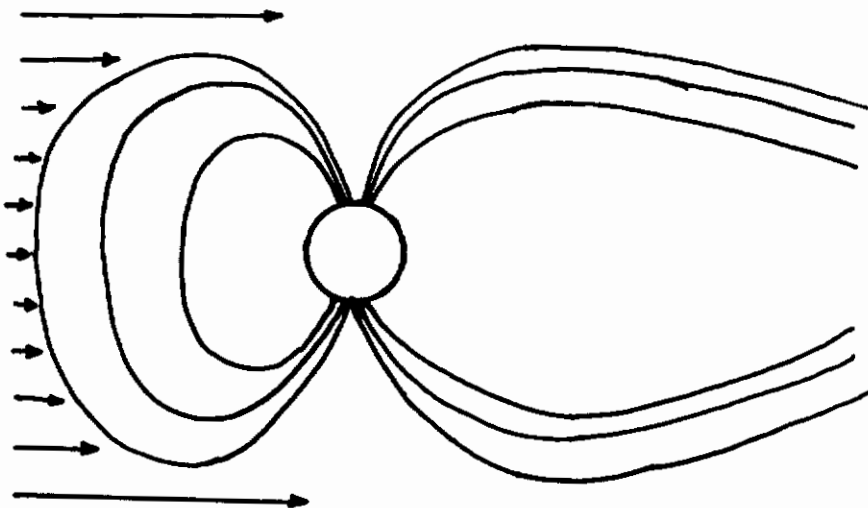


Figure 16. Interaction of Solar Wind with the Earth's Magnetic Field

SECTION 3

MISSION TRAJECTORIES

The radiative environment, described in Section 2, interacts with a vehicle executing a geocentric orbit or lunar mission. A computer program has been developed to determine the intensity of particles from the trapped radiation zones that impinges on such a vehicle (ref 31). The program also has provisions for the application of criteria for solar flare particles striking the vehicle. Galactic cosmic rays and the solar wind particles are not considered because of their relative unimportance to crew shielding problems.

The vehicle's position at various points along the trajectory is transformed from geographic coordinated to B,L coordinates, and in this form is compared to grids of magnetic field intensities and L values with their associated known particle intensities. Interpolation among the known B,L, and intensity values and the calculated B and L determines the particle intensity for B,L coordinates of the vehicle's position.

The following sections describe the three trajectories for which solutions have been developed, geocentric orbits, lunar transfer trajectories, and lunar return trajectories, and present the basic equations that were utilized. For the three types of trajectories, figure 17, the vehicle's latitude, longitude, and altitude as a function of time are determined. In order to simplify calculations, several assumptions were made:

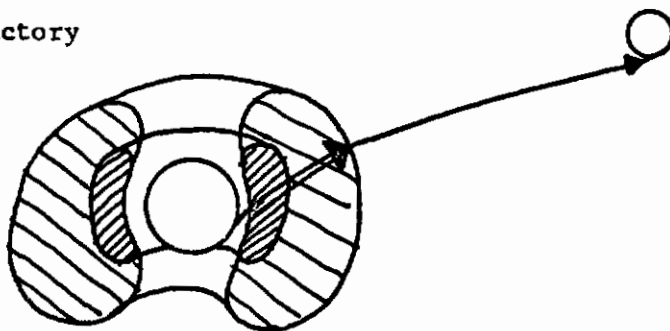
- (a) the earth is considered to be a sphere, not a geoid
- (b) the thrusting portion of the trajectory is not included in the calculations
- (c) atmospheric drag is neglected, and
- (d) the vehicle is at perigee at time zero.

3.1 GEOCENTRIC ORBITS

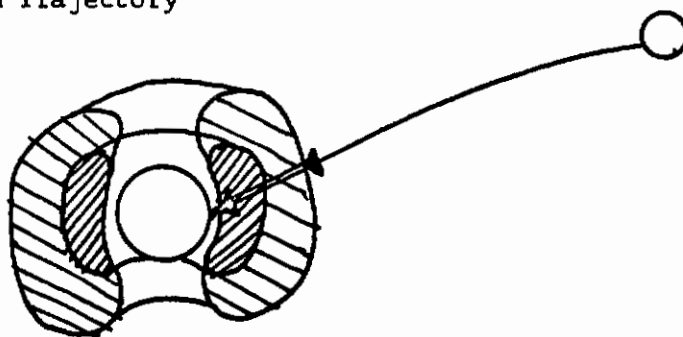
A geocentric equatorial coordinate system, figure 18, is used in the orbit analysis. The orbit is inclined at an angle i with the equator, and the vehicle is at perigee at time zero. Three unit vectors are defined within the coordinate system: \underline{P} , which is directed toward the perifocus; \underline{Q} , which is directed normal to the perifocus and in the plane of the orbit; and \underline{W} , which is directed normal to the orbit plane.

Contrails

1. Lunar Trajectory

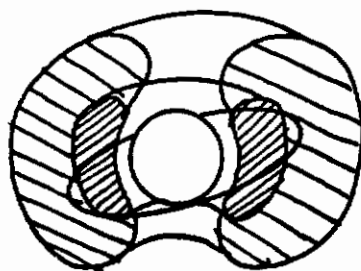


2. Lunar Return Trajectory



3. Geocentric Orbits

a.



b.

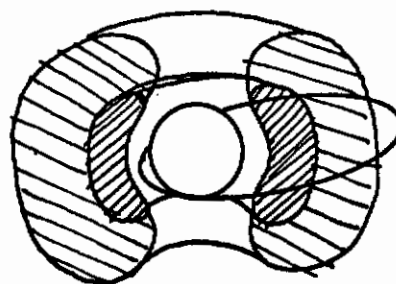


Figure 17. Trajectory Options

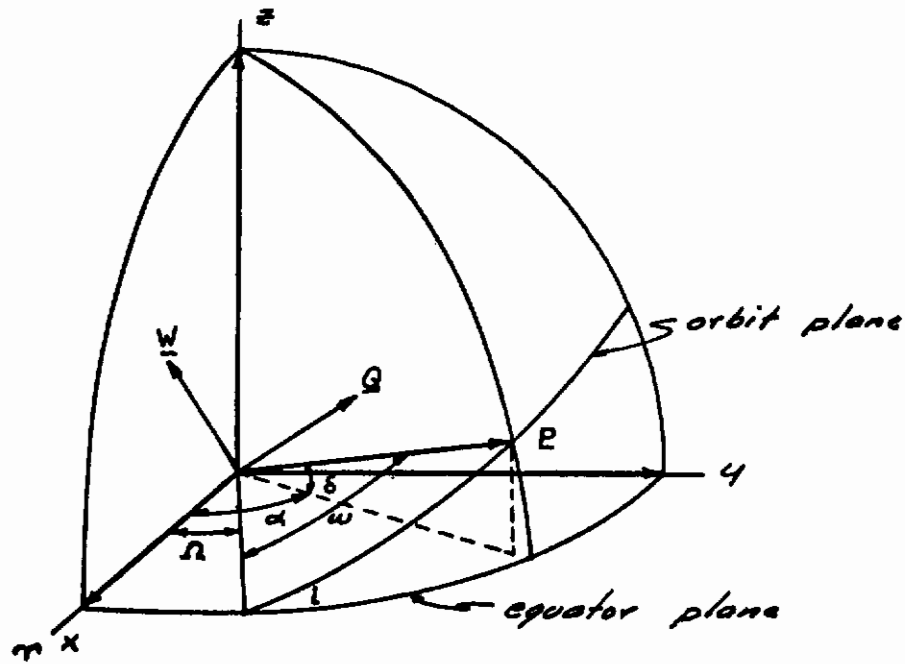


Figure 18. Equatorial Coordinate System

Contrails

Since the analysis is for a two-body orbit, the calculations of position are confined to the orbit plane, figure 19. Thus, for a desired time after initial perigee, T, the vehicle's x_w and y_w positions are determined and then transformed to the geocentric equatorial coordinates x, y, z .

The analysis of the position in the orbit plane are obtained using the following basic equations. For the trajectory (the ellipse) in figure 19,

$$\frac{r}{a} = 1 - e \cos E$$

where r = geocentric distance of vehicle

a = semi-major axis of ellipse

e = eccentricity of conic section

E = eccentric anomaly; the angle at the center of ellipse between axis and radius of an auxillary circle of radius a .

The time from perigee is given by

$$nT = E - e \sin E \quad (15)$$

where $n = 60 K_e \left(\frac{1}{a} \right)^{3/2}$ (16)

and K_e = square root of the product of the universal gravitational constant and the mass of the earth.

From equations 1 and 2,

$$\Delta E = n \frac{a}{r} \Delta T. \quad (17)$$

An iterative process is used: for a desired ΔT , an estimate of ΔE is obtained, the E being determined from

$$E_{i+1} = E_i + \Delta E. \quad (18)$$

A time, t_{C_1} , can be determined from equation 15. This time is a computed value for the time from perigee ($t_{C_1} \rightarrow \Delta T$). Also the difference

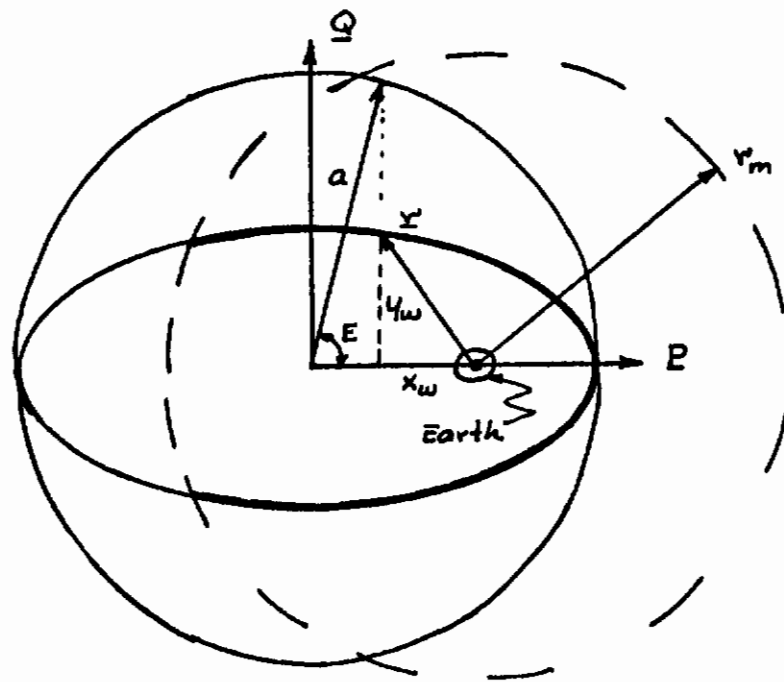


Figure 19. Orbit Plane Coordinate System

Contrails

between the desired time t_{c_2} and the actual time t_{c_1} , obtained from using ΔE from equation 17 can be computed by

$$(t_{c_2})_{i+1} = (t_{c_2})_{i+\Delta T} \quad (19)$$

and

$$\Delta t = t_{c_2} - t_{c_1} \quad (20)$$

If Δt is larger than a specified value the process is repeated until it is smaller.

When the proper value of E has been obtained, the position in the orbit plane is given by

$$x_w = a(\cos E - e) \quad (21)$$

$$y_w = a \sin E [1 - e^2]^{\frac{1}{2}} \quad (22)$$

and the geocentric equatorial coordinates are determined from

$$x = P_x x_w + Q_x y_w \quad (23)$$

$$y = P_y x_w + Q_y y_w \quad (24)$$

$$z = P_z x_w + Q_z y_w \quad (25)$$

Utilizing the earth's rotation rate of 15.041 degrees per hour, the vehicle's latitude and longitude are determined. The above procedure calculates one point on the trajectory; it is repeated until the total orbit time is reached.

At the end of each orbit two corrections for the oblateness of the earth can be added as discrete quantities. The semi-major axis can be rotated by incrementing the angle ω . This rotates P and Q in the plane of the orbit. Incrementing Ω rotates the right ascensions of P , Q , and W and corresponds to a regression of the orbit plane.

3.2 LUNAR TRANSFER TRAJECTORY

The fact that the lunar transfer trajectory is essentially two-body in nature until it reaches the sphere-of-influence of the moon is

utilized. This trajectory option is therefore assumed to be a geocentric orbit since only relative near-earth distances are considered. The lunar right ascension and declination, along with the latitude, longitude and time of perigee are used to determine the transfer orbit from which the \underline{P} , \underline{Q} , and \underline{W} vectors may be obtained.

The two-body orbit parameters may be determined to a reasonable accuracy after the semi-major axis has been estimated. For a given transfer trajectory time and lunar geocentric distance an expression for $1/a$ has been empirically determined from

$$\begin{aligned} 10^5/a = & -0.00052073t^3 + 0.19171t^3 \\ & -(23.882 + 0.05 r_g)t^2 \\ & +(1044.3 + 11.25 r_g)t \\ & -(692.5 r_g - 2031) \end{aligned} \quad (26)$$

where t = transfer trajectory time

r_g = lunar geocentric distance

After obtaining the orbital parameters, the vehicle's longitude, latitude, and altitude are determined in the same way as for geocentric orbits. The trajectory is considered complete when the vehicle reaches a specified maximum geocentric distance, which physically corresponds to the outer limit of particle data or the edge of the Van Allen zones.

3.3 LUNAR RETURN TRAJECTORY

The lunar return trajectory is handled as a retrograde transfer trajectory and therefore is essentially the same as a lunar transfer trajectory determination. In order for the return trajectory to reach a specified perigee point, either a direct or indirect trajectory may be considered; therefore, maximum trip time is utilized and all trajectories that do not exceed this time are calculated.

SECTION 4

RADIATION - MATERIAL INTERACTIONS

The interaction of radiation with matter must be described analytically in a manner to give useful results in radiation shielding. In the effort reported here the emphasis has been on the overall task without greatly refining the problem of radiation penetration. The two primary types of space radiation which are of importance are electrons and protons. As discussed in Section 2 the sources of concern are the artificial radiation belt for electrons; the inner Van Allen zone, and solar cosmic ray events for protons. Although electrons and protons are the primary radiation hazard, as they penetrate materials secondary radiation is produced which must be taken into account. This is especially true for the electrons. In the following discussion the physical processes involved are briefly discussed, after which, the mathematical formulation utilized in this study is presented.

4.1 ELECTRON INTERACTIONS

As electrons penetrate matter their energy is degraded by two processes: collisions with bound electrons and radiation in the electric fields of nuclei. The collision (ionization) process is dominant at the electron energies encountered in the artificial radiation belt, while the X rays produced by the radiative-loss mechanism (bremsstrahlung) are the biological hazard which prevails even after all the electrons have been stopped (5-6 gm/cm² of Aluminum). The processes of ionization and bremsstrahlung are important to electron shielding and are discussed below.

4.1.1 Ionization

Ionization is the principal energy-loss mechanism for energies less than the critical energy, where critical energy (E_c) is defined as that energy at which the ionization loss (energy transferred < 5 Mev) equals the radiation loss. For aluminum the critical energy is 47 Mev (ref 32), while the maximum electron energy considered for the fission electrons is 10 Mev. Electrons are relativistic even at fractional Mev energies; therefore, an expression for stopping power is required which is valid at relativistic energies. The following expression for electron stopping power, from reference 32, has been utilized in this study:

$$-\frac{1}{\rho} \frac{dE}{dx} = S(E) = \frac{2\pi N_0 e^4 Z}{mv^2 A} \left[\ln \frac{mv^2 E}{2I^2(1-\beta^2)} \right. \quad (27)$$

$$\left. - (2\sqrt{1-\beta^2} - 1 + \beta^2) \ln 2 \right.$$

$$\left. + 1 - \beta^2 + \frac{1}{8} (1 - \sqrt{1 - \beta^2})^2 \right]$$

Contrails

where $S(E)$ is in ergs $\text{gm}^{-1}\text{cm}^2$ and N_0 is Avogadro's number
 e = electron charge (4.803×10^{-10} esu)
 Z = atomic number
 m = mass of electron (9.108×10^{-28} gm)
 v = velocity of electron (cm sec^{-1})
 A = atomic weight
 c = velocity of light ($2.9979 \text{ cm sec}^{-1}$)
 E = electron energy (ergs)
 β = v/c

Equation 27 has been utilized to calculate the radiation dose due to electrons. A graph of electron stopping power versus energy for aluminum is presented. (See Figure 20.)

The range of electrons as a function of energy is complicated by multiple scattering with an electron able to lose up to one-half its energy in a single collision. There is a marked difference between the experimental maximum range (ref 33) and the computed path length (ref 34). Figure 21 illustrates this difference for the case of aluminum. The computed value is obtained from the integration of

$$\int_{\epsilon}^E \frac{dE}{S(E)} \quad (28)$$

where some very small energy ϵ is used as the lower limit of the integral since $S(E)$ is not known as the electron energy approaches zero. Therefore,

$$P(E) = P(\epsilon) + \int_{\epsilon}^E \frac{dE}{S(E)} \quad (29)$$

is utilized in obtaining computed electron path lengths based on the mean stopping power, $S(E)$. Computed results for many materials are presented in reference 34, with those for aluminum illustrated in figure. Related to electron range is the transmission factor, i.e., the fraction of electrons of a given energy which will penetrate through a distance X . This is illustrated in figure 22 and is based on Monte Carlo calculations (ref 35). As can be seen in figure 22, only approximately 50% of the electrons for a given energy penetrate one-half of R_{max} . This is for a beam of monoenergetic electrons and the actual fraction which penetrates through a given slab thickness is a function of electron energy.

The utilization of electron range and transmission factor in radiation shielding is presented in Section 4.2.

4.1.2 Bremsstrahlung

In most problems of a practical nature which deal with the passage of charged particles through matter, the effects of secondary radiation are usually of little importance. However, when the electrons trapped in the earth's magnetic field are stopped by the exterior of a space vehicle, then the secondary radiation, X rays, is the significant hazard even though only

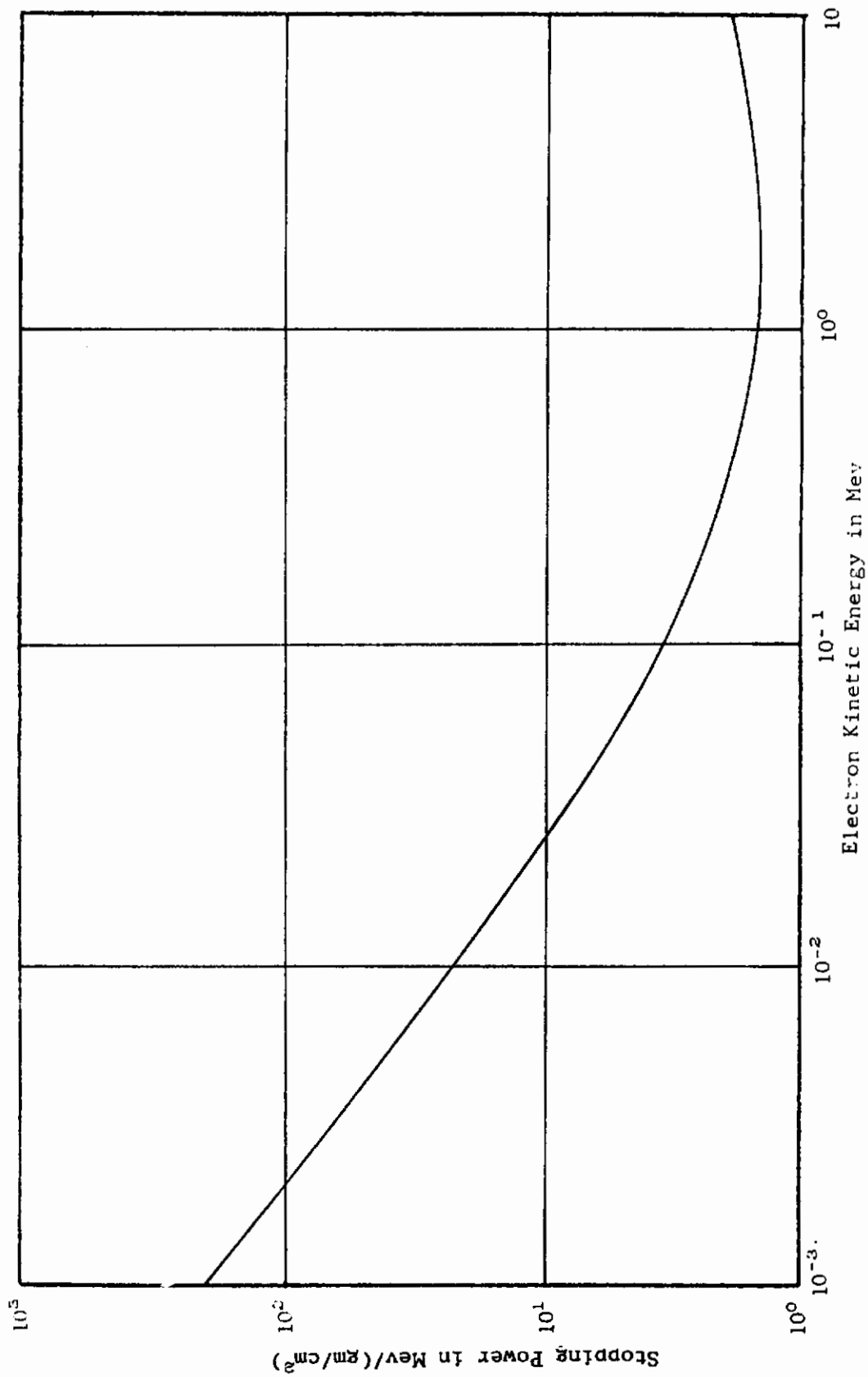


Figure 20, Electron Stopping Power for Aluminum

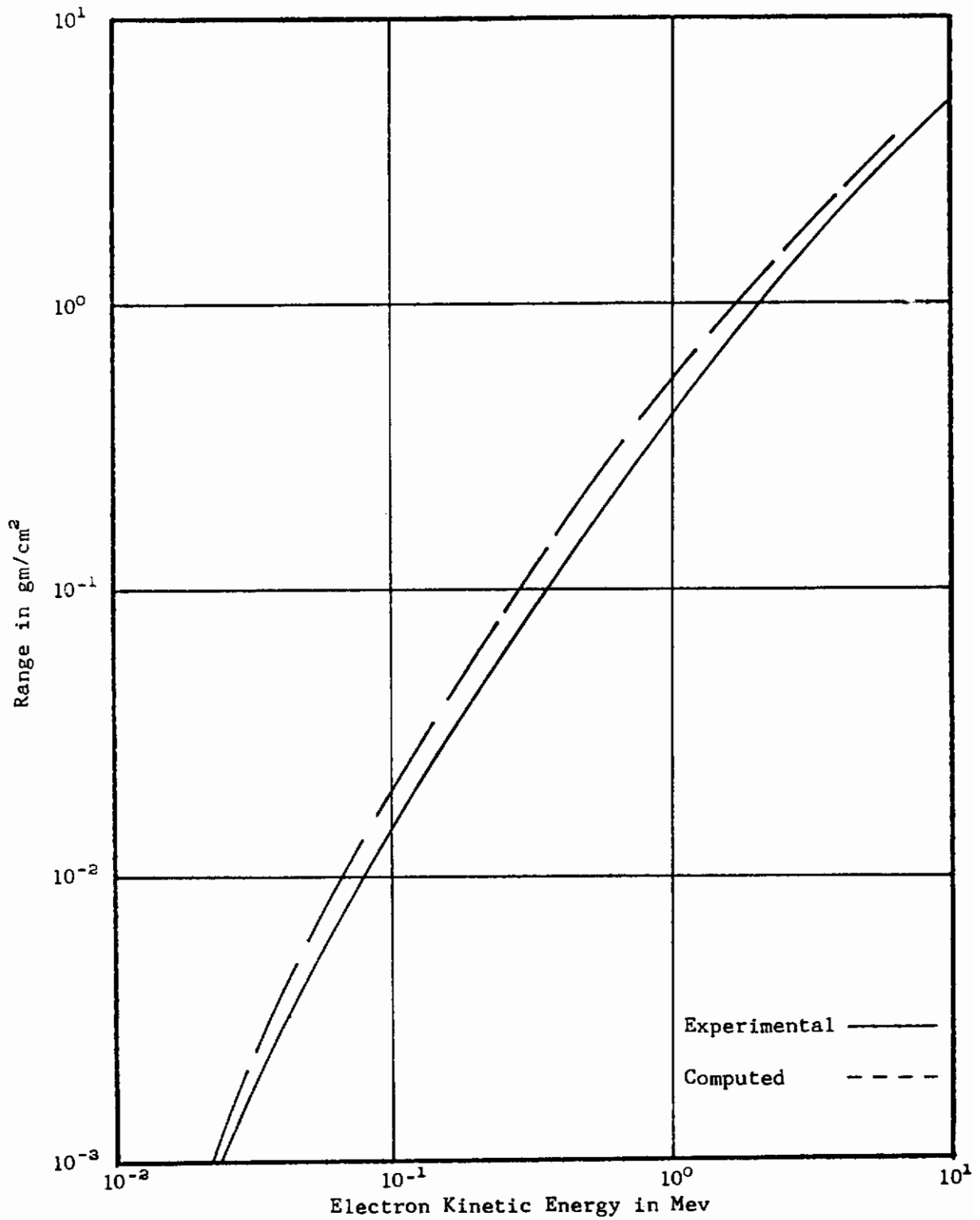


Figure 21. Range of Electrons in Aluminum

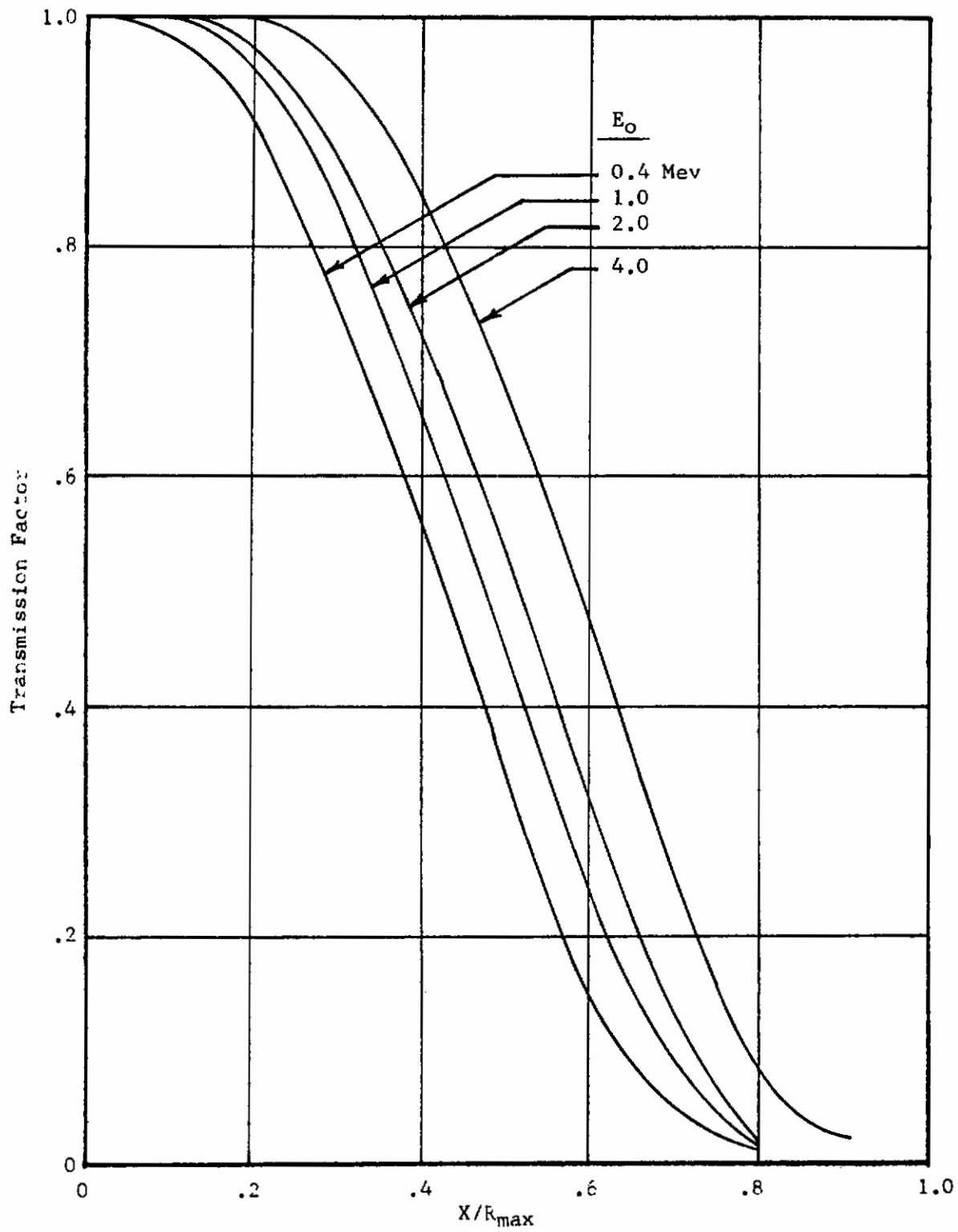


Figure 22. Transmission Factors at Various Energies for Electrons Normally Incident on Aluminum

a small fraction of the electron energy is converted into X rays. Equation 30 (ref 36) gives an approximation of this fraction.

$$\text{Fraction} \approx 7 \times 10^{-4} ZE \quad (30)$$

The bremsstrahlung produced is proportional to Z^2 , therefore the relative X rays produced in aluminum would be much less than in lead: $(13^2/82^2 = .025)$.

Monenergetic electrons produce a continuous spectrum of photon energies from zero energy up to a maximum energy equal to the energy of the electron. The continuous X-ray spectrum produced in aluminum is shown for several electron energies (ref 37). (See figure 23.) These spectra are severely modified at the low energy end due to absorption within the material itself. This is indicated qualitatively by the dotted curves in figure 23.

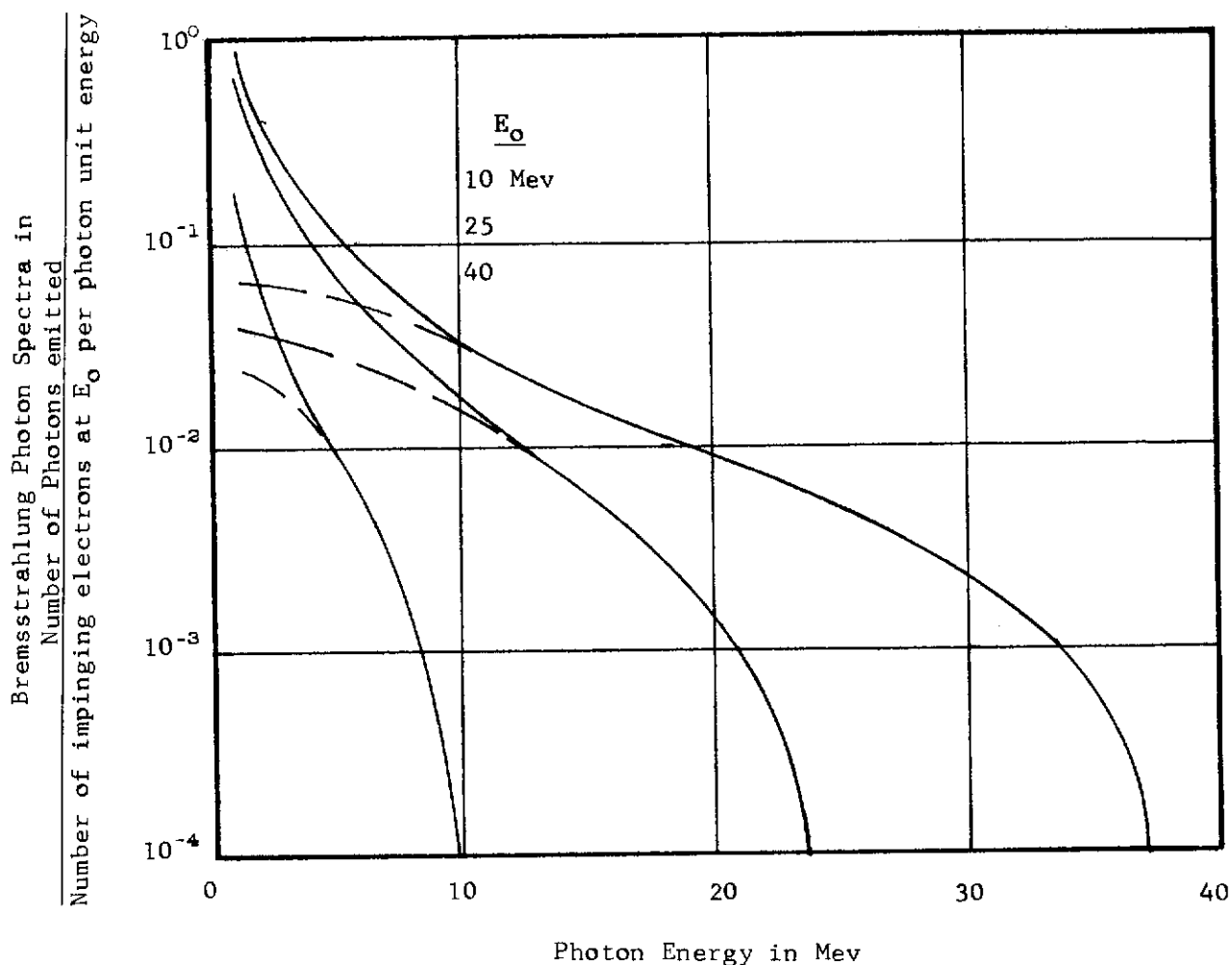


Figure 23. Thick-Target Bremsstrahlung Photon Spectra in Aluminum

Contrails

Numerous bremsstrahlung cross section formulas are presented in reference 38. Equation 31, which neglects screening, is valid for electrons of energies up to approximately 3 Mev for low-Z materials; at higher energies this equation gives a cross section which is higher than the correct value.

$$\frac{d\sigma_k}{dk} = \frac{Z^2 r_o^2 P}{137kP_o} \left\{ \frac{4}{3} - 2E_o E \left(\frac{P^2 + P_o^2}{P^2 P_o^2} \right) + \frac{\epsilon_o E}{P_o^3} + \frac{\epsilon E_o}{P^3} - \frac{\epsilon \epsilon_o}{P_o P} \right. \\ \left. + L \left[\frac{8EE_o}{3P_o P} + \frac{k^2 (E_o^2 E^2 + P_o^2 P^2)}{P_o^3 P_o} + \frac{k}{2P_o P} \left(\frac{E_o E + P_o^2}{P_o^3} \right) \epsilon_o \right. \right. \\ \left. \left. \left(\frac{E_o E + P^2}{P^3} \right) \epsilon + \left(\frac{2kE_o E}{P^2 P_o^2} \right) \right] \right\} \quad (31)$$

where

$$L = 2 \ln \left(\frac{E_o E + P_o P - 1}{k} \right), \quad \epsilon_o = \ln \left(\frac{E_o + P_o}{E_o - P_o} \right), \quad \epsilon = \ln \left(\frac{E + P}{E - P} \right)$$

- Z = atomic number of target material
- r_o = classical electron radius (2.82×10^{-13} cm)
- k = photon energy in mc^2 units
- P_o, P = initial and final momentum of electron in mc units
- E_o, E = initial and final total energy of electron in mc^2 units

The physical significance of this formula is that $\frac{d\sigma_k}{dk}$ is the differential cross section with respect to photon energy or, in other words, is the probability per atom of an electron having total energy E_o producing a photon in energy interval dk about photon energy k . The cross section σ_k , integrated over emission angle, represents the total cross section. Results for electron energies of 0.05 Mev and 0.5 Mev are presented in figure 24.

For electrons at energies in excess of a few Mev, some correction for screening is necessary in order to obtain greater accuracy. The following equation is valid for extremely relativistic electrons (ref 38):

$$\frac{d\sigma_k}{dk} = \frac{2Z^2}{137k} \left\{ \left[1 + \left(\frac{E}{E_o} \right)^2 - \frac{2}{3} \frac{E}{E_o} \right] \left[\ln M(0) + 1 - \frac{2}{b} \tan^{-1} b \right] \right. \\ \left. + \frac{E}{E_o} \left[\frac{2}{b^2} \ln(1+b^2) + \frac{4(2-b^2)}{3b^2} \tan^{-1} b - \frac{8}{3b^2} + \frac{2}{9} \right] \right\} \quad (32)$$

where
$$b = \frac{2EE_0Z^{1/3}}{111k} ; \frac{1}{M(O)} = \left(\frac{k}{2E_0E} \right)^2 + \left(\frac{Z^{1/3}}{111} \right)^2 \text{ and}$$

the symbols are as previously defined. Results for electron energies of 5 Mev, 50 Mev, and 500 Mev are presented. (See figure 24.)

4.2 ELECTRON SHIELDING CALCULATIONS

An analytical expression for the electron energy as a function of depth of penetration has been formulated for use in shielding calculations. This expression is of the form:

$$E = E_0 \left(1 - \frac{X}{R(E_0)} \right)^n \quad (33)$$

where

- E = emerging electron energy (Mev)
- E₀ = incident electron energy (Mev)
- R(E₀) = range of electron at energy E₀ (gm cm⁻²)
- X = depth of penetration (gm cm⁻²)
- n = exponent which is a function of material and electron energy

The range values utilized are experimental values for aluminum from reference 33 and not the computed path-length values. Figure 25 illustrates the electron energy (E/E₀) as a function of X/R(E₀) for electrons from 0.01 to 10 Mev, the energy range of interest. It is assumed in equation 33 that all electrons of a given energy penetrate a depth equal to their maximum experimental range, and that all electrons have the same energy at a given X. While this is not the actual case, the primary interest is in the bremsstrahlung produced and not the electron dose; the X rays are produced principally near the surface and hence the depth of electron penetration is not very critical. Table 7 lists the fraction of the X-ray dose received, inside of 5.4 gm cm⁻² of aluminum, due to bremsstrahlung production in each tenth of the thickness assuming an impinging beam of electrons distributed in energy according to figure 7. Attenuation of the X rays within the shield is included in the calculation (ref 39).

As can be seen from table 7 the bremsstrahlung produced by the electron spectrum is highly peaked toward the outside surface. Therefore, a small error is introduced in assuming that electrons penetrate perpendicularly to the shield instead of isotropically. The latter is approximately the case within the Van Allen zone. Even so, two additional approximations have been formulated to improve the estimate of the X-ray dose. First a transmission factor has been utilized, based upon reference 35, such that,

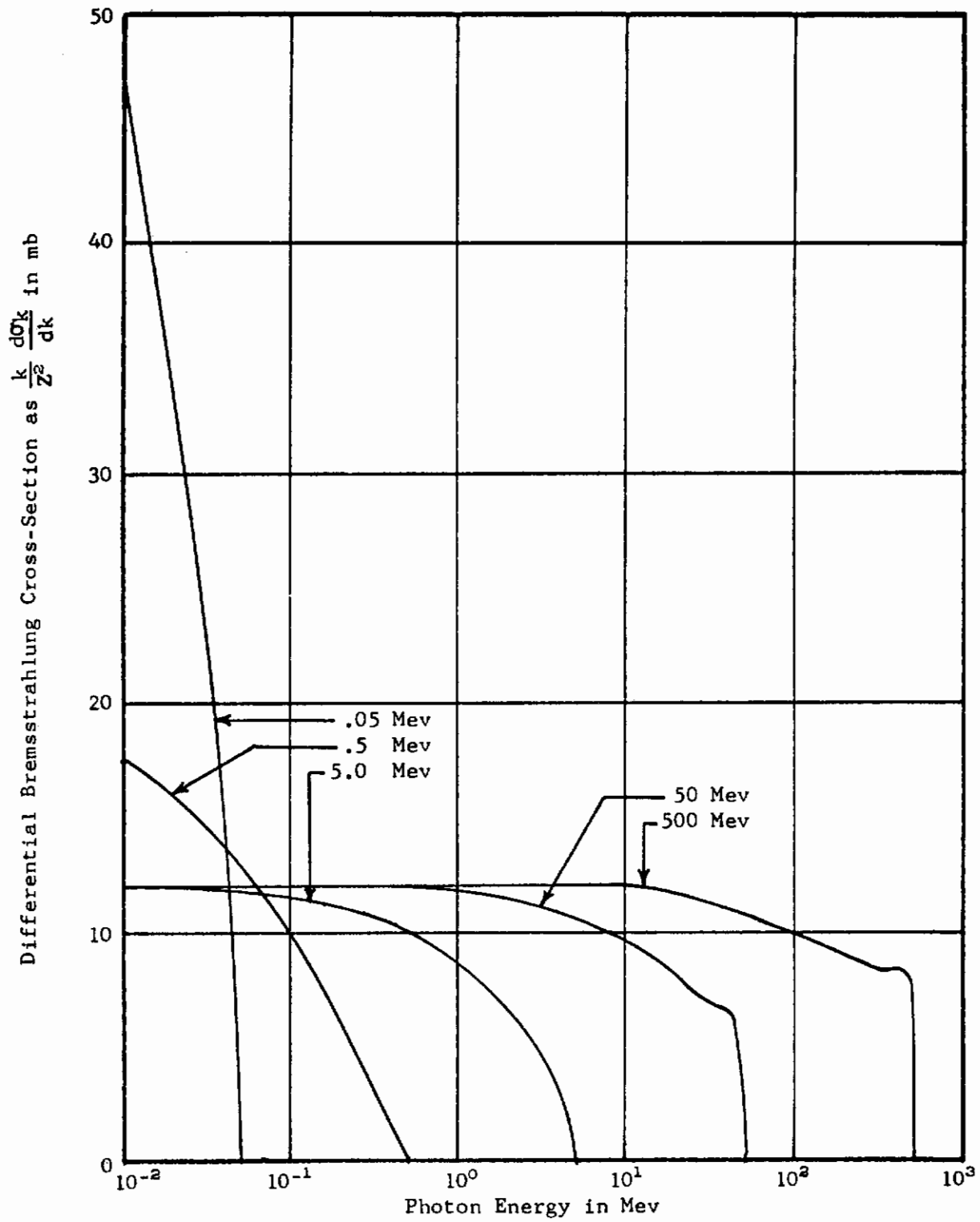


Figure 24. Bremsstrahlung Cross-Sections-Differential in Photon Energy but Integrated with Respect to Angular Distribution

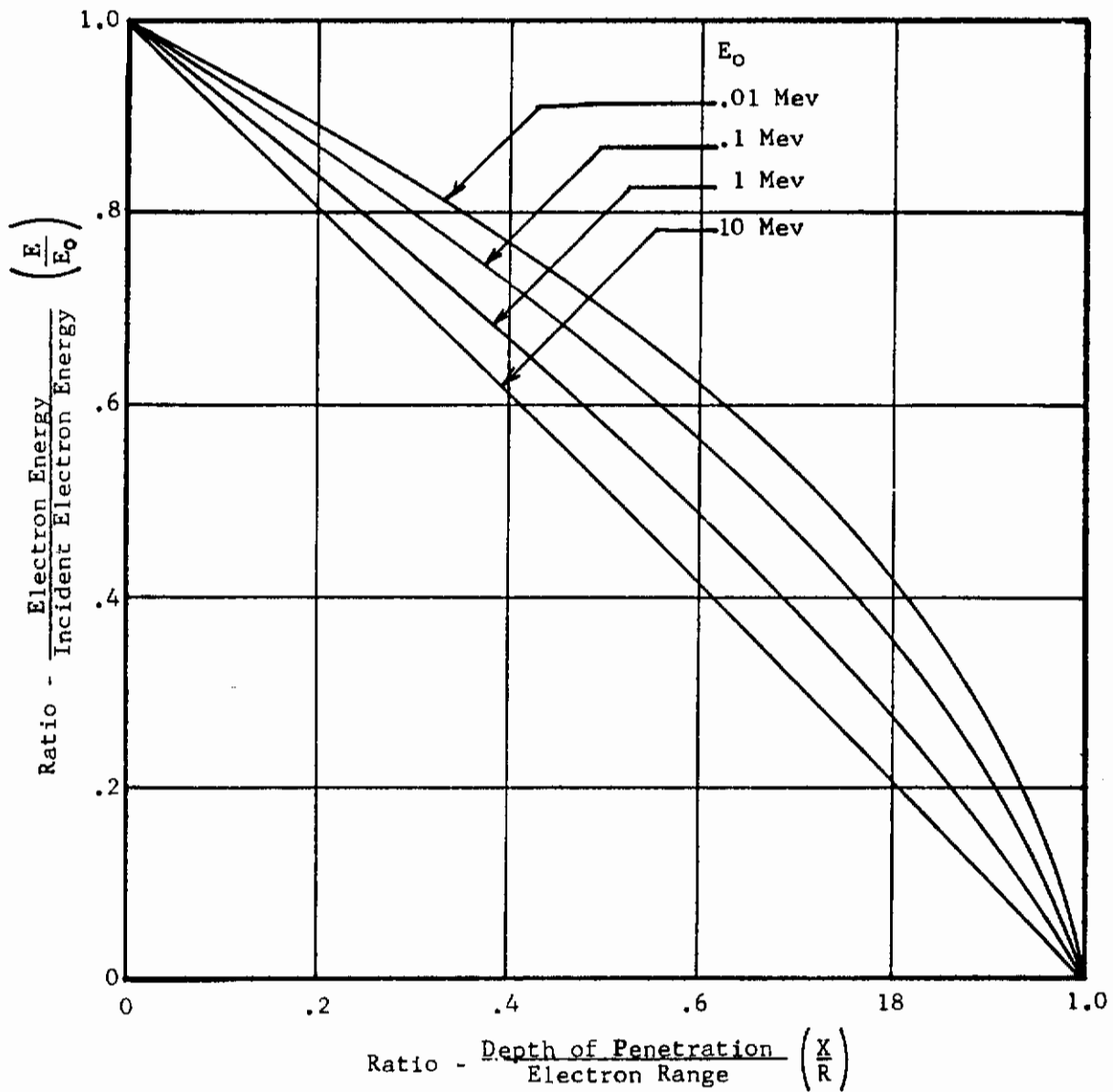


Figure 25. Electron Energy as Related to Depth of Penetration of Aluminum

TABLE 7
SOURCE DISTRIBUTION OF X-RAY DOSE
DUE TO ARTIFICIAL BELT ELECTRONS

Tenths of Shield - Total Shield 5.4 gm cm ⁻² Al.	Fraction of dose received From Each Tenth of Shield
1	.55
2	.26
3	.12
4	.048
5	.018
6	.0059
7	.0017
8	.00047
9	.00012
10	.000022

$$\phi'(E) = \phi(E) TF(E_0, X) \quad (34)$$

where $\phi'(E)$ = electron flux (electrons cm⁻²sec⁻¹ster⁻¹Mev⁻¹) at energy E (Mev) reaching a depth X(gm cm⁻²)

$\phi(E)$ = electron flux (electrons cm⁻²sec⁻¹ster⁻¹Mev⁻¹) at energy E (Mev) reaching a depth X(gm cm⁻²) with Eq 33

TF(E₀, X) = transmission factor which is a function of initial electron energy E₀ (Mev) and depth X(gm cm⁻²).

Contrails

Secondly, the X rays produced within the shield are not attenuated simply by the remaining thickness but by an increased thickness, $C(k)X$. This then tends to more closely represent the true case for an isotropic electron source. Even for a beam, scattering disperses the electrons, although X rays are produced preferentially in the direction of the electrons (ref. 40), after electron penetration, this direction is no longer necessarily that of the original electrons. The distance for X-ray attenuation is evaluated by solving for $C(k)$ utilizing equation 35.

$$e^{-\frac{C(k)X}{\lambda(k)}} = \frac{\int_0^{\pi/2} e^{-\frac{X}{\lambda(k) \cos \theta}} \sin \theta d\theta}{\int_0^{\pi/2} \sin \theta d\theta} \quad (35)$$

$C(k)$ is a function of photon energy k (Mev) and $\lambda(k)$ is the mean free path (gm cm^{-2}) for photons of energy k (Mev) in the material under evaluation.

The formulation of the X-ray source term will now be presented. Given the electron energy at any depth, X (gm cm^{-2}), the bremsstrahlung cross section $\frac{d\sigma_k}{dk}$ is calculated for various photon energies. Thus,

$$\frac{\rho N_0 Z}{A} \frac{d\sigma_k}{dk} (E, X, k) \Delta k \quad (36)$$

yields the number of photons, in energy decrement Δk (Mev) about energy k (Mev), produced per gram of material at position X (gm cm^{-2}) by electrons of energy E (Mev). Equation 36 is integrated with respect to electron energy and then with respect to X (thickness in gm cm^{-2}) in order to obtain the photon spectrum generated within the thickness of the attenuating material. In performing the numerical summation for the integration with respect to thickness, the following assumptions were made:

- The energy of electrons is constant throughout the thickness decrement, ΔX (gm cm^{-2}) upon which they impinge and is then reduced before entering the next ΔX .
- For the attenuation of the photons within the shield, the photons are all generated at the incoming face of ΔX and attenuated by $\exp \frac{C(E)\Delta X}{\lambda(E)}$ for each ΔX through which they pass.

The X rays are then attenuated by tissue, after which, equation 37 is utilized to calculate the dose rate from bremsstrahlung.

$$\text{Bremsstrahlung Dose Rate} = \sum_{i=1}^n D_c(k_i) \phi(k_i) \Delta k_i \text{ roentgens hr}^{-1} \quad (37)$$

Contrails

where $D_c(k)$ = dose conversion factor (roentgens hr⁻¹/photon cm⁻²sec⁻¹)
 $\phi(k)$ = differential photon flux (photons cm⁻²sec⁻¹ster⁻¹Mev⁻¹)
 Δk = photon energy decrement (Mev)

Figure 26 shows a plot of dose conversion factor for the range of photon energies utilized in this study (ref 41).

The application of the dose rate obtained, utilizing the above mathematical formulation is discussed in Section 5.

4.3 PROTON INTERACTIONS

Protons penetrate matter in a manner generally analogous to electrons. The ionization energy loss per unit of path length for protons and electrons at the same velocity differ by less than 10%. However, due to the mass difference, the proton energy is 1837 times greater than that of electrons at the same velocity. This gives rise to major differences in the secondary processes involved. While protons in the energy range of 10 - 300 Mev lose energy principally by electron collision (ionization), they also interact with the nuclei of the atoms of the material. In contrast, nuclear forces are unimportant for the case of incident electrons. While electrons produce bremsstrahlung through their interaction with the electric fields of nuclei, protons produce only about one-millionth the bremsstrahlung produced by an electron at the same velocity (ref 36). In the following text, ionization and nuclear interactions will be discussed.

4.3.1 Ionization

Two different expressions for the energy loss through ionization are presented. Hans Bichsel (ref 42) has derived and programmed one of these for the IBM 7090 and it is used as the basis for the penetration of protons through matter. Secondly, the energy loss expression by Sternheimer (ref 43) has been utilized in the dose calculations in the form as presented in reference 44.

The stopping power formula as expressed by Bichsel is

$$-\frac{1}{\rho} \frac{dE}{dX} = S(E) = k(\beta) \frac{Z^2}{A} \left[Z \left(f(\beta) - \ln I \right) - \left(B1 \cdot C_k + B2 \cdot C_1 + B3 \cdot C_m + B4 \cdot C_n + B5 (C_o + C_p) \right) \right] \quad (38)$$

where

$$k(\beta) = \frac{4\pi e^4 N_o}{mc^2 \beta^2} = \frac{4mc^2 r_o^2 N_o}{\beta^2} \quad \text{and} \quad f(\beta) = \left(\ln \frac{2mc^2 \beta^2}{1-\beta^2} \right) - \beta^2$$

ρ = density of stopping material (gm cm⁻³)
 z = charge number of the incident particle (1 for protons)
 Z = atomic number of the stopping material
 A = atomic weight of the stopping material (gm)
 β = v/c , velocity of the incident particle relative to the velocity of light ($c=2.9979$ cm sec⁻¹)

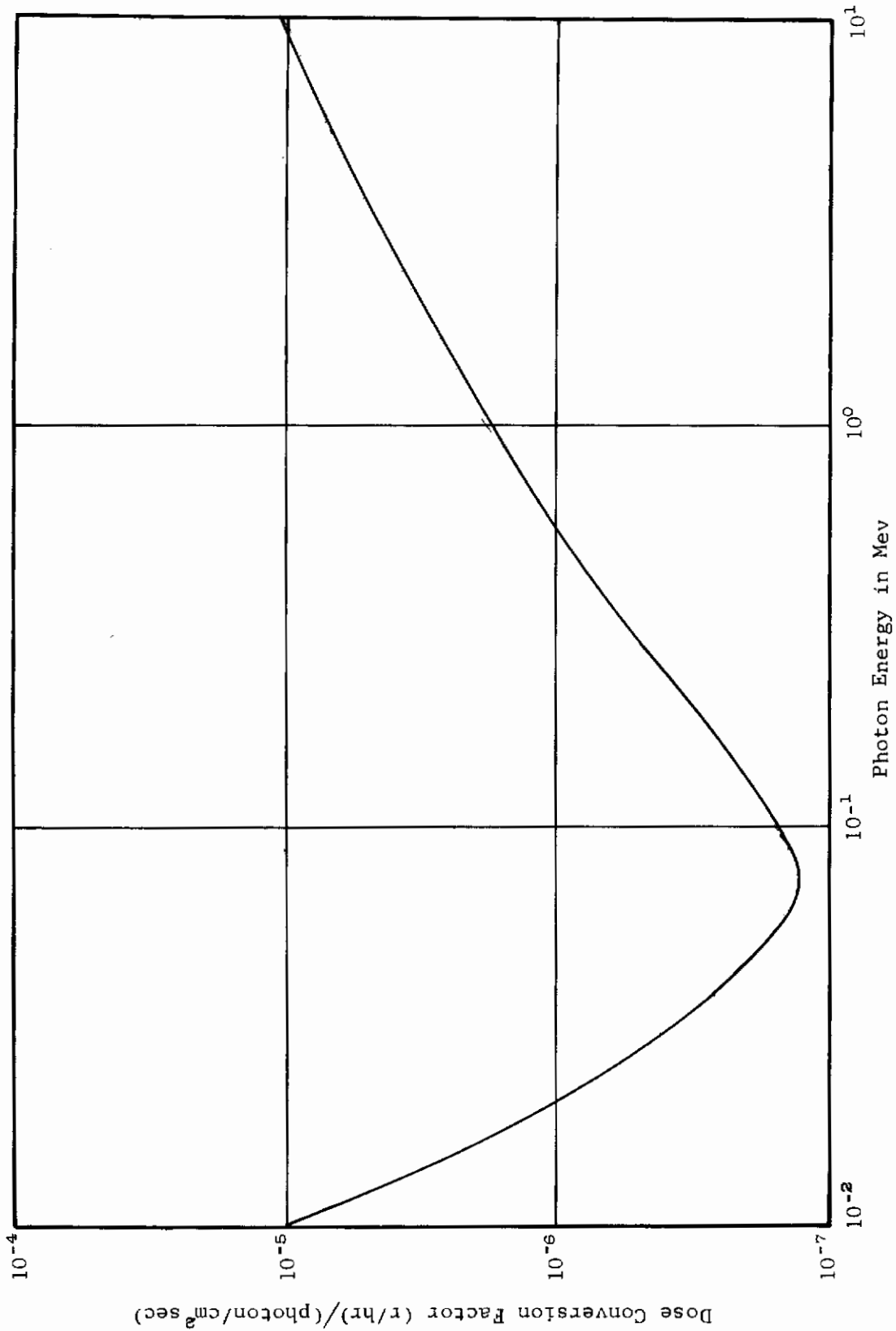


FIGURE 26 X-RAY FLUX-TO-DOSE CONVERSION FACTOR

- $C_{k,l,m,n,o,p}$ = shell corrections for various electron shells
 l = average excitation potential per electron for the stopping atoms (ev)
 $r_0^2 = 7.9403 \times 10^{-26} \text{cm}^2$
 e = electron charge ($4.803 \times 10^{-10} \text{esu}$)
 N_0 = Avogadro's number (6.02486×10^{23})
 m = rest mass of electron ($9.108 \times 10^{-28} \text{gm}$)
 $mc^2 = .510976 \text{Mev}$
 B_i = a free parameter, $B_1=B_2=1.0$ and B_3 through B_5 vary with material

The proton range is obtained from $S(E)$ as

$$E(E) = R(\epsilon) + \int_{\epsilon}^E \frac{dE}{S(E)} \quad (39)$$

where ϵ is approximately 1 Mev.

Figure 27 illustrates $R(E)$ in gm cm^{-2} for aluminum obtained using equations 38 and 39.

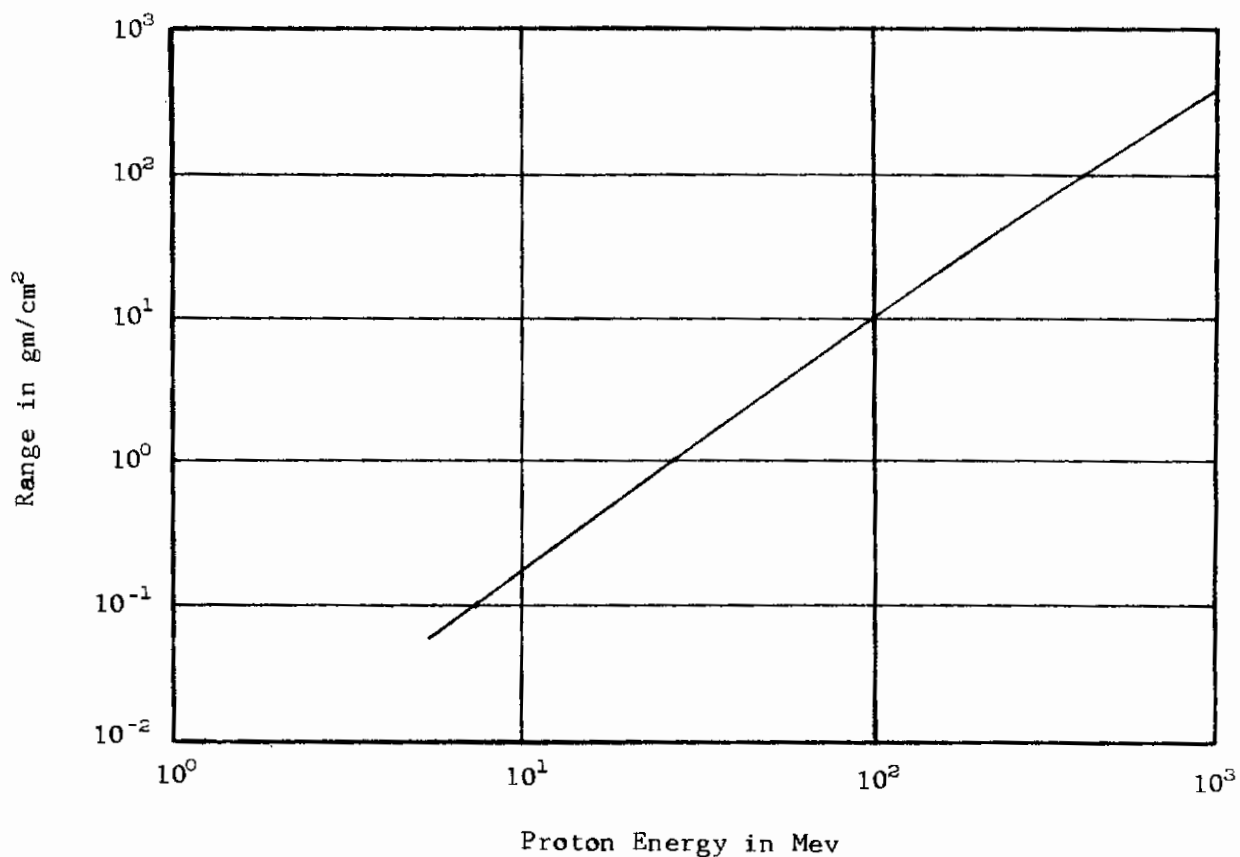


Figure 27. Range of Protons in Aluminum

Contrails

Equation 40 due to Sternheimer has been utilized in this study to calculate the proton dose in Rads.

$$-\frac{1}{\rho} \frac{dE}{dx} = S(E) = \frac{A}{\beta^2} \left[B + .69 + 2 \ln \left(\frac{P}{\mu c} \right) + \ln W_{\max} - 2\beta^2 - \delta - U \right] \quad (40)$$

where

$$A = \frac{2\pi n e^4}{m c^2 \rho},$$

$$B = \ln \left(\frac{m c^2}{I^2} \right), \quad \text{and}$$

$$W_{\max} = \frac{E_T^2 - \mu^2 c^4}{\mu c^2 \left[(\mu/2m) + (m/2\mu) + E_T/\mu c^2 \right]}$$

$$\delta = 4.606 X + C + a(X_1 - X)^{m'} \quad (X_0 < X < X_1)$$

$$\delta = 4.606 X + C \quad (X > X_1)$$

$$X = \log_{10} (P/\mu c)$$

$$C = -2 \ln (I/hv_p) - 1$$

$$v_p = (ne^2/\pi m)^{\frac{1}{2}}$$

$$U = 2C_K/Z + 2C_L/Z$$

$$P = \frac{\left(E_T^2 - (\mu c^2)^2 \right)^{\frac{1}{2}}}{c}$$

$$E_T = E_K + \mu c^2$$

$$C_L = \frac{6.85 \times 10^{-1}}{E_K}$$

c = velocity of light ($2.9979 \text{ cm sec}^{-1}$)

n = number of electrons/cm³ in stopping materials

v = velocity of proton

μ = mass of proton

m = mass of electron ($9.108 \times 10^{-20} \text{ gm}$)

W_{\max} = maximum energy transfer from proton to a free electron ($4E_T m/\mu$)

P = proton momentum

E_K = proton kinetic energy (ergs)

E_T = proton total energy (ergs)

ρ = density of stopping material (gm cm^{-3})

Contrails

- I = average ionization potential of stopping material (ergs)
- δ = density correction expression
- a, X, m' = are material constants
- v_p = plasma frequency
- h = Planck's constant (6.6252×10^{-27} erg sec)
- U = shell correction expression
- C_K, C_L = shell correction factors
- X_0 = the value of X which corresponds to the momentum below which $\delta=0$
- X_1 = the momentum above which the relation between δ and X can be assumed to be linear

4.3.2 Nuclear Interactions

Protons in the energy range 50 - 1000 Mev can interact with the nuclei of the stopping material. The higher the energy of a proton, the more important is the role of nuclear collisions before a proton reaches the end of its range, and the 1000 Mev upper limit is merely the highest energy considered for this study. Inelastic nuclear collisions result in a variety of secondary particles with complicated spectra and angular distributions.

Nuclear interactions of high-energy protons with nuclei are described with various so-called "models." The nuclear reaction is considered to consist of two phases: (1) the cascade stage characterized by nucleon-nucleon collisions within the nucleus initiated by the incoming proton and (2) the evaporation process by which particles escape from the residual nucleus, which is in an excited state, remaining at the end of the cascade. The cascade phase is usually treated by the Monte Carlo method (ref 45), while evaporation is handled as decay of the compound nucleus (ref 46). Nucleon-Nucleon cross sections are illustrated in figure 28, while figure 29 presents the probability of nuclear interaction for aluminum as related to the geometrical cross section over the energy range (50 - 1000 Mev). The theoretical prediction of particle yield from the compound nucleus is lower than that obtained experimentally (ref 47).

4.4 PROTON SHIELDING CALCULATIONS

The mathematical formulation of the penetration of protons into matter is analogous to that utilized for electrons. Ionization is the process which mainly controls the proton energy at a depth of penetration, X in gm cm⁻², and is expressed functionally as:

$$E = E_0 \left(1 - \frac{X}{R(E_0)} \right)^n \quad (41)$$

where

- E = emerging proton energy (Mev)
- E_0 = incident proton energy (Mev)
- X = depth of penetration
- $n = R(E_0) = \text{range (gm cm}^{-2}\text{) of proton having energy } E_0$

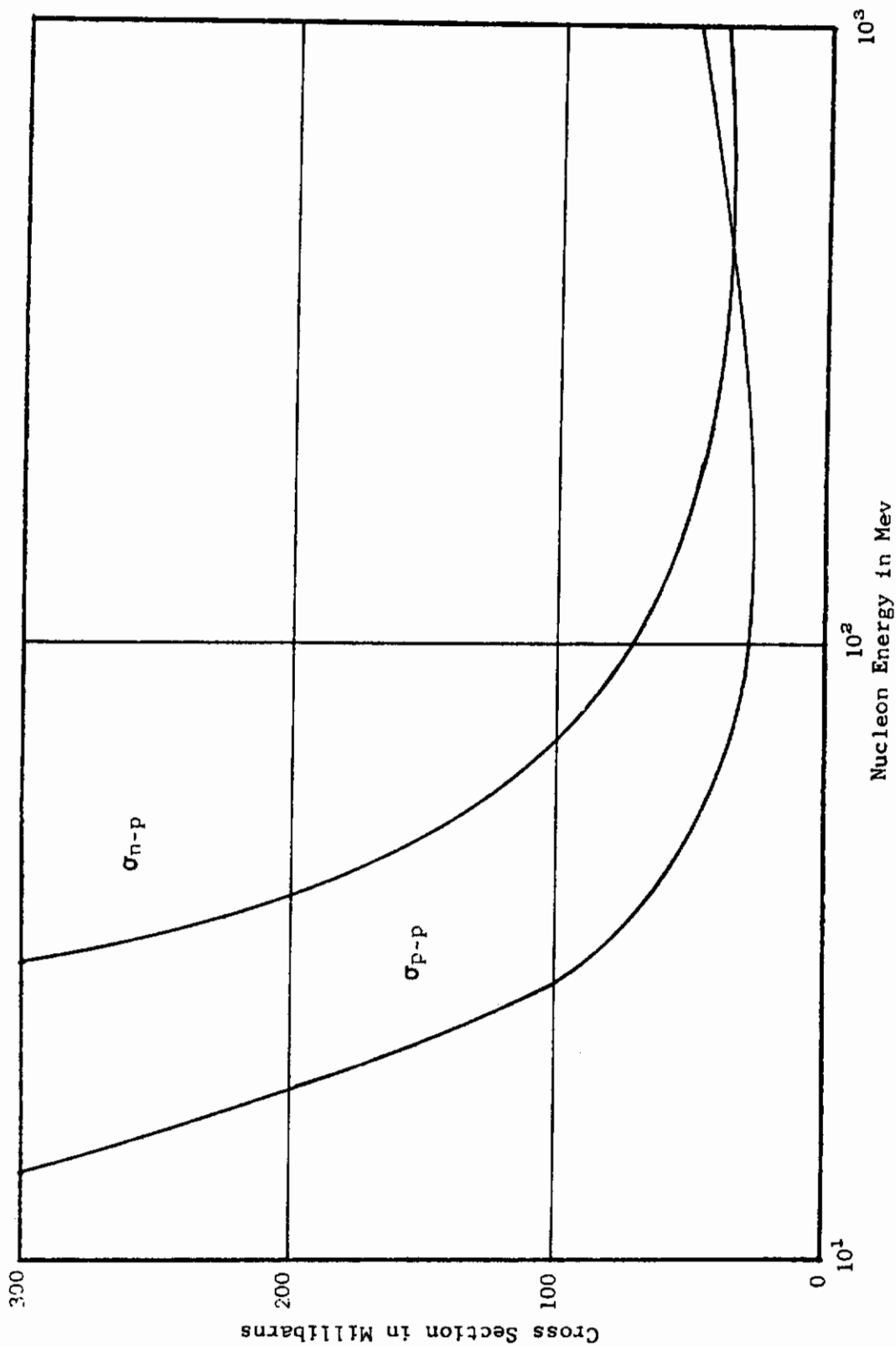


Figure 28. Nucleon-Nucleon Cross Sections

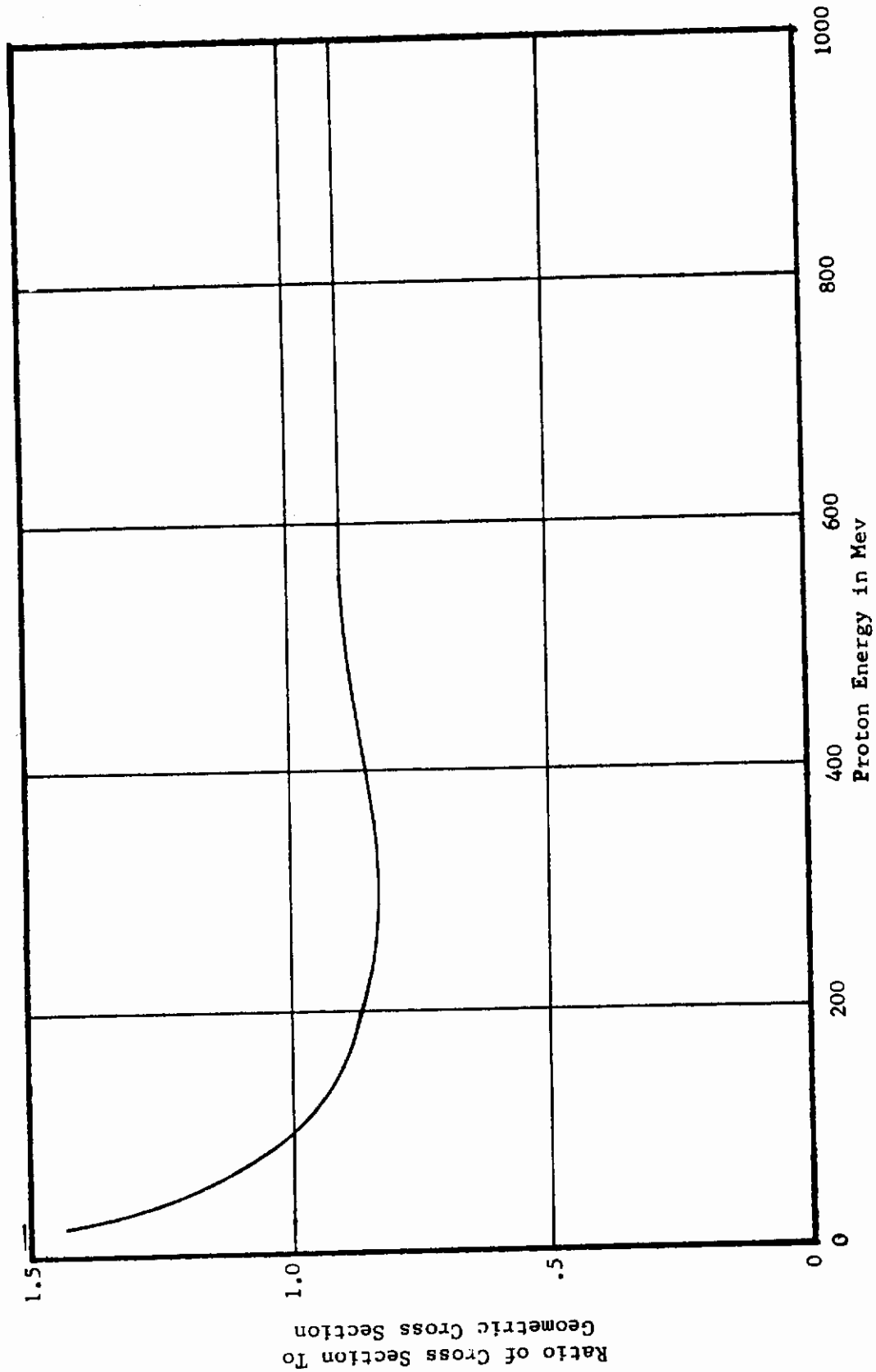


Figure 29. Proton Nonelastic Cross Section for Aluminum

Contrails

This expression is valid up to about 200 Mev. For higher energies the expression

$$E = E_0 + S(E)X \quad (42)$$

is used.

The initial proton energy is degraded according to equation 41 or equation 42 depending upon the proton energy. Along with this energy degradation the flux of this energy group is attenuated exponentially by nuclear interactions. This is formulated as

$$\phi_p(E, X + \Delta X) = \phi_p(E', X) \frac{\Delta E'}{\Delta E} e^{-\left(\frac{\Delta X}{\lambda}\right)}. \quad (43)$$

The factors in equation 43 are defined below.

$\phi_p(E, X + \Delta X)$ = differential flux of protons having energy E at depth X + ΔX .

$\phi_p(E', X)$ = differential flux of protons having energy E' at depth X, where E' = f(E, ΔX) from equation 41 or equation 45.

$\Delta E'$ and ΔE = energy decrements for the protons entering ΔX , and exiting from ΔX respectively.

λ = mean free path for nuclear interaction and is assumed independent of proton or neutron energy. For aluminum ($\lambda \sim 100$ gm/cm²) based on geometric cross section and transparency.

The nuclear interaction attenuation, $e^{-\frac{\Delta X}{\lambda}}$, in equation 43 gives rise to secondary particle fluxes at lower energies, such that

$$\begin{aligned} \phi_{ps}(E, X + \Delta X) = & \gamma_{pp} \left[\phi_p(E'', X) \frac{\Delta E''}{\Delta E} F_p(E'') \right] \\ & + \gamma_{np} \left[\phi_n(E''', X) \frac{\Delta E'''}{\Delta E} F_n(E''') \right]. \end{aligned} \quad (44)$$

The various terms in equation 44 are defined below.

$\phi_{ps}(E, X + \Delta X)$ = differential flux of secondary protons having energy E at depth X + ΔX .

$\phi_p(E'', X)$ = differential flux of protons having energy E'' = g(E) as presented in equation 47.

Contrails

$\phi_n(E''', X)$ = differential flux of neutrons having E''' at depth X ,
where $E''' = h(E)$ as presented in equation 47.

Y_{pp} = number of protons produced per proton nuclear interaction.

$\Delta E, \Delta E'', \Delta E$ are energy decrements.

$F_p(E'')$ = fraction of protons undergoing inelastic reactions
in $\Delta X - X_{np}(E, \Delta X)$.

$X_{np}(E, \Delta X)$ = portion of ΔX from which secondary proton cannot escape
from ΔX . See reference 48 for deviation.

Y_{np} = number of protons produced per neutron nuclear interaction.

$F_n(E''')$ = fraction of neutrons undergoing inelastic reactions in
 $\Delta X - X_{np}$.

The energy relationship for the nuclear interactions are

$$E = \frac{E'' - E^*}{\text{Yield}}, \quad (45)$$

$$E = \frac{E''' - E^*}{\text{Yield}}, \quad \text{and} \quad (46)$$

$$h(E) = g(E) = (\text{Yield})E + E^*. \quad (47)$$

The following are the definitions of the terms in equations 45, 46, and 47.

E = energy of emitted secondary particle.
 E^* = excitation energy resulting from nuclear interactions.
 E'' and E''' = energy of proton or neutron interacting with nucleus.

$$\text{Yield} = \begin{cases} \frac{Y_{pp} + Y_{np}/R_{pn}}{R_{pn}} & \text{(for secondary protons)} \\ \frac{Y_{pn} + R_{pn}/Y_{nn}}{Y_{nn}} & \text{(for secondary neutrons)} \end{cases}$$

R_{pn} = energy of emitted proton/energy of emitted neutrons.

Y_{pp} = number of protons produced per proton interaction.

Y_{np} = number of protons produced per neutron interaction.

Y_{nn} = number of neutrons produced per neutron interaction.

Y_{pn} = number of neutrons produced per proton interaction,
which are from reference 47.

Contrails

The secondary radiation produced by protons include neutron, protons, gamma rays, and mesons. Estimates of the gamma ray dose (refs 49 and 50) indicate that the relative importance of gamma rays is not a significant factor until the depth of penetration is 11 to 24 gm cm⁻² (~ 10% of the dose). As for the mesons, it is shown in reference 51 that for 700 Mev protons, the dose from mesons may be 30-50 percent as dangerous as that from the neutrons. In the current study the gamma-rays and mesons are neglected, due to the complexities involved.

SECTION 5

SHIELDING CALCULATIONS

Shielding calculations in the CARS program utilize the results from separate and independent space shielding programs. These programs, one for protons and one for electrons, determine the penetration of a beam flux of particles through a semi-infinite slab of material. Due to the mathematical models used in the programs and the relationship between beam flux and isotropic flux, the results can be applied to other geometries. The shielding programs are used to generate curves of dose rate versus thickness of tissue for various thicknesses of shield material. These curves are fit with an analytical expression and used in computing the dose rate at a point.

5.1 ISOTROPIC FLUX AND BEAM FLUX RELATIONSHIPS

Both the proton shielding program and the electron penetration and bremsstrahlung production program assume that a beam flux of particles is normally incident upon a semi-infinite slab of material. The proton program uses a straight ahead particle penetration assumption in calculating radiation penetration (ref 12), while the electron program utilizes a similar, but modified version of this assumption (ref 39). The relationship between a beam flux and an isotropic flux is illustrated in figure 30. Sketch a shows a beam flux impinging normally to a semi-infinite slab of thickness t . Sketch b illustrates an isotropic flux incident upon a spherical shell of thickness t . With the above assumptions, the dose rate at point P1 is equivalent to the dose rate at the center of the spherical shell, point P2.

The dose rate at a point other than the center of a spherical shell (sketch c) is approximated by;

- (1) dividing the space about the point into incremental solid angles,
- (2) calculating a representative wall slant thickness for each solid angle,
- (3) and summing the incoming radiation over 4π steradians.

The approximation is reasonably good so long as the point is not close to a vehicle wall. In the vicinity of a vehicle wall a ray is not likely to give a representative material slant thickness. The approximation can be improved, however, by increasing the number of incremental angles.

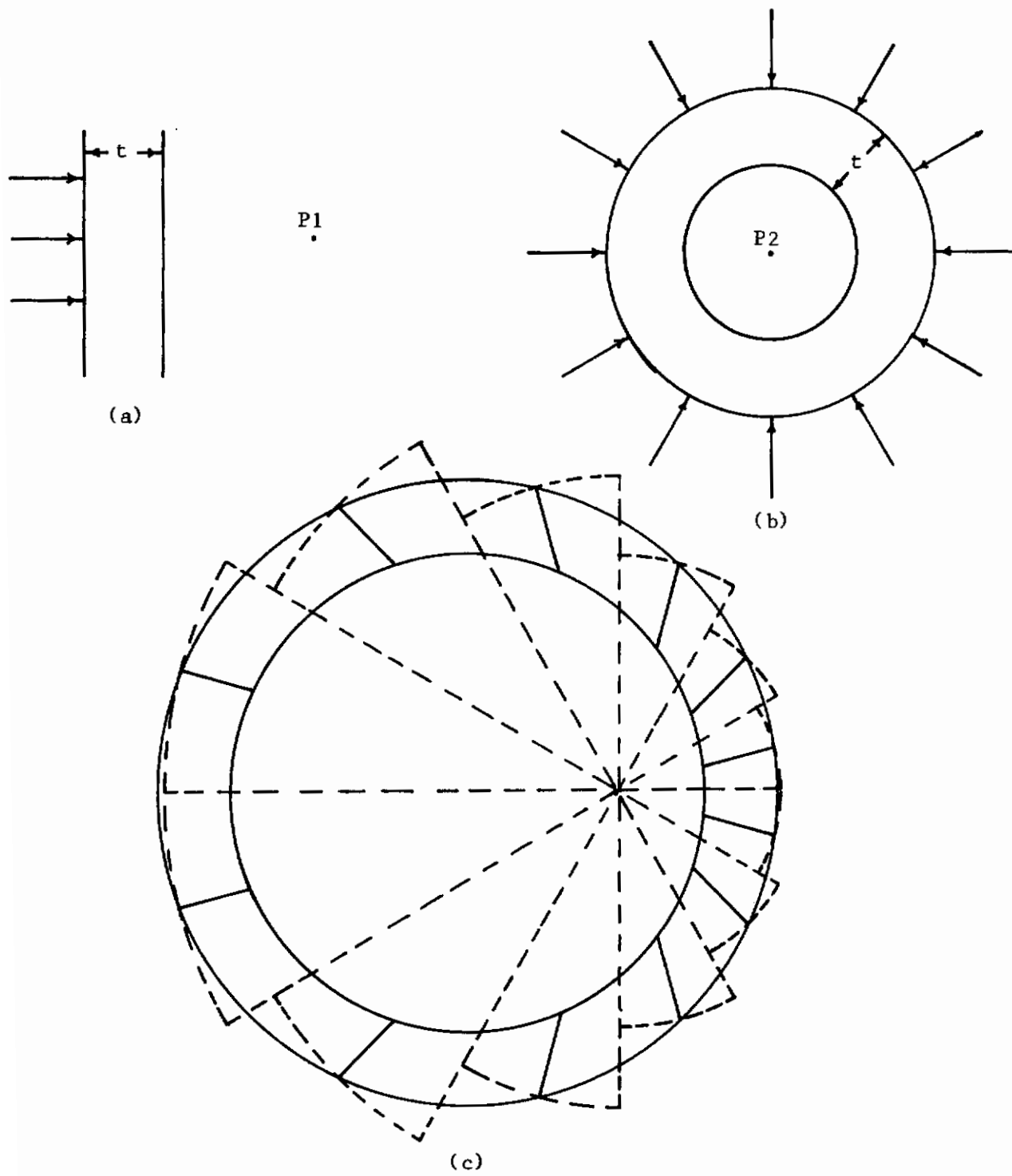


Figure 30 Flux - Geometry Relationships

This approach can be applied to any vehicle geometry; the principal problem is in determining material slant thicknesses. Expressions have been derived which will compute slant thicknesses for certain vehicle geometries and these are discussed in Section 6. For very small or irregularly shaped geometries it may be necessary to determine the material distribution about a point through direct measurement or some other means. It is a simple matter, then, to determine the dose at the point using expressions for dose versus thickness.

5.2 DOSE RATE DETERMINATION

The proton and electron shielding programs determine the particle spectra emerging from various vehicle wall thicknesses, based upon radiation impinging upon the vehicle surface. The impinging spectra are determined by the mission and radiative environment encountered. Emerging spectra from the various shield thicknesses are assumed incident upon a semi-infinite slab of tissue in order to account for the self-shielding of the astronaut's body. Shielding calculations are made with these spectra to determine the dose rate as a function of tissue thickness.

Having generated curves of dose rate versus tissue thickness for various shield thicknesses, the next step is to fit the results with an orthogonal polynomial expression of the form

$$\ln \text{Dose Rate} = [A_1 + A_2 t^1 + A_3 t^2 + \dots A_n t^{n-1}] \quad (46)$$

where t = tissue thickness

A_n = set of coefficients which is a function of the wall thickness

Several sets of coefficients for equation 46 have been determined for the Van Allen zone proton and electron spectra and the envelope solar flare proton spectrum. The coefficients were determined for the above spectra after penetrating various thicknesses of aluminum. Six terms were used in the calculations and the results are given in tables 8, 9, and 10. Figures 31, 32, and 33 illustrate the curves which are represented by the different sets of coefficients.

Thus, the dose rate is given in terms of tissue thickness for different vehicle wall thicknesses. The material slant thicknesses must be determined for each incremental solid angle (see Sections 6 and 7). Ideally, a calculated wall slant thickness will fall in the range of wall thicknesses chosen for curve fitting. The dose rates per steradian are computed, Eq 46, for the adjacent curves using the appropriate coefficients and tissue thickness. The dose rate per steradian for the calculated wall thickness is obtained by interpolating between the results.

TABLE 8
ORTHOGONAL POLYNOMIAL COEFFICIENTS FOR VAN ALLEN PROTONS
FOR VARIOUS THICKNESSES OF ALUMINUM

N	Al Thickness g/cm ²	A(N,1)	A(N,2)	A(N,3)	A(N,4)	A(N,5)	A(N,6)
1	3.0	-0.77537x10 ¹	-1.26944x10 ⁻¹	+3.28078x10 ⁻³	-4.92462x10 ⁻⁵	+3.54788x10 ⁻⁷	-9.71000x10 ⁻¹⁰
2	5.0	-0.79985x10 ¹	-1.07907x10 ⁻¹	+2.63945x10 ⁻³	-3.93649x10 ⁻⁵	+2.84616x10 ⁻⁷	-7.83595x10 ⁻¹⁰
3	7.5	-0.82309x10 ¹	-0.94998x10 ⁻¹	+2.22540x10 ⁻³	-3.29698x10 ⁻⁵	+2.39033x10 ⁻⁷	-6.62063x10 ⁻¹⁰
4	10.0	-0.84561x10 ¹	-0.82255x10 ⁻¹	+1.90224x10 ⁻³	-2.87687x10 ⁻⁵	+2.11131x10 ⁻⁷	-5.87674x10 ⁻¹⁰
5	12.5	-0.85453x10 ¹	-0.77621x10 ⁻¹	+1.73046x10 ⁻³	-2.57371x10 ⁻⁵	+1.86741x10 ⁻⁷	-5.15556x10 ⁻¹⁰
6	15.0	-0.86865x10 ¹	-0.69078x10 ⁻¹	+1.43559x10 ⁻³	-2.07702x10 ⁻⁵	+1.48205x10 ⁻⁷	-4.04536x10 ⁻¹⁰
7	17.5	-0.88534x10 ¹	-0.61138x10 ⁻¹	+1.19336x10 ⁻³	-1.70385x10 ⁻⁵	+1.21369x10 ⁻⁷	-3.32586x10 ⁻¹⁰
8	20.0	-0.90702x10 ¹	-0.48813x10 ⁻¹	+0.78841x10 ⁻³	-1.05579x10 ⁻⁵	+0.73264x10 ⁻⁷	-1.98954x10 ⁻¹⁰
9	25.0	-0.93125x10 ¹	-0.35567x10 ⁻¹	+0.37735x10 ⁻³	-0.39198x10 ⁻⁵	+0.22070x10 ⁻⁷	-0.50493x10 ⁻¹⁰
10	30.0	-0.95070x10 ¹	-0.28949x10 ⁻¹	+0.24334x10 ⁻³	-0.26444x10 ⁻⁵	+0.16651x10 ⁻⁷	-0.42634x10 ⁻¹⁰

TABLE 9
ORTHOGONAL POLYNOMIAL COEFFICIENTS FOR ARTIFICIAL BELT ELECTRONS
PENETRATING VARIOUS THICKNESSES OF ALUMINUM

N	Al Thickness g/cm ²	A(N, 1)	A(N, 2)	A(N, 3)	A(N, 4)	A(N, 5)
1	2.0	-0.12568x10 ²	-0.53293x10 ⁰	+0.13784x10 ⁻¹	-0.14618x10 ⁻³	+0.52605x10 ⁻⁶
2	4.0	-0.15795x10 ²	-0.25635x10 ⁰	+0.61682x10 ⁻²	-0.65383x10 ⁻⁴	+0.23528x10 ⁻⁶
3	6.0	-0.18477x10 ²	-0.32719x10 ⁻¹	+0.12651x10 ⁻⁴	-0.10104x10 ⁻⁶	+0.42459x10 ⁻⁹
4	8.0	-0.18734x10 ²	-0.32092x10 ⁻¹	-0.39688x10 ⁻⁵	+0.12792x10 ⁻⁶	-0.58836x10 ⁻⁹
5	10.0	-0.18985x10 ²	-0.32062x10 ⁻¹	+0.67458x10 ⁻⁵	-0.38101x10 ⁻⁷	+0.14226x10 ⁻⁹
6	14.0	-0.19480x10 ²	-0.31565x10 ⁻¹	-0.10834x10 ⁻⁶	+0.46840x10 ⁻⁷	-0.16387x10 ⁻⁹
7	18.0	-0.19977x10 ²	-0.31279x10 ⁻¹	+0.42749x10 ⁻⁶	+0.49087x10 ⁻⁷	-0.20490x10 ⁻⁹
8	24.0	-0.20763x10 ²	-0.30653x10 ⁻¹	-0.42575x10 ⁻⁵	+0.10674x10 ⁻⁶	-0.41596x10 ⁻⁹
9	30.0	-0.21724x10 ²	-0.29996x10 ⁻¹	-0.36145x10 ⁻⁵	+0.94757x10 ⁻⁷	-0.36957x10 ⁻⁹

TABLE 10
ORTHOGONAL POLYNOMIAL COEFFICIENTS FOR ENVELOPE FLARE PROTONS
PENETRATING VARIOUS THICKNESSES OF ALUMINUM

N	A ₁ Thickness g/cm ²	A(N, 1)	A(N, 2)	A(N, 3)	A(N, 4)	A(N, 5)	A(n, 6)
1	2.0	-0.13294x10 ²	-4.09318x10 ⁻¹	+1.20376x10 ⁻²	-1.86075x10 ⁻⁴	+13.8084x10 ⁻⁷	-3.87240x10 ⁻⁹
2	4.0	-0.14167x10 ²	-3.28820x10 ⁻¹	+0.89642x10 ⁻²	-1.32328x10 ⁻⁴	+9.51022x10 ⁻⁷	-2.60047x10 ⁻⁹
3	6.0	-0.14877x10 ²	-2.73814x10 ⁻¹	+0.70194x10 ⁻²	-1.00773x10 ⁻⁴	+7.17211x10 ⁻⁷	-1.95852x10 ⁻⁹
4	8.0	-0.15460x10 ²	-2.23223x10 ⁻¹	+0.51803x10 ⁻²	-0.70124x10 ⁻⁴	+4.82847x10 ⁻⁷	-1.29097x10 ⁻⁹
5	10.0	-0.15768x10 ²	-2.07544x10 ⁻¹	+0.48135x10 ⁻²	-0.65748x10 ⁻⁴	+4.56946x10 ⁻⁷	-1.23137x10 ⁻⁹
6	14.0	-0.16428x10 ²	-1.62959x10 ⁻¹	+0.33408x10 ⁻²	-0.41692x10 ⁻⁴	+2.73469x10 ⁻⁷	-0.71131x10 ⁻⁹
7	18.0	-0.16892x10 ²	-1.40496x10 ⁻¹	+0.27518x10 ⁻²	-0.33554x10 ⁻⁴	+2.17789x10 ⁻⁷	-0.56339x10 ⁻⁹
8	24.0	-0.17570x10 ²	-1.08545x10 ⁻¹	+0.19241x10 ⁻²	-0.21956x10 ⁻⁴	+1.37858x10 ⁻⁷	-0.35275x10 ⁻⁹
9	30	-0.18086x10 ²	-0.80192x10 ⁻¹	+0.11456x10 ⁻²	-0.10574x10 ⁻⁴	+0.55022x10 ⁻⁷	-0.12067x10 ⁻⁹

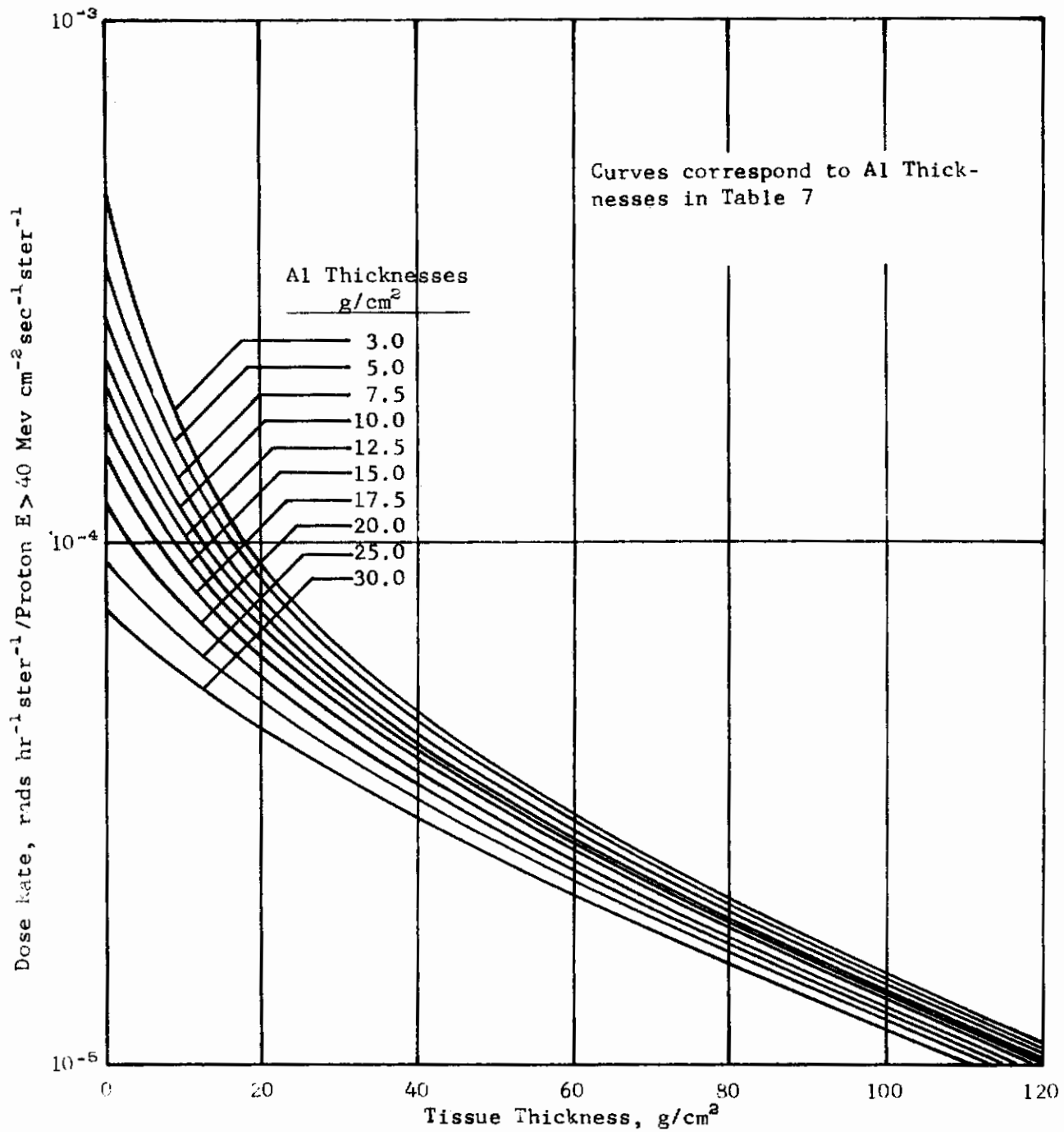


Figure 31. Dose Rate versus Depth in Tissue Due to Van Allen Protons After Passing Through Various Thicknesses of Aluminum

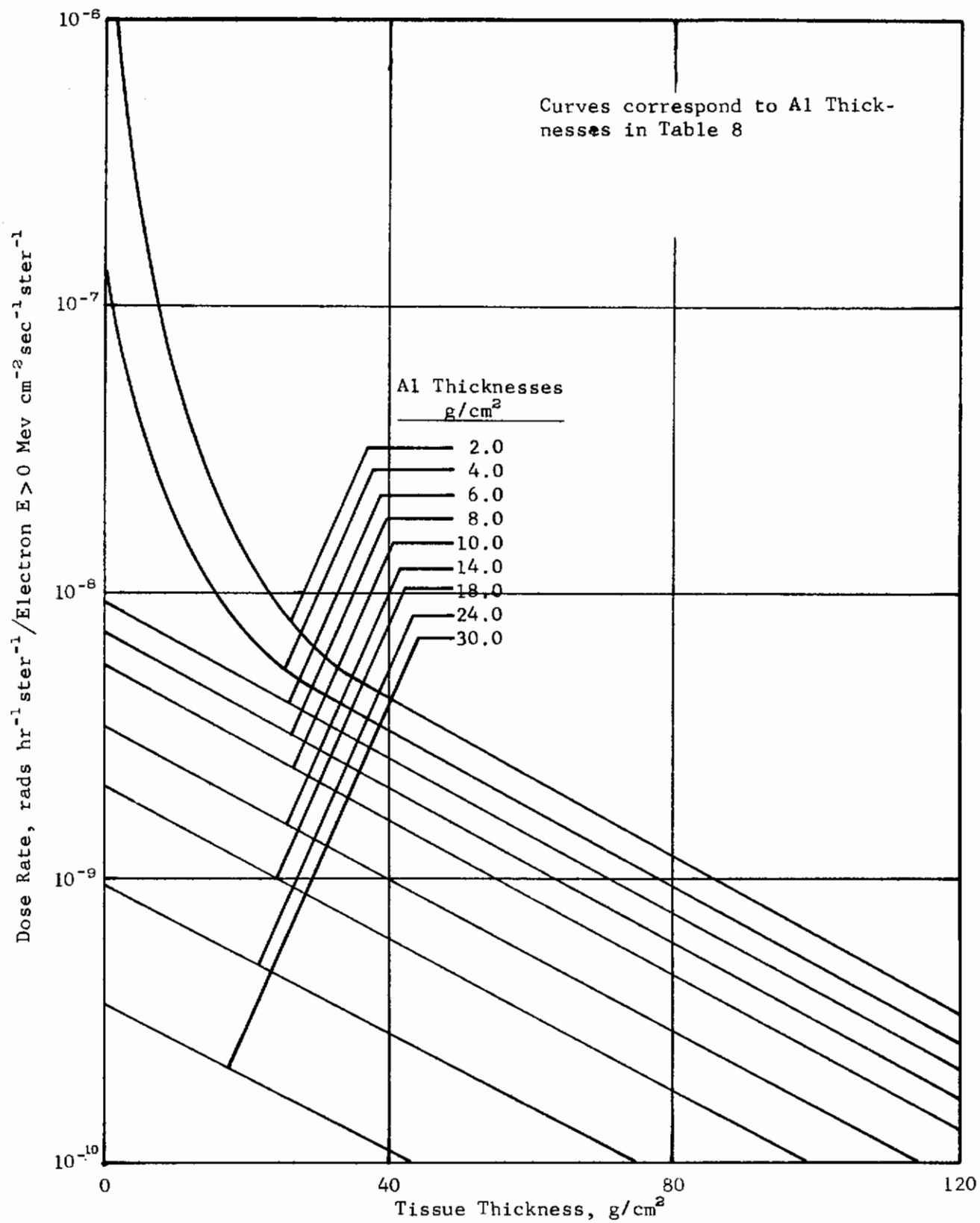


Figure 32 Dose Rate versus Depth in Tissue Due to Artificial Belt Electrons Passing Through Various Thicknesses of Aluminum

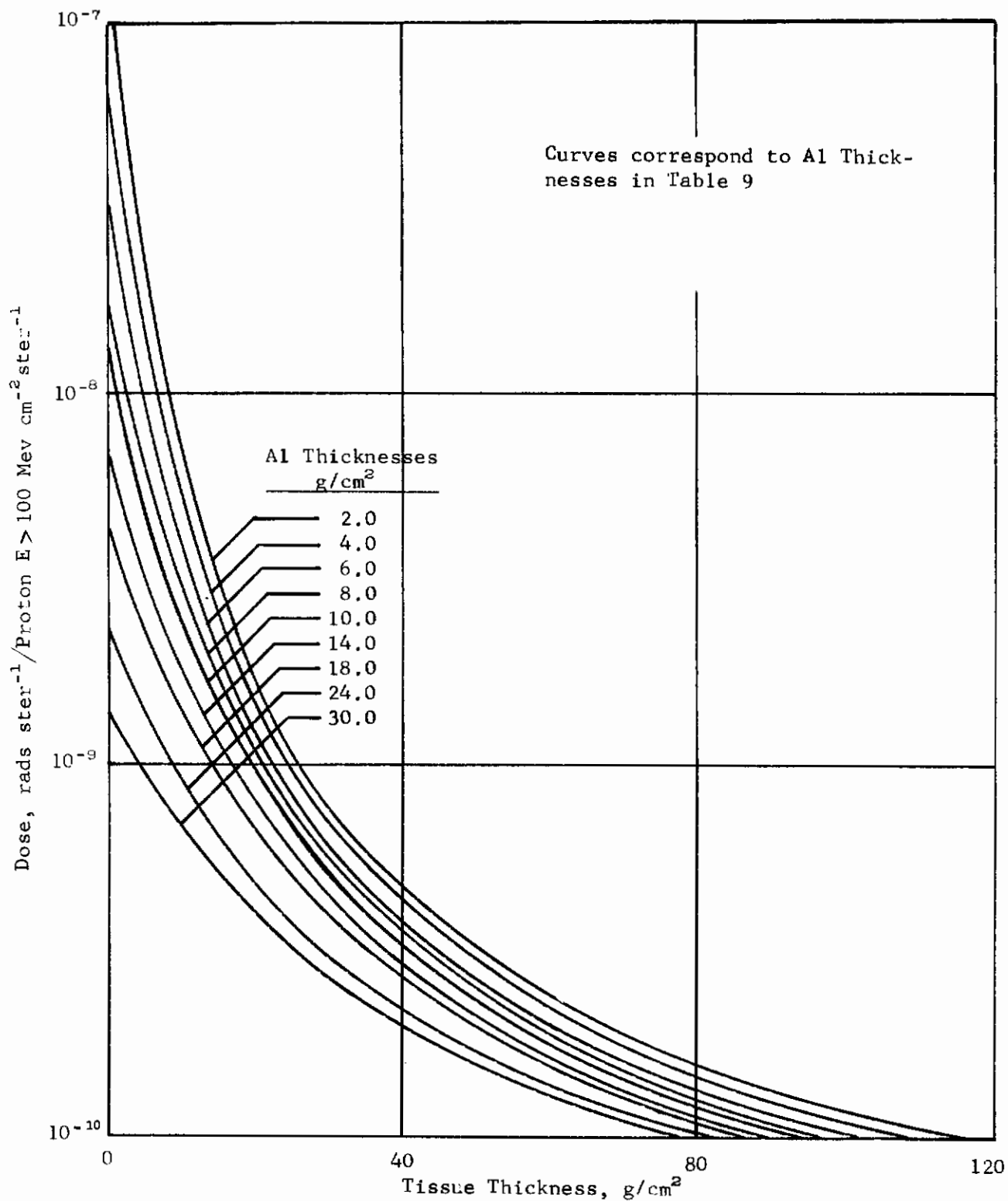


Figure 33 Dose Rate versus Depth in Tissue Due to Solar Flare Protons After Passing Through Various Thicknesses of Aluminum

Contrails

The total dose rate at a point is found by summation over all the incremental solid angles.

$$D = \sum_{ij} D_{ij} \Delta\Omega_{ij} \quad (47)$$

where D_{ij} = dose rate per unit solid angle determined from equation 46

$\Delta\Omega_{ij}$ = incremental solid angle

The total dose rate at a point is calculated for a specified number of points. Each point is assumed to represent an area on a surface at a given depth in the model astronaut. A mean dose rate for the surface is calculated by

$$\bar{D}_t = \frac{\sum_i D_i A_i}{\sum_i A_i} \quad (48)$$

where \bar{D}_t = mean dose rate at depth t in the model astronaut

D_i = calculated dose rate at i^{th} point on surface at depth t

A_i = area of surface a depth t represented by i^{th} point.

The environmental flux spectra, which are utilized in this study, are for normalized unidirectional flux. Calculated dose rates are in units of;

- (1) rads hr⁻¹/Proton with $E > 40$ Mev cm⁻²sec⁻¹ster⁻¹ for Van Allen protons
- (2) rads hr⁻¹/Electron with $E > 0$ Mev cm⁻²sec⁻¹ster⁻¹ for Van Allen electrons
- (3) rads/Proton with $E > 100$ Mev cm⁻²ster⁻¹ for envelope solar flare.

Multiplying the results by the average unidirectional flux intensity encountered on a particular mission (as determined in the trajectory portion of CARS) gives an accurate estimate of the dose or dose rate to be encountered.

Thus, the CARS program accounts for the environment, the mission, the vehicle geometry, the particle interaction with the vehicle wall material, and the self-shielding of the crew member in assessing the biomedical radiation hazard.

SECTION 6

VEHICLE GEOMETRY

The vehicle geometry is assumed to be represented by the combination of several geometrical surfaces. Analytical expressions have been developed for spherical, conical, and toroidal surfaces. Any combination of these is possible and each can be used as many times as required to describe a space vehicle.

6.1 MATHEMATICAL DESCRIPTION OF SURFACE

Expressions for the different surfaces are

Spherical

$$(x-a)^2 + (y-b)^2 + (z-c)^2 - R^2 = 0 \quad (49)$$

Conical

$$\frac{z^2}{c^2} + \frac{y^2}{b^2} - \frac{(x-a)^2}{a^2} = 0 \quad (50)$$

Toroidal

$$[(x-a)^2 + y^2 + z^2 + b^2 - r^2]^2 - 4b^2(y^2 - z^2) = 0 \quad (51)$$

The various constants in the above are as shown in figure 34. It is a relatively simple task to utilize other surfaces, however, these three offer considerable flexibility.

Spherical coordinate angles, θ and φ , are utilized to define rays from the origin of an arbitrary coordinate system. Coordinates of the intersection points of these rays with specified vehicle surfaces are determined with the following expressions.

$$x = t \sin \varphi \cos \theta \quad (52)$$

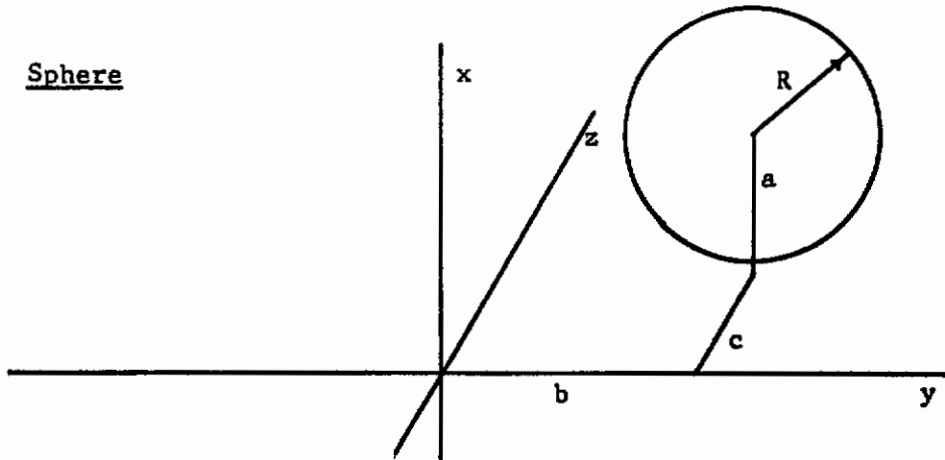
$$y = t \sin \varphi \sin \theta \quad (53)$$

$$z = t \cos \varphi \quad (54)$$

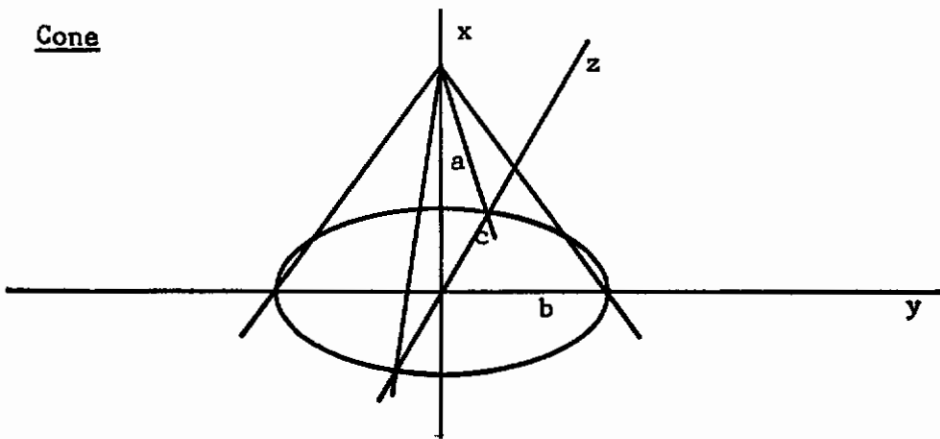
The parameter, t , is found by parametric substitution in equations 49, 50, and 51. The resulting equations are quadratics so that the solution for t is of the form

Contraails

Sphere



Cone



Torus

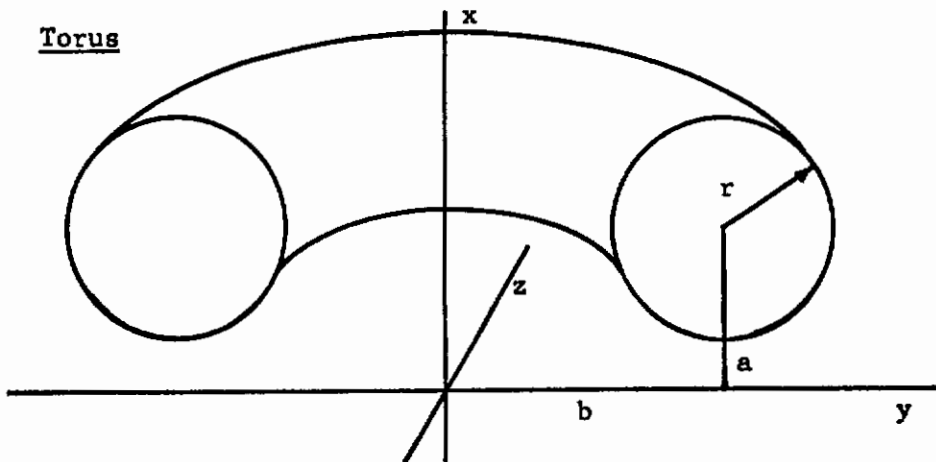


Figure 34. Surfaces Available for Describing Spacecraft Geometry

$$t = \frac{-B_1 \pm \sqrt{B_1^2 - 4A_1 C_1}}{2A_1} \quad (55)$$

where

Spherical

$$A_1 = 1.0 \quad (56)$$

$$B_1 = -2(a \sin \varphi \cos \theta + b \sin \varphi \sin \theta + c \cos \varphi) \quad (57)$$

$$C_1 = a^2 + b^2 + c^2 - R^2 \quad (58)$$

Conical

$$A_1 = a^2 b^2 \cos^2 \varphi + a^2 c^2 \sin^2 \varphi \sin^2 \theta - b^2 c^2 \sin^2 \varphi \cos^2 \theta \quad (59)$$

$$B_1 = 2ab^2 c^2 \sin \varphi \cos \theta \quad (60)$$

$$C_1 = -a^2 b^2 c^2 \quad (61)$$

Toroidal

$$A_1 = 1.0 \quad (62)$$

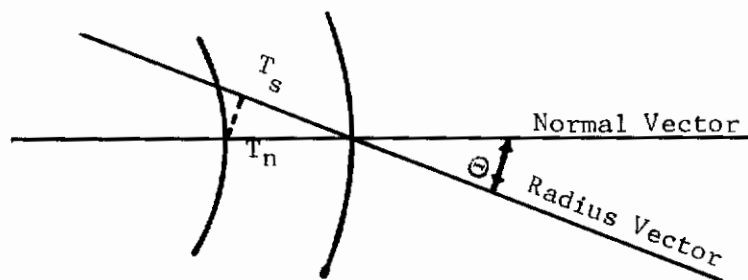
$$B_1 = -2[a \sin \varphi \cos \theta + b(\sin^2 \varphi \sin^2 \theta + \cos^2 \varphi)^{\frac{1}{2}}] \quad (63)$$

$$C_1 = a^2 + b^2 - r^2 \quad (64)$$

Once the intersection points on the vehicle surface are determined, they remain constant for a given problem. The next step is to determine the vehicle wall slant thicknesses with respect to any specified point in the vehicle.

6.2 CALCULATION OF SLANT THICKNESSES

A wall slant thickness with respect to a given point is determined using the angle between the radius vector and the normal to the vehicle surface and the normal wall thickness. The relationship between the wall slant thickness (T_s) and the normal thickness can be seen in the following sketch.



$$T_{s_{ij}} = T_{n_{ij}} / \cos \Theta$$

Figure 35. Wall Slant Thickness Relationship

The angle, Θ , is the angle between the radius vector and the normal to the vehicle surface. The formulation used in determining $\cos \Theta$ is as follows.

$$\begin{aligned} \cos \Theta &= \frac{\vec{N}}{|\vec{N}|} \cdot \frac{\vec{R}}{|\vec{R}|} & (66) \\ &= \cos \alpha_N \cos \alpha_R + \cos \beta_N \cos \beta_R + \cos \gamma_N \cos \gamma_R \end{aligned}$$

where α , β , and γ are the direction angles of the radius vector (\vec{R}) and the normal vector (\vec{N}). The direction cosines for the radius vector are obtained from

$$\cos \alpha_R = (x - XREF) / DEN \quad (67)$$

$$\cos \beta_R = (y - YREF) / DEN \quad (68)$$

$$\cos \gamma_R = (z - ZREF) / DEN \quad (69)$$

$$DEN = \sqrt{(x - XREF)^2 + (y - YREF)^2 + (z - ZREF)^2} \quad (70)$$

where x, y, z = coordinates of intersection point

$XREF, YREF, ZREF$ = coordinates of point at which the dose is to be calculated

The direction cosines for the normal vector are determined from

Spherical

$$\cos \alpha_N = (x-a)/DEN \quad (71)$$

$$\cos \beta_N = (y-b)/DEN \quad (72)$$

$$\cos \gamma_N = (z-c)/DEN \quad (73)$$

$$DEN = \sqrt{(x-a)^2 + (y-b)^2 + (z-c)^2} \quad (74)$$

Conical

$$\cos \alpha_N = (a-x)/(a^2 DEN) \quad (75)$$

$$\cos \beta_N = y/(b^2 DEN) \quad (76)$$

$$\cos \gamma_N = z/(c^2 DEN) \quad (77)$$

$$DEN = \sqrt{\left(\frac{a-x}{a^2}\right)^2 + \left(\frac{y}{b^2}\right)^2 + \left(\frac{z}{c^2}\right)^2} \quad (78)$$

Toroidal

$$\cos \alpha_N = f(x,y,z)(x-a)/DEN \quad (79)$$

$$\cos \beta_N = f(x,y,z)y-2b^2y/DEN \quad (80)$$

$$\cos \gamma_N = f(x,y,z)-2b^2z/DEN \quad (81)$$

$$f(x,y,z) = (x-a)^2 + y^2 + z^2 + b^2 - r^2 \quad (82)$$

$$DEN = \sqrt{[f(x,y,z)(x-a)]^2 + [f(x,y,z)y-2b^2y]^2 + [f(x,y,z)-2b^2z]^2} \quad (83)$$

The constants in the above equations are as illustrated in figure 34.

Vehicle wall slant thicknesses are thus calculated between each intersection point and the point at which the dose rate is to be calculated. These thicknesses determine which sets of A_N coefficients to use in the dose rate calculations (Section 5).

The surfaces described above were used to describe a vehicle representing the APOLLO Command Module (CM). It was divided into four sections; two spherical, one conical and one toroidal. (See figure 36.) The walls of the spacecraft were assumed to be laminated similar to the illustration in figure 37. Material densities and probable normal thicknesses of the various layers are included in the figure. Equivalent thicknesses of aluminum based upon proton ranges are also given. The thickness of the heat resistant material, phenolic nylon, is variable since greater thicknesses are required on the blunt end and the lower side of the vehicle

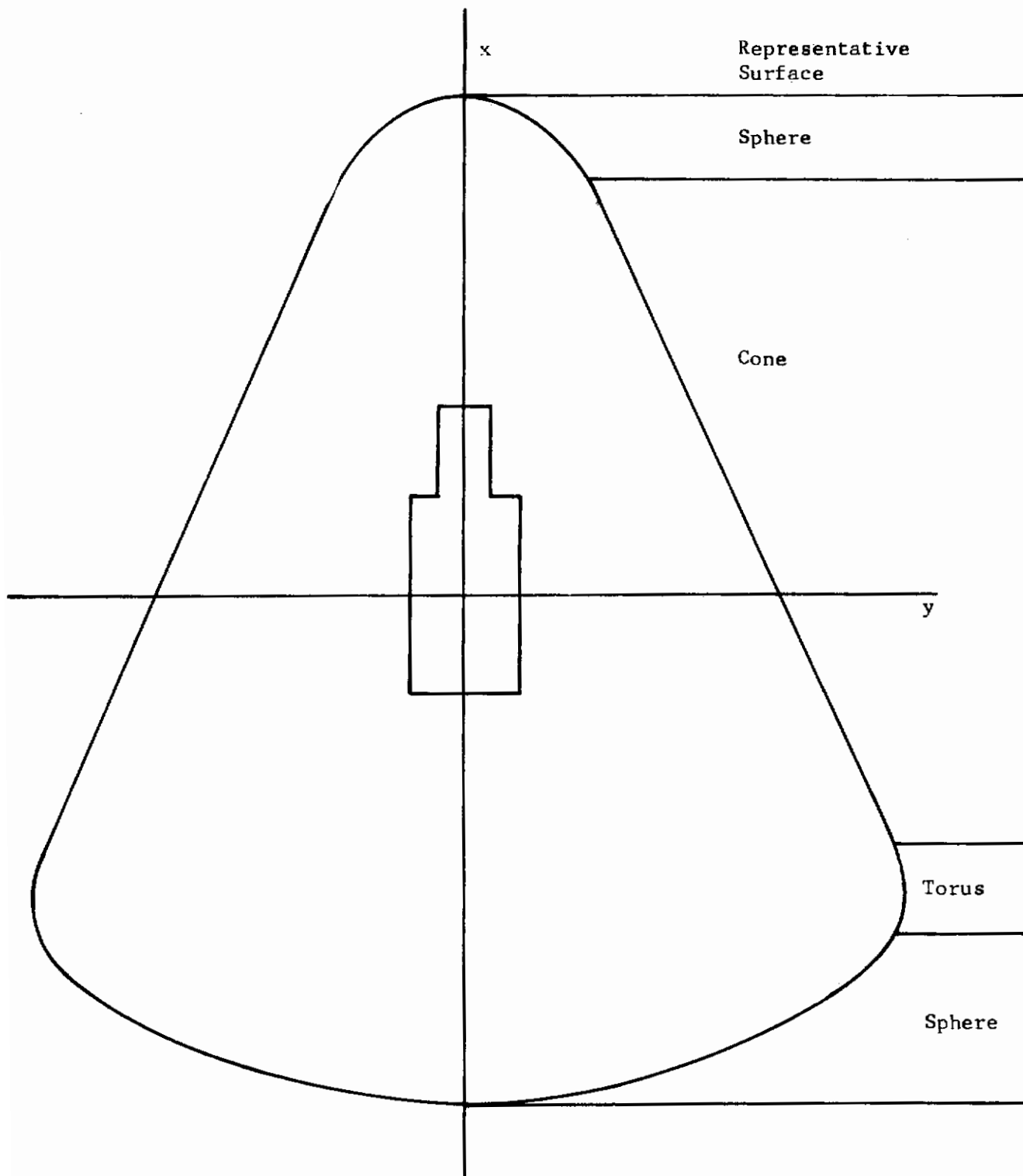
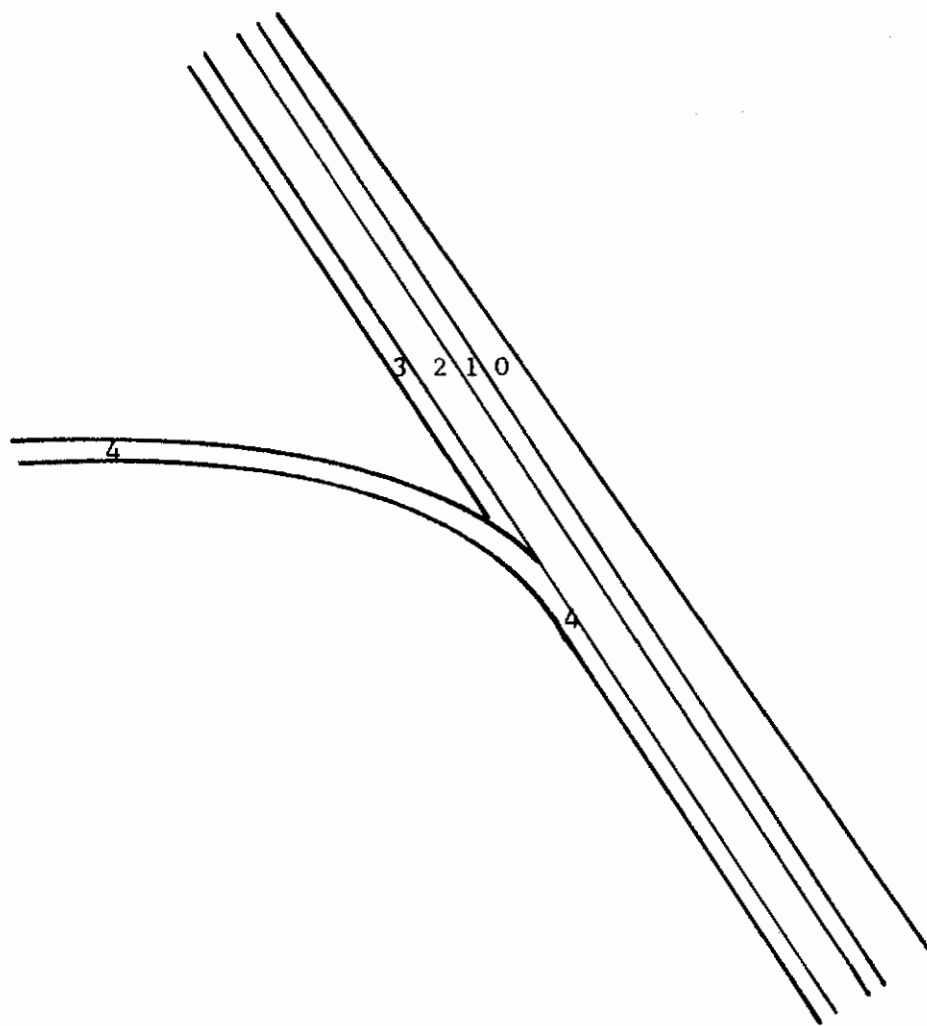


Figure 36. Cross Section of APOLLO Command Module
Showing Position and Orientation of Model Astronaut in
Sample Problem



Layer Number	Material	ρ g/cm ³	Normal Inches	Thickness g/cm ²	Equivalent Thickness Weighting Factor
0	Phenolic Nylon	1.20150	Variable		1.221
1	Stainless Steel Backup	7.83344	.1	1.990	0.8403
2	Thermoflex Insulation	0.03845	.5	.004883	1.0582
3	Stainless Steel Shell	7.83344	.1	1.990	0.8403
4	Aluminum Pressure Vessel	2.768	.1	.7031	1.000

Figure 37. Typical Wall of the APOLLO Command Module

Contrails

during reentry. It is taken to vary as $[\sin \omega/2]^4$ where ω is equivalent to the angle θ in a cylindrical coordinate system with ω measured in the yz plane. Calculations of dose rates were made with the model astronaut positioned in the APOLLO vehicle as in figure 37 and the results are presented in Section 8.

SECTION 7

MODEL ASTRONAUT

In order to predict the space radiation dose rate at a point on or within an astronaut, one must account for the self shielding of the body. A mathematical model representing an astronaut was devised for this investigation. It reflects a certain amount of the details of the human body and, yet, maintains a relatively simple geometry. Tissue slant thicknesses in the model astronaut for each incremental solid angle are determined in the Model Astronaut and Vehicle Radiation Analysis Code (MAVRAC), ref 52. These thicknesses along with the vehicle wall slant thicknesses are used to determine the dose rate at a point. In this way both vehicle shielding and self shielding of the model astronaut are taken into account.

7.1 DESCRIPTION OF MATHEMATICAL MODEL

The model astronaut utilized in this investigation reflects the flatness of the human torso and head. This factor may be important when predicting the dose rate distribution in an astronaut. The model consists of two finite right elliptical cylinders, one representing the torso and the other the neck and head. The effects of the arms and legs are not included in this analysis. Suggested dimensions for the model astronaut are given below and represent the mean dimensions of U. S. Air Force flying personnel. The torso, head and neck mean dimensions were obtained from Table 29-1 of reference 53. The model astronaut is illustrated in figure 38.

Torso

$$\text{Height} = \text{Cervical height} - \text{crotch height} = 59.08 - 32.83 = 26.25''$$

$$\text{Minor Axis} = \frac{\text{Chest depth} + \text{waist depth} + \text{buttock depth}}{3} =$$

$$\frac{9.06 + 7.94 + 8.81}{3} = 8.60''$$

$$\text{Major Axis} = \frac{\text{Biacromial diameter} + \text{hip breadth}}{2} =$$

$$\frac{15.75 + 13.17}{2} = 14.46''$$

Head and Neck

$$\text{Height} = \text{sitting height} - \text{shoulder (acromial) height (sitting)} = 35.94 - 23.26 = 12.68''$$

$$\text{Minor Axis} = \text{Bitragion diameter} = 5.60''$$

$$\text{Major Axis} = \text{Head length} = 7.76''$$

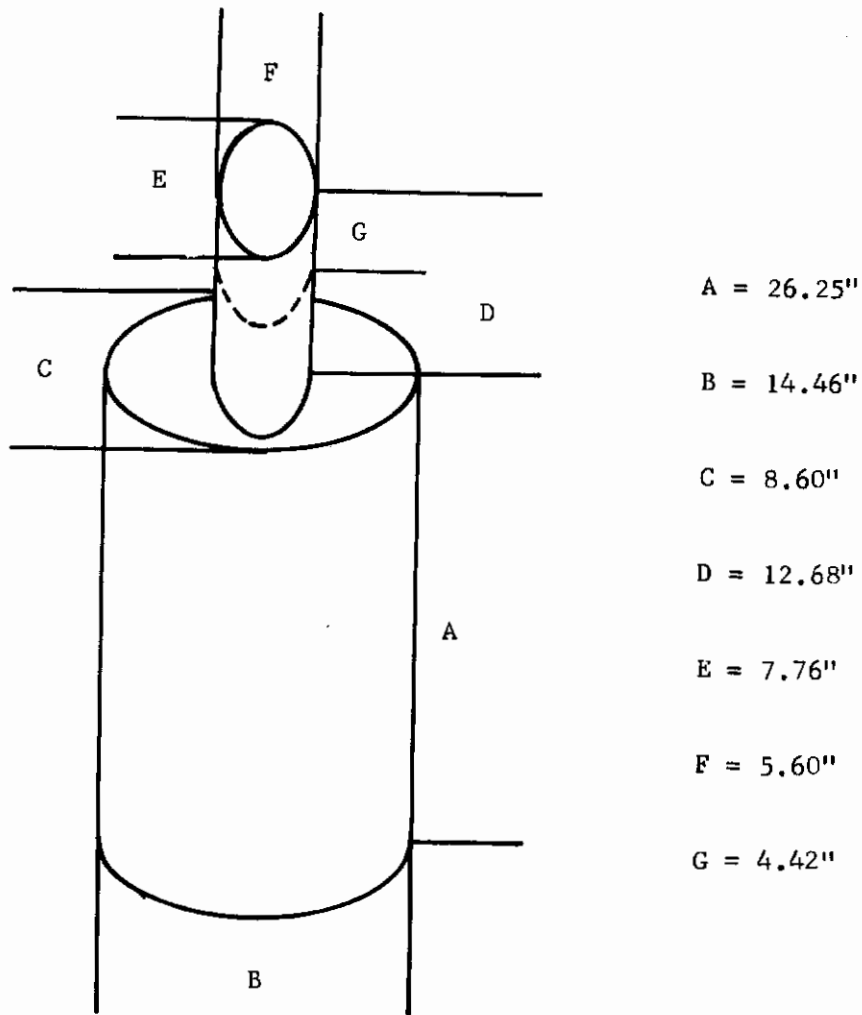


Figure 38. Model Astronaut Based on Dimensions of U. S. Air Force Flying Personnel

Eye Level

Height = stature = 69.11"

Eye (Internal Canthus) Height = 64.69"

Eye Level = 69.11" - 64.69" = 4.42"

The dimensions of the model astronaut are input parameters in the CARS program and need not be those given above.

7.2 BIOMEDICAL TOLERANCES

In order to evaluate the radiation hazards of space flight it is necessary to locate the susceptible organs of the body. Since the different organs have their individual tolerance levels, it is necessary to consider the important ones separately. Those of chief concern in this study are the eyes, the skin, and the blood forming organs. The mean eye level of U. S. Air Force flying personnel (ref 53) is 4.42" from the top of the head and the mean depth of the eyes is 3.0 millimeters. The blood forming organs are at a depth of approximately 5.25 g/cm². Calculated dose rates for the different organs are given in Section 8 for Van Allen proton and electron spectra and the envelope solar flare proton spectrum.

In lieu of Air Force tolerance levels for the various organs, current NASA tolerance levels are given in table 11.

TABLE 11

NASA BIOMEDICAL TOLERANCES

Critical Organ	Maximum Single Acute Exposure (rad)	Design Dose (rad)
Eyes	100	25
Skin Body Dose 0.07mm Depth	500	125
Blood Forming Organs	200	50

7.3 CALCULATION OF TISSUE SLANT THICKNESS

Tissue slant thicknesses which radiation must penetrate to arrive at a point are calculated for the incremental solid angles. Rays from this point to the points on the vehicle surface are assumed to be representative of the solid angles. Using the mathematical model astronaut described above,

Contrails

the intersection points of these rays on the elliptic and plane surfaces are determined. The rays are defined by spherical coordinate angles, θ and φ , and must be recalculated for each new point in the astronaut. The angles are found by

$$\varphi_{ij} = \cos^{-1} \left[\frac{z_{ij} - ZREF}{RV_{ij}} \right] \quad (84)$$

$$\theta_{ij} = \cos^{-1} \left[\frac{x_{ij} - XREF}{RV_{ij} \sin(\varphi_{ij})} \right] \quad (85)$$

where x_{ij}, z_{ij} = coordinates of intersection points on vehicle surface

$XREF, ZREF$ = coordinates of reference point

RV_{ij} = Radius vector from the reference point to a point on the surface

Equations for calculating the coordinates of the intersection points on the model astronaut surfaces are

$$x = t \sin \varphi_{ij} \cos \theta_{ij} \quad (86)$$

$$y = t \sin \varphi_{ij} \sin \theta_{ij} \quad (87)$$

$$z = t \cos \varphi_{ij} \quad (88)$$

where

Plane

$$t = \frac{1}{A_1} \quad (89)$$

$$A_1 = \frac{\sin \varphi \cos \theta}{a} + \frac{\sin \varphi \sin \theta}{b} + \frac{\cos \varphi}{c} \quad (90)$$

Elliptical Cylinder

$$t = \frac{-B_1 \pm \sqrt{B_1^2 - 4A_1 C_1}}{2A_1} \quad (91)$$

$$A_1 = b^2 \cos^2 \varphi + c^2 \sin^2 \varphi \sin^2 \theta \quad (92)$$

$$B_1 = -2Cb^2 \cos \varphi - 2c^2 B \sin \varphi \sin \theta \quad (93)$$

$$C_1 = b^2 c^2 + c^2 B^2 - b^2 c^2 \quad (94)$$

Contrails

Since the mathematical surfaces describing the model astronaut are infinite lines, planes, and elliptical cylinders, many of the calculated intersection points are not actually within the limits of the model. A subroutine in MAVRAC determines which intersection points are valid. A test is made first to see if the intersection is on the right end of the ray. Other tests are made to see if the point is within the elliptical boundaries or to see if it lies between the proper planes.

Once a point is found to be valid it is a simple matter to obtain the slant tissue thickness (TIS_{ij}).

$$TIS_{ij} = \sqrt{x^2 + y^2 + z^2} \quad (95)$$

If rays pass through both torso and head the thicknesses are merely added to get the total tissue thickness.

SECTION 8

RESULTS

As stated previously, the three hazardous components of space radiation are considered to be the Van Allen zone protons, the solar flare protons, and the artificial belt electrons. In addition, the critical biomedical tolerances have been stated for the eyes, skin, and blood forming organs. Therefore, results of dose calculations are presented for these environments and these organs. The results are presented in table 12.

In calculating the results presented in table 12, 342 incremental solid angles were utilized to obtain the dose at each point. For the skin dose, 182 points were utilized to obtain the mean dose listed in table 12; and for the blood forming organs (5 cm deep) 302 points were examined. In obtaining a representative dose to the eyes, the mean dose was calculated for 10 points at eye level and 3mm deep.

TABLE 12

DOSE RESULTS

Environment Critical Organ	Normalized Van Allen Protons ⁽¹⁾	Normalized Envelope Flare Protons ⁽²⁾	Normalized Artificial Belt Electrons ⁽³⁾
Eyes	2.49×10^{-3}	2.16×10^{-6}	2.83×10^{-7}
Skin	2.68×10^{-3}	3.07×10^{-6}	7.48×10^{-7}
Blood Forming Organs	1.46×10^{-3}	0.48×10^{-6}	1.27×10^{-7}

(1) Units for this column are $\text{rads hr}^{-1}/\text{Proton } E > 40 \text{ Mev cm}^{-2} \text{ sec}^{-1} \text{ ster}^{-1}$

(2) Units for this column are $\text{rads}/\text{Proton } E > 100 \text{ Mev cm}^{-2} \text{ ster}^{-1}$

(3) Units for this column are $\text{rads hr}^{-1}/\text{Electron } E > 0 \text{ Mev cm}^{-2} \text{ sec}^{-1} \text{ ster}^{-1}$

SECTION 9

RECOMMENDATIONS

Based upon the experience gained performing the study discussed in the previous Sections, it is recommended that future effort on Computer Analysis of Radiation Shielding be expended on the following:

- (1) Parametric studies to be conducted to evaluate the radiation hazard for various types of space missions.
- (2) Improvement in the representation of the bloodforming organs.
- (3) Upgrading the environmental data to account for variability of spectra.
- (4) Generalization of geometry to account for equipment.
- (5) Evaluation of the importance of orientation of vehicle with respect to the anisotropy of the trapped radiation.

REFERENCES

1. McIlwain, C. E., "Coordinates for Mapping the Distribution of Magnetically Trapped Particles," Journal of Geophysical Research, Vol. 66, No. 11, November 1961, pp. 3681-3691.
2. Northrop, T. G., and Teller, E., "Stability of the Adiabatic Motion of Charged Particles in the Earth's Field," Physical Review, Vol. 117, No. 1, January 1, 1960, pp. 215-225.
3. Stone, E. C., "The Physical Significance and Application of L , B_0 , and R_0 to Geomagnetically Trapped Particles," Journal of Geophysical Research, Vol. 68, No. 14, July 15, 1963, pp. 4157-4166.
4. Chapman, S. and Bartels, J., Geomagnetism, Vol. 2, Oxford: Clarendon Press, 1940, p. 610.
5. Finch, H. F. and Leaton, B. R., "The Earth's Main Magnetic Field-Epoch 1955.0," Monthly Notices of the Royal Astronomical Society, Geophysical Supplement, Vol. 64, No. 7, November 1957, pp. 314-317.
6. Jensen, D. C. and Cain, J. C., "An Interim Geomagnetic Field," Journal of Geophysical Research, Vol. 67, No. 9, August 1962, pp. 3568-3569.
7. Jensen, D. C. and Whitaker, W. A., "A Spherical Harmonic Analysis of the Geomagnetic Field," Journal of Geophysical Research, Vol. 65, No. 8, August 1960, p. 2500.
8. Brown, W. L., Hess, W. N., and Van Allen, J. A., "Collected Papers on the Artificial Radiation Belt From the July 9, 1962, Nuclear Explosion - Introduction," Journal of Geophysical Research, Vol. 68, No. 3, February 1, 1963, pp. 605-606.
9. Singer, S. F., "Trapped Albedo Theory of the Radiation Belt," Physical Review Letters, Vol. 1, No. 5, September 1, 1958, pp. 181-183.
10. Pizzella, G., McIlwain, C. E., and Van Allen, J. A., "Time Variations of Intensity in the Earth's Inner Radiation Zone, October 1959 through December 1960," Journal of Geophysical Research, Vol. 67, No. 4, April 1962, pp. 1235-1253.
11. Lenchek, A. M. and Singer, S. F., "Geomagnetically Trapped Protons from Cosmic-Ray Albedo Neutrons," Journal of Geophysical Research, Vol. 67, No. 4, April 1962, pp. 1263-1287.
12. McIlwain, C. E., "The Radiation Belts, Natural and Artificial," Science, Vol. 142, No. 3590, October 18, 1963, pp. 355-361.

REFERENCES (Cont'd)

13. Freden, S. C. and White R. S., Trapped Proton and Cosmic-Ray Albedo Neutron Fluxes, UCRL-6603, University of California, October 2, 1961.
14. Id., "Particle Fluxes in the Inner Radiation Belt," Journal of Geophysical Research, Vol. 65, No. 5, May 1960, pp. 1377-1383.
15. Id., "Protons in the Earth's Magnetic Field," Physical Review Letters, Vol. 3, No. 1, July 1, 1959, pp. 9-11.
16. Naugle, J. E. and Kniffen, D. A., "Variations of the Proton Energy Spectrum with Position in the Inner Van Allen Belt," Journal of Geophysical Research, Vol. 68, No. 13, July 1, 1963, pp. 4065-4078.
17. Carter, R. E., Reines, F., Wagner, J. J., and Wyman, M. E., "Free Antineutrino Absorption Cross Section. II. Expected Cross Section from Measurements of Fission Fragment Electron Spectrum," Physical Review, Vol. 113, No. 1, January 1, 1959, pp. 280-286.
18. McIlwain, C. E., private communication.
19. O'Brien, B. J., Van Allen, J. A., Laughlin, C. D., and Frank, L. A., "Absolute Electron Intensities in the Heart of the Earth's Outer Radiation Zone," Journal of Geophysical Research, Vol. 67, No. 1, January 1962, pp. 397-403.
20. Bailey, D. K., "Time Variations of the Energy Spectrum of Solar Cosmic Rays in Relation to the Radiation Hazard in Space," Journal of Geophysical Research, Vol. 67, No. 1, January 1962, pp. 391-396.
21. Winckler, J. R., "Solar Influences on the Radiation Field in Space," Aerospace Medicine, Vol. 32, No. 10, October 1961.
22. Bryant, D. A., et al., "Solar Cosmic Rays Following the Flare of September 28, 1961," Paper presented at the American Geophysical Union Meeting, Washington, D. C., April 1962.
23. Anderson, K. A., Preliminary Study of Prediction Aspects of Solar Cosmic-Ray Events, NASA TN D-700, University of California, April 1961.
24. Weddell, J. B., "Statistical Prediction of Solar Proton Events," Proceedings of the Symposium on the Protection Against Radiation Hazards in Space, TID-7652, Gatlinburg, Tennessee, November 5-7, 1962.

REFERENCES (Cont'd)

25. Chupp, E. L. Dye, D. L., Mar, B. W., Oncley, L. A., and Williamson, R. W., Analysis of Solar-Flare Hazard to Manned Space Systems, D2-11608, The Boeing Company, Seattle, Washington.
26. Project Apollo Spacecraft Development Statement of Work, Part 3, Technical Approach, NASA Manned Spacecraft Center, Langley Air Force Base, Virginia, December 18, 1961. (CONFIDENTIAL).
27. Solar Proton Manual, X-611-62-122, ed., McDonald, F. B., Goddard Space Flight Center, Greenbelt, Maryland, January 1963.
28. Meyer, P. and Vogt, R., The Primary Cosmic Ray Electron Flux During a Forbush-Type Decrease, EFINS-61-50, University of Chicago, August 1961.
29. Biermann, L., "Comet Tails and Solar Corpuscular Emission," Zeitschrift fur Astrophysik, Vol. 29, 1951, pp. 274-286.
30. Parker, E. N., "Extension of the Solar Corona into Interplanetary Space," Journal of Geophysical Research, Vol. 64, No. 11, 1959, pp. 1675-1681.
31. Morrison, M. R. and Tate, A. E., Determination of Particle Fluxes Impinging on a Spacecraft, NSL 63-63R-1, Northrop Space Laboratories, Hawthorne, California, Contract No. AF 33(657)-8762, August 1963.
32. Bette, Hans A. and Ashkin, Julius, "Passage of Radiation Through Matter," Experimental Nuclear Physics, Vol. I, Edited by Segre, John Wiley and Sons, Inc., New York (1953).
33. Halliday, David, Introductory Nuclear Physics, John Wiley and Sons, Inc., New York, 1955.
34. Nelms, Ann T., Energy Loss and Range of Electrons and Positrons, Supplement to NBS Circular 577, National Bureau of Standards, Washington, D. C., July 30, 1958.
35. Perkins, J. F., "Monte Carlo Calculations of Transport of Fast Electrons," Physical Review, Vol. 126, No. 5, June 1, 1962.
36. Evans, Robley D., The Atomic Nucleus, McGraw-Hill Book Company, Inc., New York, 1955.
37. Hansen, N. E. and Fultz, Cross Sections and Spectra for Negative Electron Bremsstrahlung, UCRL 6099, University of California, Lawrence Radiation Laboratory, Livermore, California, November 15, 1960.
38. Koch, H. W., and Motz, H. W., "Bremsstrahlung Cross Section Formulas and Related Data," Review of Modern Physics, Vol. 31, No. 4, October 1959.

REFERENCES (Cont'd)

39. Fortney, R. E., Electron Penetration and Bremsstrahlung Production, NSL 63-158, 1963, Northrop Space Laboratories, Hawthorne, California.
40. Heitler, W., The Quantum Theory of Radiation, Oxford Clarendon Press, 1954.
41. Kinsman, Simon, Radiological Health Handbook, U. S. Department of Health, Education, and Welfare, Cincinnati, Ohio, January 1957.
42. Bichsel, Hans, Higher Shell Corrections in Stopping Power, Technical Report No. 3, Linear Acceleration Group, Department of Physics, University of Southern California, Los Angeles, California, 21 June 1961.
43. Sternheimer, R., "Range-Energy Relations for Protons in Be, C, Al, Cu, Pb, and Air," Physical Review, Vol. 115, No. 1, July 1, 1959.
44. Chapman, M. C., Proton Ionization Losses in Material, NSR 60-7, Northrop Corporation, Hawthorne, California, 24 May 1960.
45. Bertini, H. W., Monte Carlo Calculations on Intranuclear Cascades, ORNL-3383, Oak Ridge National Laboratory, Oak Ridge, Tennessee, 1963.
46. Blatt, John M. and Weisskopf, Victor F., Theoretical Nuclear Physics, John Wiley and Sons, New York, 1960.
47. Allen R. I., et al., Shielding Problems in Manned Space Vehicles, NR-140, Lockheed Nuclear Products, Marietta, Georgia, September 1961.
48. Duckworth, G. D. and Fortney, R. E., Proton Shielding Program for the IBM 7090, NSL 62-81, Northrop Space Laboratories, Hawthorne, California, May 1962.
49. Madey, Richard, Duneer, Arthur, G., Jr., and Krieger, Theodore, Jr., "Gamma Dose from Solar Flare Protons Incident on an Aluminum Shield," Transactions of the American Nuclear Society, Vol. 5, No. 1, 1962.
50. Alsmiller, F. S., Alsmiller, R. G., Jr., and Trubery, D. K., "Comparison of Primary Proton Dose with the Dose From Gamma Rays Produced by Inelastic Scattering of Solar Flare Protons," ORNL-3360, October 8, 1962.
51. Murphy, B. L., Kitshing, P., and Knowles, H. B., "The Biological Hazards of π and μ Mesons," Proceedings of the Symposium on the Protection Against Radiation Hazards in Space, TID-7652, Gatlinburg, Tennessee.

Contrails

REFERENCES (Cont'd)

52. Duckworth, G. D., Model Astronaut and Vehicle Radiation Analysis Code (MAVRAC), NSL 63-159, Northrop Space Laboratories, Hawthorne, California, Contract AF 33(657)-8762, 1963.
53. Hansen, R., Cornog, D. Y., Hertzberg, H. T. E., Annotated Bibliography of Applied Physical Anthropology in Human Engineering, WADC TR 56-30, Wright Air Development Division, Wright-Patterson AFB, Ohio.